DYNAMICS AND SPATIO-TEMPORAL VARIABILITY OF THE MID-ATLANTIC BIGHT COLD POOL

by

ZHUOMIN CHEN

A dissertation submitted to the

School of Graduate Studies

Rutgers, The State University of New Jersey

In partial fulfillment of the requirements

For the degree of

Doctor of Philosophy

Graduate Program in Oceanography

Written under the direction of

Enrique N. Curchitser

And approved by

_____

_____

_____

_____

New Brunswick, New Jersey

October, 2018

ABSTRACT OF THE DISSERTATION

Dynamics and Spatio-temporal Variability of the Mid-Atlantic Bight Cold Pool

by Zhuomin Chen

Dissertation Director:

Enrique N. Curchitser

The Mid-Atlantic Bight (MAB) Cold Pool is a bottom-trapped cold (lower than 10 °C) and fresh (lower than 34 psu) water mass, that is isolated from the surface by the seasonal thermocline, and is located over the mid- and outer-shelf of the MAB. It has been recognized that the Cold Pool plays an important role in impacting the along-shelf and across-shelf seasonal and interannual variations of temperature, salinity, sea surface slope, and exchange of heat and salt. Environmentally driven changes in habitats, have been shown to have a first order impact on the MAB ecosystem. For example, spatio-temporal variability of the Cold Pool exerts strong influence on the recruitment and settlement of several cold-temperatures fish species in the MAB ecosystem.

Following the Cold Pool definition, we put forward a method that includes three criteria to capture and quantify the Cold Pool characteristics, based on a 50-year (1958-2007) high-resolution regional ocean model hindcast simulation. The seasonal climatology of the Cold Pool and its properties are investigated during its *onset* - *peak* - *decline* cycle. Three stages of the Cold Pool event are defined according to its evolving status and characteristics. The cores of the Cold Pool

usually travel along the 60-m isobath starting south of the New England shelf to the Hudson Shelf Valley at a speed of approximately 2 cm/s. The depth-averaged heat budget of the near-bottom water column (below 30-m depth) over the MAB and Georges Bank is investigated to compare the relative contribution between the vertical diffusion from the surface layer and advection during strong and weak Cold Pool years. Possible origins of the Cold Pool are investigated by performing a lead-lag correlation analysis. Results suggest that the Cold Pool originates not only from local remnants of winter water near the Nantucket Shoals, but has an upstream source traveling in the spring time from the southwestern flank of the GB along the 80-m isobath.

The interannual variability of the Cold Pool and summer progressions are also investigated. Results show that the Cold Pool exhibits significant year-to-year variability in the state variables (persistence time, volume and temperature), spatial distribution and the equatorward progression. Based on the persistence time, volume and volume-averaged temperature, a Cold Pool Index (CPI) is defined and computed in order to represent the strength of the Cold Pool. Anomalous strong and weak years are investigated using a composite analysis according to the CPI values. The volume-averaged heat budget of the Cold Pool region between strong and weak years is investigated. Results suggest that abnormal warming/cooling from initial temperature and horizontal advection drives the interannual variability in temperature. The depth-averaged temperature anomaly in the Cold Pool region is largely determined by the initial temperature anomaly in the early spring, suggesting a potential for seasonal predictability.

Statistical relationships between the Cold Pool temperature and large-scale oceanic and atmospheric processes in the Northwest Atlantic Ocean are investigated. The relationship between the Cold Pool temperature and the north-south shift of the Gulf Stream position are investigated. Results shows that the spring Cold Pool temperature has a significant positive correlation with the annual Gulf

Stream index. Besides, the fall Gulf Stream position is significantly correlated with the Cold Pool temperature in the following spring, enhancing the use of the fall Gulf Stream position as a leading indicator of the Cold Pool temperature. The Cold Pool temperature also has a positive response to the winter NAO, with the Cold Pool temperature lagging the NAO by approximately 2 years. The possible mechanistic link between the Cold Pool temperature, Gulf Stream position and the NAO are discussed.

Acknowledgements

First of all, I would like to express my deepest gratitude to Enrique Curchitser, my supervisor, for leading me to the world of the Mid-Atlantic Bight Cold Pool, continually guiding me and giving me confidence and knowledge throughout my time at Rutgers. I really appreciate the opportunity being admitted into the program and became one of his group members of the Earth System Modeling Group five years ago. He gave me lots of encouragement and enough freedom to explore interesting topics around the Cold Pool and so many valuable advices towards the science and future career.

I would also like to express sincere thanks to my committee members, Robert Chant, Josh Kohut and Ruoying He, for their consistent support and help on my graduate work. Bob gave me a lot of help and valuable suggestions during my hardest time in research. I really enjoy the regular ocean modeling lab meeting leaded by him and John Wilkin. I have learned a lot through sharing my research and discussions with other lab members, Eli Hunter, Piero Mazzini and Julia Levin, etc. Bob also gave me valuable suggestions on the second chapter of this thesis. A lot of thanks to Josh, who pointed out an interesting topic of the Cold Pool for me, which is to investigate the connection of the Cold Pool to the Labrador Sea. This later becomes part of the fourth chapter. I also would like to thank Ruoying serving as an external member on my committee. As an excellent expert in coastal oceanography, he gave me a lot of good advices about investigating the relationship between the Gulf Stream and the Cold Pool, as well as dealing with observation and model datasets over the Northwest Atlantic coastal ocean.

I also want to thank every current and previous members of the Earth System Modeling group at Rutgers, Dujuan Kang, Raphael Dussin, Elizabeth Drenkard, Shuwen Zhang, Dimitris Politikos, Romain Escudier, Alexandra Ramos, Bryan Raney, et al., for all their help throughout my PhD study. Dujuan not only helps me in my research, but also a good friend in life. With her accompany, my graduate life becomes much easier. I also would like to thank Byoung-Ju Choi for introducing the world of Ensemble Kalman Filter to me, during his stay with the group. Special thanks to Michael Alexander, who inspires me to think about the reemergence mechanism, and to Kate Hedstrom, who helps me when I rerun the ROMS-NWA model on Cheyenne.

I also want to thank my fellow graduate students in the Graduate Program of Oceanography for the friendship. Specially, Xinzhong Zhang helps me a lot during my first two years at Rutgers. Without his help, I won't quickly get used to the life in a foreign country. Guangyu Xu and Hanzhi Lin are also great friends and alumna. They make my life of living abroad much easier. I also would like to thank Chuning Wang, Fernando Pareja, Christopher Free, Amy Kuzminov for their accompany, and I will remember the happy time taking classes together with them. A sincere thank you to my friend Lequan Chi, for his consistent help in research.

Lastly, I would like to thank my parents, grandparents and the whole family in China for their unconditional care and support.

Dedication

To my dear mom and dad, Lina Lin, Guangping Chen, who love me, believe in me, and have supported me every step of the way.

Table of Contents

List of Tables

List of Figures

Chapter 1
Introduction

1.1 Importance of the Cold Pool

The Intergovernmental Panel on Climate Change (IPCC) fifth assessment shows that the global ocean including the Northwest Atlantic (NWA) Ocean has a general warming trend [Collins, 2013]. A recent study by Saba et al. [2016] revisited this warming trend in the NWA, and suggested warming over the continental shelf may be greater and faster than previously projected by IPCC. This change is believed to be related to a retreat of the Labrador Current, a northerly shrift of the Gulf Stream, and a replacement of cold Labrador Slope Water by warm Atlantic Temperate Slope Water along the Shelf Slope [Saba et al., 2016]. Warming on a scale of 3-4 °C has been shown to cause extreme impacts on the ecosystem, especially on commercially important fisheries [Benway and Jossi, 1998, Narváez et al., 2015].

As the most important thermal feature over the Mid-Atlantic Bight (MAB), the Cold Pool is closely related to recruitment and settlement of several cold-temperate fishery species in the MAB ecosystem, as well as phytoplankton productivity [Flagg et al., 1994, Miller et al., 2016, Sullivan et al., 2005, Weinberg, 2005]. Recent studies aim to explore the mechanism behind this connection [Miller et al., 2016], however, the mechanism of the formation and evolution of the Cold Pool itself is not yet well investigated. Thus, a better understanding of the Cold Pool and its dynamics is important for the investigation of oceanic productivity along northwestern coast of the Atlantic Ocean.

1.2 The Mid-Atlantic Bight

The Mid-Atlantic Bight (MAB) is one of the principal, productive, coastal oceanographic regimes situated off the northeast US seaboard. It stretches from Cape Cod to Cape Hatteras [Mountain, 2003, Churchill and Gawarkiewicz, 2012], exhibiting a strong seasonal cycle in physical and biological processes [Gong et al., 2010]. The shelf width and depth of Middle Atlantic Bight are typically 100-200km and 100-200m. The most prominent feature of the MAB is the Hudson Shelf Valley (HSV), an across-shelf valley that functions as a channel for across-shelf transport as well as a dynamical boundary for along-shelf flow (Figure 1.1) [Gong et al., 2010]. South of the HSV is another important shelf feature - the Fortune/Tiger Shore, outlined by the 40m isobath. The steep topography between the 40 and 60 m isobaths at the outer shelf edge of this shoreline have an important influence on across-shelf transport [Gong et al., 2010]. The Connecticut river, Hudson river, Delaware river and the Susquahana river are the primary rivers delivering fresh and nutrient rich water onto the shelf [Gong et al., 2010].

The MAB continental shelf is dominated by a continuous but leaky current system with a mean depth-averaged equatorward along-shelf flow of 5-10 cm/s linearly correlated with topography, increasing offshore (Figure 1.2) [Lentz, 2008a,b]. There are significant seasonal variations in the mean shelf flow: during stratified and well-mixed seasons of summer and winter, the shelf flow is cross-shelf dominated; while during transition seasons of spring and fall, it is along-shelf dominated [Gong et al., 2010]. Lentz [2008a] found that seasonal variations in the depth-averaged flow are polarized, with major axis amplitudes of 1-5 cm/s, oriented along isobath at most sites. Seasonal variations in the wind stress and the buoyancy-driven cross-shelf density gradient play key roles in significant variations in the along-shelf flow [Lentz, 2008a], especially for the southern MAB and the inner New England shelf. Apart from wind forcing and buoyancy forcing,

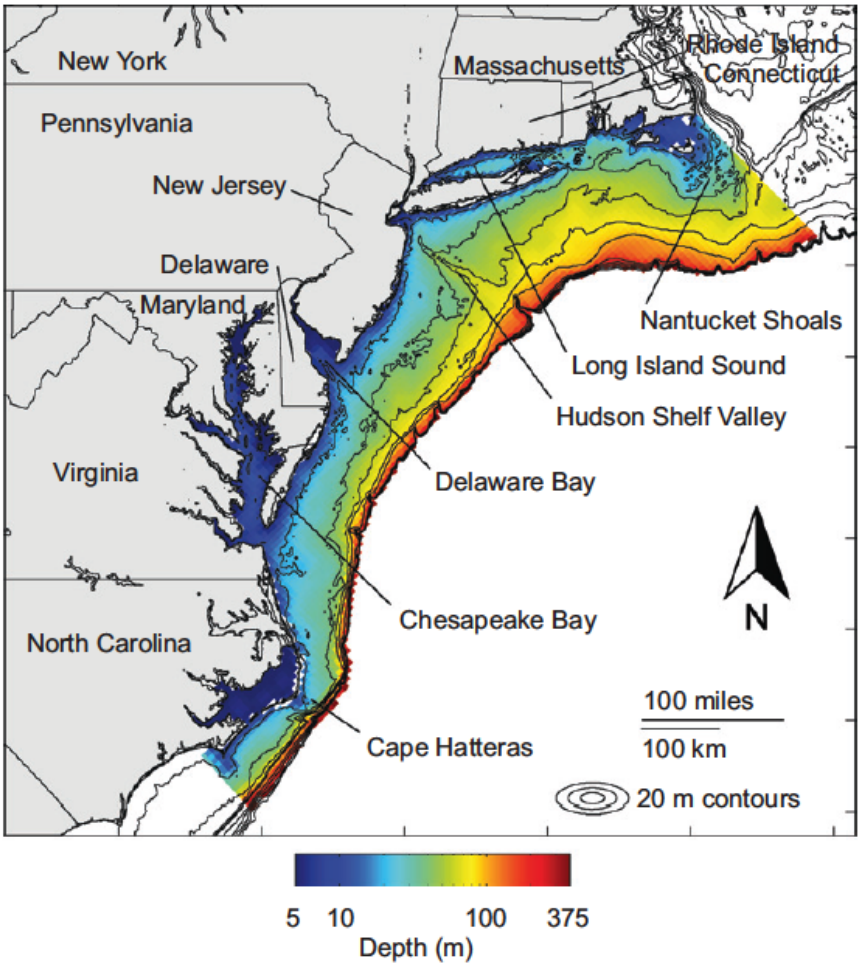

Figure 1.1: The study area of the Mid-Atlantic Bight with bathymetric contours derived from the ETOPO2 data. Figure is from Dalyander et al. [2013].

tidal rectification, topography, bottom boundary layer, and slope water intrusions appear to be the dominant dynamical factors in the MAB current system as well.

1.3 The MAB Shelf Water

The primary water mass in the MAB is the Shelf Water, part of a large scale coastal current system that extends from Labrador to Cape Hatteras, separated from the warmer and saltier Slope Water offshore by a well-defined surface-to-bottom salinity and density front with a mean drift towards the south (Figure 1.2) [Mountain, 2003, Churchill and Gawarkiewicz, 2012]. While traveling in the MAB,

properties of the Shelf Water are regionally modified by topography and several processes, such as surface heating and cooling, enhanced tidal mixing, local precipitation and river discharge, and mixing with the Slope Water [Mountain, 2003]. As the Shelf Water travels southward, most of it exits the shelf through a number of processes [Gong et al., 2010]. The Shelf Water is usually diverted offshore and entrained into Gulf Stream warm core rings or smaller instability-generated eddies to the deep ocean near the Cape Hatteras [Mountain, 2003, Churchill and Gawarkiewicz, 2012].

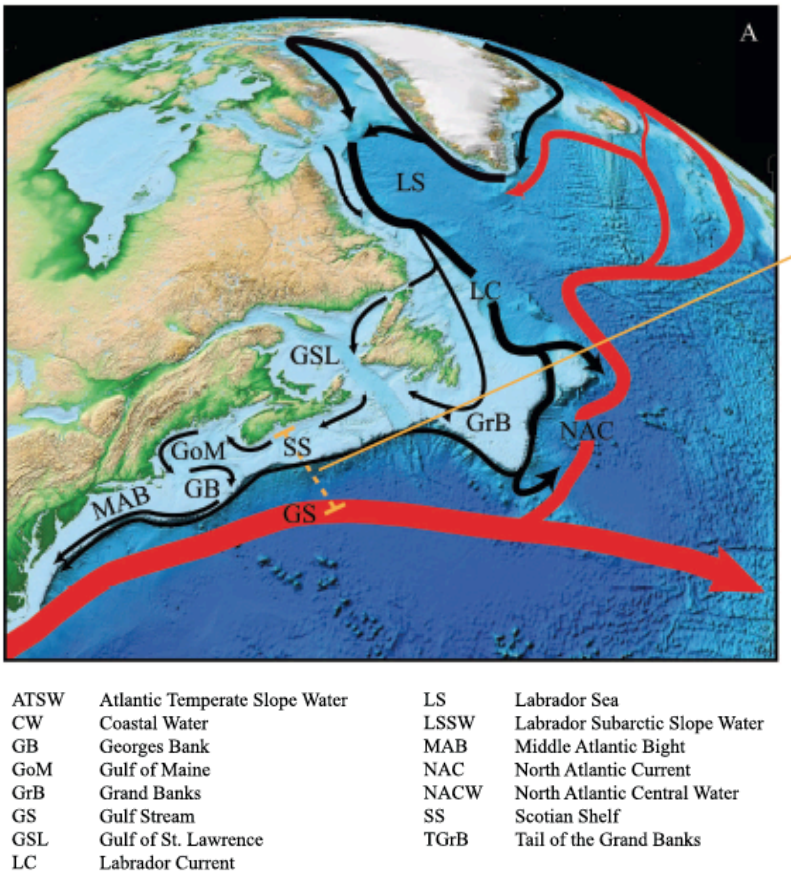

Figure 1.2: Circulation pattern of the Northwest Atlantic Ocean. Figure is from Greene et al. [2013].

The Shelf Water in the MAB is regarded as a water mass that is usually formed in the Gulf of Maine through mixing of cold and fresh water from the Scotian Shelf and the warmer and saltier Slope Water through the Northeast

Channel [Mountain, 2003]. Occasional mixing may happen directly between water from Scotian Shelf through the Northeast Channel and water on eastern GB [Mountain, 2003]. Based on oxygen isotope measurements, the shelf water in MAB was affected by the fluctuations in (1) the cold and fresh sub-polar water input from farther north glacial melt and (2) additional fresh water input through nearby river runoff [Chapman and Beardsley, 1989]. Thus, this upstream water source is a mixture of brine-enriched shelf water and high-latitude river discharge [Khatiwala et al., 1999]. Loder et al. [1998] suggest that the Arctic Ocean serves as the primary source of cold and fresh water to the Northwest Atlantic continental shelf.

There are strong regional and seasonal variations in Shelf Water temperatures with a substantial influence from coastal air temperature patterns [Mountain, 2003]. The annual maximum (minimum) temperature occur progressively earlier (later) from south to north, and it also exhibits a spatial pattern with summer maximums increasing from north to south [Mountain, 2003]. Strong annual variations in surface temperature also show more substantial influences from air-sea interactions than advection. Surface heating typically leads to a stratified water column with a warm and shallow near-surface layer from spring to fall, overlying a cool near-bottom layer located over the mid- and outer-shelf, which is the Cold Pool water. Seasonal evolution and dissolution of near-bottom Cold Pool water over the mid- and outer-shelf, in turn play an important role in the seasonal variation of both the across-shelf and along-shelf temperature gradient [Lentz, 2008a]. It is evident that the seasonal variations in surface heat flux plays a primary role as the heat source (and sink) for the shelf waters, with additional influences from sub-polar shelf water, offshore slope water and sea ice. Apart from air-sea heat flux and advection, seasonal cycles of temperature and salinity are further modified by intrusions of Slope Water and Gulf Stream rings [Benway and Jossi, 1998].

1.4 Thesis Structure

The overaching theme of this thesis is to explore the seasonal-to-interannual variability of the Mid-Atlantic Bight (MAB) Cold Pool, as well as its possible origins and relationships with large-scale ocean circulation variability, for better understanding the Cold Pool formation and evolution. Here, we use a long-term (1958-2007) high-resolution (horizontal resolution: 7 km; 40 vertical layers) numerical simulation of the Northwest Atlantic Ocean with the Regional Ocean Modeling System (ROMS-NWA). Based on the definition of the Cold Pool (a cold and fresh water mass located over the mid- and outer-shelf of the MAB below a seasonal thermocline), we develop a Cold Pool quantification method to quantify the Cold Pool characteristics, such as total volume, mean temperature and salinity, as well as its cores and extents. Three criteria are employed in the quantification method: (1) the Temperature and Salinity Criteria, (2) the Stratification Criteria, (3) the Location Criteria.

The first research chapter (Chapter 2) focuses on the seasonal variability of the Cold Pool over the 50-year average. We define three stages of the Cold Pool according to its seasonal evolution and characteristics. The seasonal variations in the cores and different retreating speeds of its north and south extents are investigated. Depth-averaged heat budget of the near-bottom layer is built to explore the relative importance of heat advection versus vertical mixing. Compared to vertical mixing, advection is suggested to play an key role in leading the difference in retreat speeds. Besides, we also perform a lead-lag correlation analysis on the 50-year near-bottom depth-mean temperature anomalies to explore possible origins of the Cold Pool.

Given the results in Chapter 2 that our quantification method and the model is capable of capturing the seasonal variability of the Cold Pool, we investigate

the interannual variability of the Cold Pool in Chapter 3. The Cold Pool characteristics (persistence time, volume, temperature) have a strong year-to-year oscillation. According to the persistence time, volume magnitude and volume-averaged temperature, we derive a Cold Pool Index (CPI) in order to evaluate the Cold Pool strength of each year. The Cold Pool characteristics and the equatorward progressions during strong and weak Cold Pool years are compared and investigated, using the composite analysis according to the CPI values. A detailed quantitative study of relative importance of advection versus initial temperature in the spring between strong and weak Cold-Pool years is investigated, using a near-bottom volumed-averaged heat budget.

In the last research chapter (Chapter 4), we focus on the relationship between the Cold Pool characteristics and large-scale processes in the Northwest Atlantic Ocean, the north-south shift of the Gulf Stream path and the North Atlantic Oscillation. Statistical relationship between the Cold Pool temperature and the north-south shift of the Gulf Stream position are investigated. Besides, the Cold Pool temperature also has a positive response to the winter NAO, with the Cold Pool temperature lagging the NAO by approximately 2 years. The possible mechanistic link between the Cold Pool temperature, Gulf Stream position and the NAO are discussed.

Finally, we summarize the main conclusions from previous research chapters in Chapter 5.

Chapter 2

Seasonal Variability of the Cold Pool over the Mid-Atlantic Bight Continental Shelf

2.1 Abstract

The Mid-Atlantic Bight (MAB) Cold Pool is a distinctive cold (lower than 10 °C) and relatively fresh (lower than 34 psu) water mass. It is located over the mid- and outer-shelf of the MAB, below the seasonal thermocline and is attached to the bottom. Following this definition, we put forward a method that includes three criteria to capture and quantify Cold Pool characteristics, based on a 50-year (1958-2007) high-resolution regional ocean model hindcast. The seasonal climatology of the Cold Pool and its properties are investigated during its *onset* - *peak* - *decline* cycle. Three stages of the Cold Pool event are defined according to its evolution and characteristics. The Cold Pool cores travel along the 60-m isobath starting south of the New England shelf to the Hudson Shelf Valley at a speed of 2-3 cm/s. Furthermore, the northern extent of the Cold Pool retreats about 2.6 times faster than the southern extent during the summer progression. The heat balance of the near-bottom water column over the MAB and Georges Bank (GB) is computed for a comparison of the relative contributions of the vertical mixing and horizontal- and vertical-advection. Possible origins of the Cold Pool are investigated by performing a lead-lag correlation analysis. Results suggest that the Cold Pool originates not only from local remnants of winter water near the Nantucket Shoals, but has an upstream source traveling in the spring time from the southwestern flank of the GB along the 80-m isobath.

2.2 Introduction

The Mid-Atlantic Bight (MAB) Cold Pool is a distinctive cold and relatively fresh water mass located over the mid- and outer-shelf that is one of the principal, productive, coastal oceanographic regimes situated off the northeast US seaboard [Houghton et al., 1982, Fairbanks, 1982, Brown et al., 2012]. It is usually colder than 10 °C and isolated from the surface by a seasonal thermocline. Cold Pool water is part of the primary shelf water mass of MAB, with salinity less than 34 psu [Mountain, 2003, Manning, 1991]. The relative cold and fresh shelf water of MAB is part of a large-scale buoyancy-driven coastal current system. The MAB shelf water is assumed to have origins from the north, as far as the Labrador Sea and the Baffin Bay, and exits the shelf near Cape Hatteras [Mountain, 2003, Gong et al., 2010, Churchill and Gawarkiewicz, 2012]. In the offshore direction, the MAB shelf water is separated from the warmer and saltier Slope Water by a well-defined surface-to-bottom salinity and density front that has a mean drift towards the south [Mountain, 2003, Churchill and Gawarkiewicz, 2012]. Properties of the shelf water are regionally modified by topography and several other processes, such as surface heating and cooling, enhanced tidal mixing, local precipitation and river discharge, and mixing with the Slope Water [Mountain, 2003].

It has been recognized that the Cold Pool plays an important role in impacting the along-shelf and across-shelf seasonal variations of temperatures, salinities, sea surface slopes, nutrient fluxes and distributions, and exchanges of heat and salt [Sha et al., 2015, Lentz, 2017]. Environmentally driven changes in habitats, have been shown to have a first order impact on the MAB ecosystem [Benway and Jossi, 1998, Narváez et al., 2015]. For example, spatio-temporal variability of the Cold Pool exerts strong influence on the recruitment and settlement of several cold-temperatures fish species in the MAB ecosystem [Miller et al., 2016, Sullivan et al., 2005, Nye et al., 2011, Adams et al., 2015], as well as phytoplankton

productivity [Flagg et al., 1994].

Understanding the origins and formation of the Cold Pool have been the focus of previous studies. Fundamentally, there are two hypotheses on the origin of the Cold Pool. The first is that the Cold Pool is the remnant of local winter water. The Cold Pool forms with strong winter mixing and becomes isolated from the surface due to the onset of summer stratification in the water column, with no renewal from upstream sources (north of the MAB) [Bigelow and Sears, 1933, Ketchum and Corwin, 1964, Houghton et al., 1982, Ou and Houghton, 1982]. The second hypothesis suggests that the Cold Pool does have origins from an upstream cold water source, such as the Gulf of Maine (GoM), Georges Bank (GB) [Hopkins and Garfield III, 1979, Han and Niedrauer, 1981, Fairbanks, 1982, Chapman and Beardsley, 1989, Brown et al., 2015].

The first hypothesis is supported by Bigelow and Sears [1933], who first observed and recorded the Cold Pool phenomenon by a series of cross-shelf shipboard measurements along the MAB coast between 1928 and 1931. The vertical thermal structure was first referred to as 'a pool of cold water that resides on the mid- and outer-shelf throughout the summer when a strong thermocline exists'. By identifying the limits of this thermal structure, irrespective of depth, Bigelow and Sears [1933] concluded that this cold water was formed due to mixing in the winter, persisted for several months in the spring and summer, and received no replenishment throughout the summer. Ketchum and Corwin [1964] revisited this phenomenon based on more continuous and dense shipboard observations off Long Island between 1956 and 1959. They confirmed that the Cold Pool was formed by local winter mixing together with the development of a shallow seasonal thermocline. They also concluded that the warming of the subsurface cold water on the continental shelf appears to be a result of mixing with warmer and saltier water either from the surface or from offshore at a similar depth and density.

Houghton et al. [1982] gave a more detailed description of the seasonal variation of the Cold Pool based on observational data within the MAB during the year 1979. They defined the Cold Pool as a distinctive cold water mass that first appears with the onset stratification in the spring, and then evolves throughout the summer until the water column overturns and mixes in the fall. Houghton et al. [1982] and Ou and Houghton [1982] both suggested that the cold core was initiated near the Nantucket Shoals (NS) and gradually drifted southward with a mean speed about 5 cm/s. They also suggested that the strong tidally-mixed winter water from the NS is the primary source of the Cold Pool. As spring arrives, the cold denser water mass becomes isolated from the surface and spreads over the New England Shelf (NES) and into the New York Bight (NYB). Then, it is the isolation from the surface heating, rather than replenishment of colder upstream water, that contributes to the Cold Pool's persistence throughout the summer months.

Alternatively, Hopkins and Garfield III [1979], Han and Niedrauer [1981] both suggested that instead of winter residual water near the NS, the GoM water is a probable source for the MAB Cold Pool. Based on the bottom temperatures in May and June 1975, they estimated that the traveling speed of the coldest region moved from the north to the Hudson Shelf Valley (HSV) was at about 3-4 cm/s. Water traveling for 4-5 months at that average velocity means that the cold water would have originated in the GoM in January. Additionally, based on salinity and isotopic analysis, Fairbanks [1982] suggested that the Cold Pool is probably diluted by sea ice melt water from the Gulf of St. Lawrence during the early spring. About two months later, there is still remnant melt water present but the Cold Pool has been mixed with, or renewed, by GoM water. After July, there is no remnant of the sea ice melt water. Thus it was concluded that the Cold Pool was continuously renewed from the upstream (north of the MAB) during the springtime, and there could be different origins of the Cold Pool between early

spring and summer.

Later, with support from Mid-Atlantic Regional Association Coastal Ocean Observing System (MARACOOS), repeated high-resolution glider measurements of temperature and salinity have been obtained along a series of along-shelf zigzag trajectories from Massachusetts to Maryland. Strong seasonal variations of temperature at depth off New Jersey were found to be consistent with advection of Cold Pool colder waters from the north during spring and summer [Castelao et al., 2008]. Based on a particularly comprehensive set of glider measurements for the year of 2007, Brown et al. [2015] revisited the thermal structure, defined five different stages of the annual Cold Pool phenomenon, and highlighted the importance of the May-to-June inflow of the cold water from GB and GoM regions.

Lentz [2017] explores the seasonal warming of the Cold Pool using in-situ measurements of temperature and salinity profiles collected between 1955 and 2014. The average annual evolution and spatial structure of the Cold Pool were characterized, and he found that the warming rate of the Cold Pool is not spatially uniform, but rather warms more rapidly over GB relative to the rest of the MAB. This is attributed to enhanced vertical mixing associated with strong tidal currents. Using a conceptual model of heat balance, Lentz [2017] estimates that the mean turbulent diffusivities at the top of the Cold Pool to be an order of magnitude larger over the GB than in the southern MAB. This is consistent with the fact that tidal mixing is stronger over GB than the MAB.

Thus, the mechanism of the formation and evolution of the Cold Pool are still being explored. Previous studies are mainly based on relative sparse observational datasets, limited by spatial and temporal resolution. Here, we investigate Cold Pool characteristics using a long-term high-resolution numerical model (ROMS-NWA). This paper focuses on investigating the Cold Pool climatology and seasonal variability. Subsequent work will emphasize the inter-annual and decadal scales.

This paper is organized as follows. Section 4.3 includes an introduction of the high-resolution ROMS-NWA model, model evaluation against observational datasets, and a description of the methods we use to quantify the Cold Pool based on its definition. Section 2.4 presents seasonal variability of the Cold Pool, and its summer progression. In Section 3.5, a heat budget of the near-bottom layer is investigated over the MAB and GB. In Section 2.6, possible origins of the Cold Pool are discussed. Finally, we will summarize the main results in Section 3.6.

2.3 Methods

2.3.1 Model

The high-resolution numerical simulation was performed with the Regional Ocean Modeling System (ROMS), a split-explicit, free-surface, terrain-following, hydrostatic, primitive equation [Song and Haidvogel, 1994, Shchepetkin and McWilliams, 2005]. The model domain covers the Northwest Atlantic Ocean (ROMS-NWA), extending from the Gulf of Mexico to the Gulf of St. Lawerence as shown in the background of Figure 3.1. The simulation period of the model ranges from year 1958 to 2007. The model's horizontal resolution is about 7 km on average. There are 40 vertical terrain-following levels, with water depth ranges from 10 m to 5500 m. The K-profile Parameterization (KPP) scheme was employed for vertical mixing in the boundary layer and ocean interior [Large et al., 1994].The background vertical mixing coefficient (m^2/s) for active tracer variables is about 1.0×10^{-6}. Initial and oceanic boundary forcing are both from the reanalysis data of Simple Ocean Data Assimilation version 2.1.6 [Carton and Giese, 2008]. Atmospheric forcing including air temperature, sea level pressure, humidity, wind, solar radiation, and precipitation are from the Coordinated Ocean-ice Reference Experiments (CORE.v2; 1948-2007) data sets. River runoff is implemented as freshwater flux input by estimating global river discharges [Dai et al., 2009]. Ten

major tidal components are also included, which were extracted from TPXO [Egbert and Erofeeva, 2002]. Standard circulation state variables, for example, temperature, salinity, and currents, are archived at a daily interval.

The ROMS-NWA model has been used to study eddy characteristics and energetics in the Gulf Stream region [Kang and Curchitser, 2013, 2015, Kang et al., 2016, Kang and Curchitser, 2017]. Our study only focuses on the MAB and GB shelf region that is far away from the open boundaries with depth between 20 m and 200 m, as indicated in the red box in Figure 3.1. The reason we include the GB region is because of the continuous shelf topography connecting the southern flank of GB and the New England shelf seaward from approximately 60-m isobath to the shelf break. The GB and the MAB continental shelf is dominated by a continuous current system with a mean clockwise (GB) and equatorward (MAB) along-shelf flow of 5-10 $cm \cdot s^{-1}$ over the mid- and outer-shelf, linearly correlated with topography, increasing offshore [Lentz, 2008a,b, Butman et al., 1982]. The GB is separated from the Scotian Shelf to the northeast by the Northeast Channel, which has a depth of about 230 m, and from the NS to the west by the Great South Channel, whose depth is around 70 m [Butman et al., 1982, Lentz et al., 2003]. The most prominent feature of the MAB is the HSV (marked as a star in Figure 3.1), an across-shelf valley that functions as a channel for across-shelf transport as well as a dynamical boundary for along-shelf flow [Gong et al., 2010].

2.3.2 Model Evaluation

To evaluate the model performance on the seasonal time scale in the continental shelf region, in particular in the MAB region, we compare the numerical simulations with four observational datasets: (1) trawl survey data (`www.nefsc.noaa.gov/epd/ocean/MainPage/ioos.html`), including sea surface temperature (SST), bottom temperature (BT) over the period of 1963-2007, calibrated by

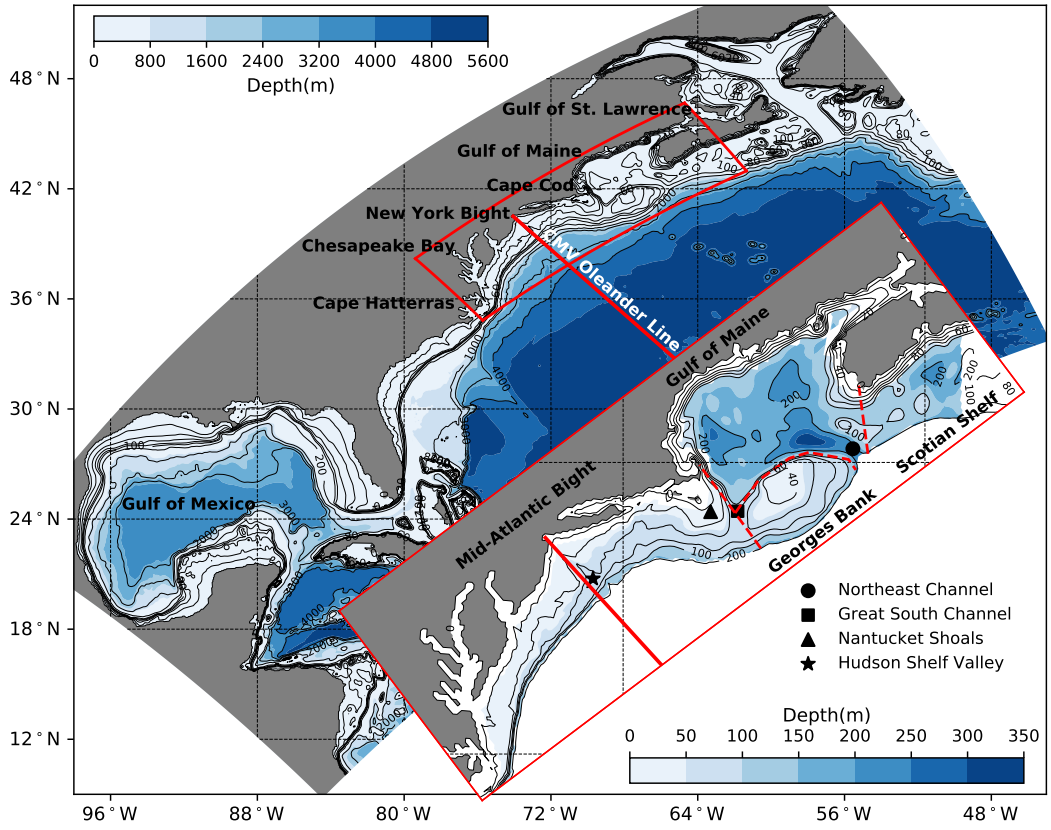

Figure 2.1: Bathymetry of the ROMS-NWA model domain (in the background; colorbar: upper left) and the study area (zoomed red box; colobar: lower right). Contours of the model domain are given every 20 meters from 0 to 100 m, every 100 meters from 100 to 200 m, and every 1000 meters from 1000 to 5000 m. Contours of the zoomed study area are given every 20 meters from 0 to 100m and every 100 meters from 100 to 200m. Red dashed lines denote boundaries between four sub-domains: the Middle Atlantic Bight, Georges Bank, Gulf of Maine, and Scotian Shelf with depth between 20 and 200 m. Position of the CMV Oleander Line is represented by a red thickened solid line. Special topography, such as the HSV, the NS, the Great South Channel, and the Northeast Channel are marked with different markers (shown in the lower right legend) in the zoomed red box.

Northeast Fisheries Science Center (NEFSC); (2) subsurface vertical temperature transections across the shelf from vessel *CMV Oleander* XBT datasets (`po.msrc.sunysb.edu/Oleander/XBT/NOAA_XBT.html`) between 1977 and 2007; (3) surface-to-bottom temperature and salinity profiles acquired by autonomous underwater glider vehicles (AUGV) from the Mid-Atlantic Regional Association Coastal Ocean Observing System (MARACOOS; `maracoos.org`) over the period of 2006-2007; and (4) MAB BT horizontal distribution and across-shelf temperature transections during 1979 from [Houghton et al., 1982].

2.3.2.1 Sea Surface and Bottom Temperature Comparison

The NEFSC trawl surveys provide long-term time series of SST and BT data that located within the MAB region over the period of 1963 to 2007. Here we calculate the climatological mean of the 45-year temperature datasets. Therefore, we focus on the seasonal time scale when comparing between observations and the model. Corresponding model values are interpolated using the Inverse Distance Weighting Method, as described in Appendix 2.8.1.

As shown in Figure 2.2a and 2.2b, the model exhibits significant skill in each season (represented by different colors in the figure). Linear regressions are performed and both regression lines fall close to the 1:1 ratio line, with slopes of 0.957 and 0.954, respectively. The 95% confidence intervals for SST and BT are also calculated, and few points are out of these intervals. The fractions (R^2) of the total sum of squares that explained by the regression for SST and BT are 0.965 and 0.828, respectively. Figure 2.2c shows the comparison of seasonal temperature time series between observations and the model. During the Cold Pool period (April to September), the model has an overestimate of 0.63 °C in SST and 1.78 °C in BT. The Root-Mean Square Error (RMSE) of SST and BT between model and observations are 1.09 °C and 2.14 °C, respectively. Although the model is biased warm, it captures the seasonal variations and the bias remains consistent

during the stratified seasons, with correlation coefficients reaching 0.99 and 0.94 for SST and BT, respectively.

2.3.2.2 Subsurface Temperature Comparison

We compare the model output with the vessel *CMV Oleander* XBT dataset over the period of 1977 to 2007. This data is collected frequently during round-trips between Elizabeth, New Jersey and Hamilton, Bermuda (Figure 3.1, and it provides temperature transects in the northwest Atlantic region including the continental shelf, the Slope Sea, the Gulf Stream as well as the northwestern Sargasso Sea. Here we only focus on the MAB shelf between the 40- and 100-m isobaths (Figure 3.3c). For the comparison, the model interpolation is performed using the Inverse Distance Weighting Method (Appendix 2.8.1). The dataset is separated into summer-stratified (May-October) and winter-mixed (November-April) seasons, as the Cold Pool exists during the stratified season and for comparison with the non-assimilative model performance in Wilkin and Hunter [2013].

Results show that the model captures the spatio-temporal variations in temperature over the continental shelf. During the summer-stratified seasons, the model overestimates the temperature by less than 1 °C near the surface, and by less than 1.5 °C in the subsurface layer. During winter-mixed seasons, the model overestimates the temperature by about 1 °C below the 20 m depth, and the temperature bias decreases toward the surface. The model overestimates the temperature by about 0.5 °C on average at depth above 20 m depth. The RMSE between the observation and model ranges from about 1 °C near the surface to around 1.5 °C in the subsurface during the winter seasons. The RMSE between the observation and model ranges from about 1 °C near the surface to less than 1.8 °C in the subsurface. The overall temperature bias and RMSE for both summer and winter seasons are comparable with and sometimes better than that of the non-assimilative model recorded inWilkin and Hunter [2013].

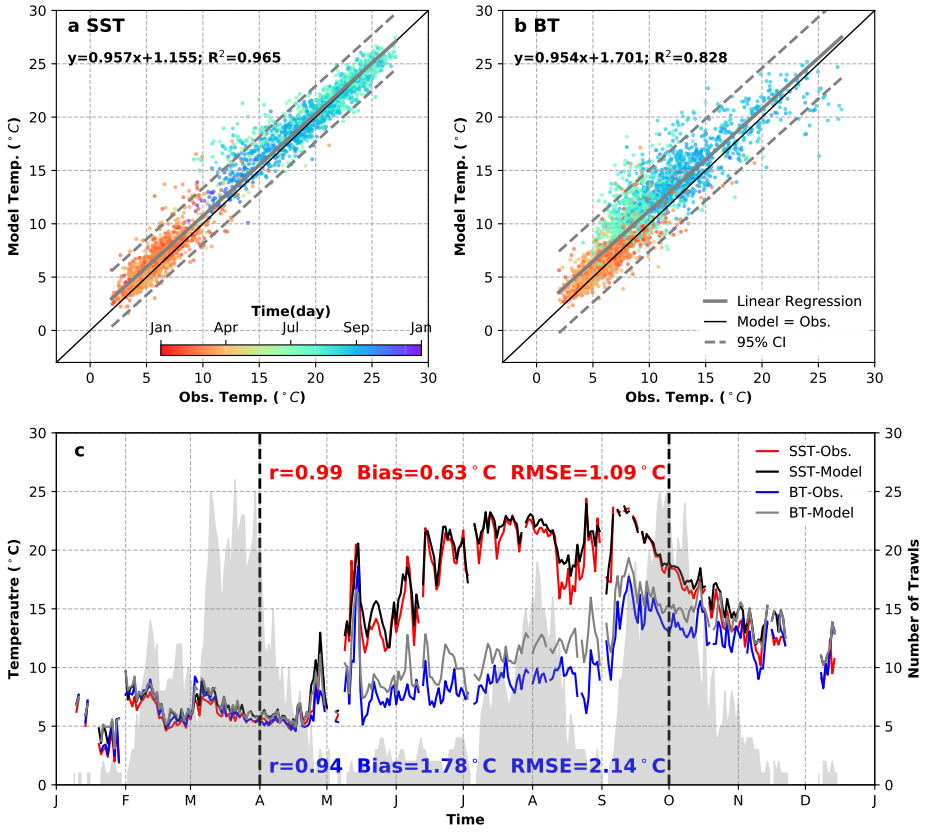

Figure 2.2: Scatter diagrams of interpolated model values versus observed values of (a) SST and (b) BT. The black diagnoal lines in (a) and (b) represent the 1:1 ratio of model values versus observed values. The gray thick solid lines represent the linear regression lines between observed values and model values. The dashed lines represent 95% confidence intervals. (c) Comparisons of climatological mean seasonal time series of observed and model SST/BT. The red (blue) lines represent observation of SST (BT); and the black and gray lines represent corresponding model values.

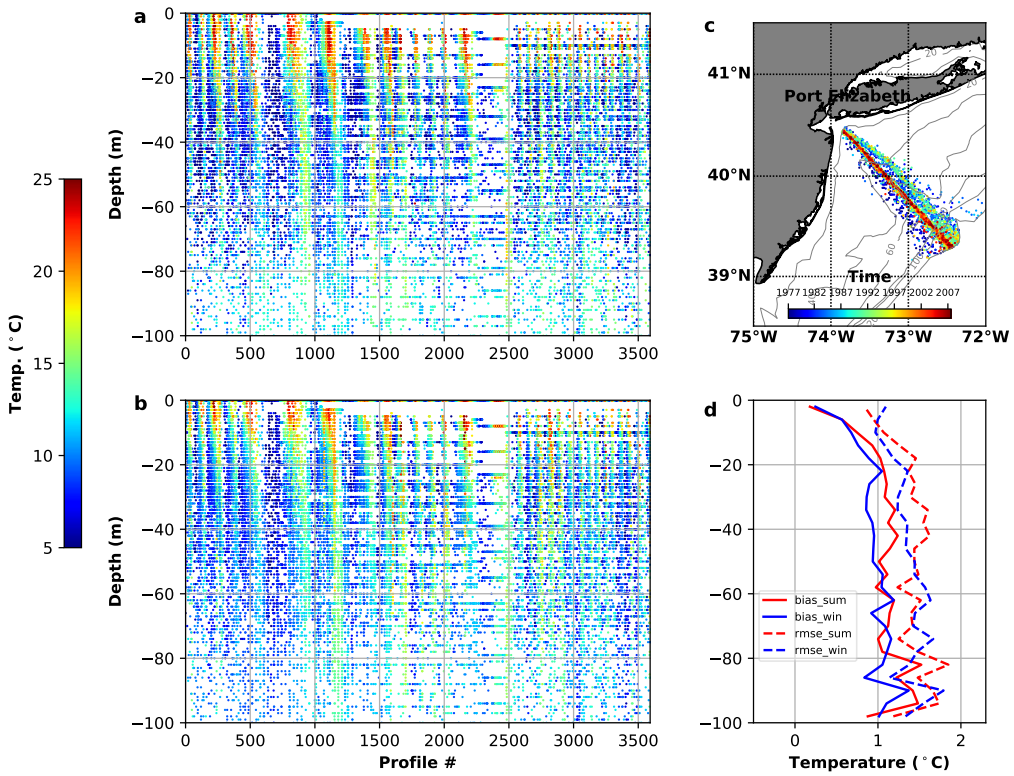

Figure 2.3: Comparisons of subsurface vertical temperature profiles between (a) CMV Oleander XBT observation and (b) the corresponding model interpolated values from 1977 to 2007 over the MAB shelf (between the 20- and 200-m isobaths). The x-axis represents profile number and y-axis represents depth. Profile numbers are in an ascending order of time. (c) Scatter plot of the XBT trajectories over the MAB shelf, with color representing time. (d) Vertical distribution of mean bias (model minus observation; solid lines) and RMSE (dashed lines) during summer-stratified (May-October; red) and winter-mixed (November-April; blue) seasons.

Further, we also perform model-observation comparison using high-resolution across-shelf AUGV profiles of temperature and salinity during the summers of 2006 and 2007, and BT distributions and across-shelf temperature transections from Houghton et al. [1982]. Results are presented in the Appendices 2.8.2 and 2.8.3. The four datasets combined form the basis of our model evaluation, which shows the model is able to successfully capture both temporal and spatial variability of the Cold Pool.

2.3.3 Quantification Method of the Cold Pool

Based on previous studies [Houghton et al., 1982, Fairbanks, 1982, Brown et al., 2012, Lentz, 2017], the Cold Pool is considered as a relatively cold and fresh water mass cooler than 10 °C located over the mid- and outer-shelf of the MAB below the seasonal thermocline during stratified season. Following this definition, three criteria are applied to capture and quantify the Cold Pool:

1. Temperature & Salinity Criteria: The temperature of the Cold Pool is defined to be lower than 10 °C [Houghton et al., 1982, Fairbanks, 1982, Brown et al., 2012, Lentz, 2017]. Because of the tendency of the model to be slightly warm biased, we also explore the 11 and 12 °C as temperature criteria for the Cold Pool. Those results do not change the nature of the results presented here and are presented, for completeness, in Appendix 2.8.4. In this study, we applied the temperature criterion to capture the colder part of the observed Cold Pool since we are concerned more about its evolution, possible source and the Cold Pool core movement than calculating its precise volume. Ultimately, this approach (rather than de-biasing the model results) allows us to maintain full dynamical balances in a situation with limited temporal and spatial observational datasets in the region.

Additionally, as part of the MAB shelf water, salinity of the Cold Pool water is identified to be less than 34 *psu* [Mountain, 2003]. For some shelf-break regions,

there is a *Salinity Maximum Layer* [Gordon and Aikman, 1981, Fairbanks, 1982] in the mid-water column, considered to be intrusions of salty Slope Water onto the shelf. This phenomenon was also captured in the vertical AUGV temperature and salinity profiles during the summer of 2007 (Figure 2.15). High-salinity (above 34 psu) low-temperature (around 8 °C) waters intruded onto the shelf at a depth of 30 m. The threshold value for salinity (34 psu) to separate the Slope Water from the Cold Pool is based on the research of MAB shelf water properties over the period of 1977 to 1999 [Mountain, 2003].

2. Stratification Criterion: The Cold Pool develops along with the onset of thermal stratification of the water column. If the water column is well-mixed, it is not considered as Cold Pool water even though the temperature is below 10°C. According to Li et al. [2015], density stratification over the MAB region is thermally controlled throughout most of the year. Therefore, stratification is determined by calculating the mixed layer depth (MLD) based on vertical temperature profiles. The criterion selected for calculating the MLD is a threshold value of temperature (δT=0.2°C) from that at 10 m depth [de Boyer Montégut et al., 2004]:

$$D_m = z_{min}(T(z = Z_{ref}) - \delta T) \tag{2.1}$$

$$Z_{ref} = 10m; \delta T = 0.2°C \tag{2.2}$$

where D_m represents the depth of the mixed layer base and z is positive upward.

3. Location Criterion: In the vertical, the Cold Pool stays below the MLD, with no direct contact with the air-sea interface. In the horizontal direction, we only consider regions within the MAB that are between the 20 and 200 m isobaths as shown in Figure 3.1.

By applying these three criteria to the ROMS model output and its climatology, we quantified the Cold Pool seasonal evolution and variations in its volume, temperature, salinity, density and progression velocity. We analyze these Cold

Pool state variables to develop insight into the Cold Pool characteristics in both the along-shelf and across-shelf directions, as well as at different time scales. In this study, we focus on the seasonal time scale. The inter-annual variability and long-term trends of the Cold Pool are the subject of subsequent work.

2.4 Seasonal Variability of the Cold Pool

We use the high-resolution space- and time-continuous hindcast solutions to characterize the Cold Pool seasonal variability over the MAB continental shelf.

2.4.1 Timing and Spatial Patterns

First, we focus on the timing and spatial distribution of the Cold Pool on the seasonal time scale (Figure 2.4), by applying the Cold Pool Quantification method (Section 3.3.3) on the climatological model solution from 1958 to 2007. The Cold Pool is a continuous and persistent feature throughout the stratified months. The spatial distribution of the Cold Pool suggests significant seasonal variability. It typically experiences an *onset* - *peak* - *decline* period during its annual cycle. From a climatological perspective, it first emerges around early April (day 95), reaches the maximum volume ($2.25\times10^3 km^3$) around mid-May (day 139) and slowly disappears around mid-September (day 256). The Cold Pool persistence is about five and a half months (162 calendar days).

With the enhancement of surface warming and the onset of stratification in the spring, the Cold Pool begins to develop below the MLD in the inner-shelf (20-40 m isobath) region off the New Jersey coast, with an average temperature around 6 °C on calendar day 100 (Figure 2.4). Later, the Cold Pool expands its volume both up-shelf and down-shelf as well as in the offshore direction. Within less than a month, the Cold Pool reaches its southernmost point and its southern extent begins to retreat northward due to warming and mixing in the southern MAB

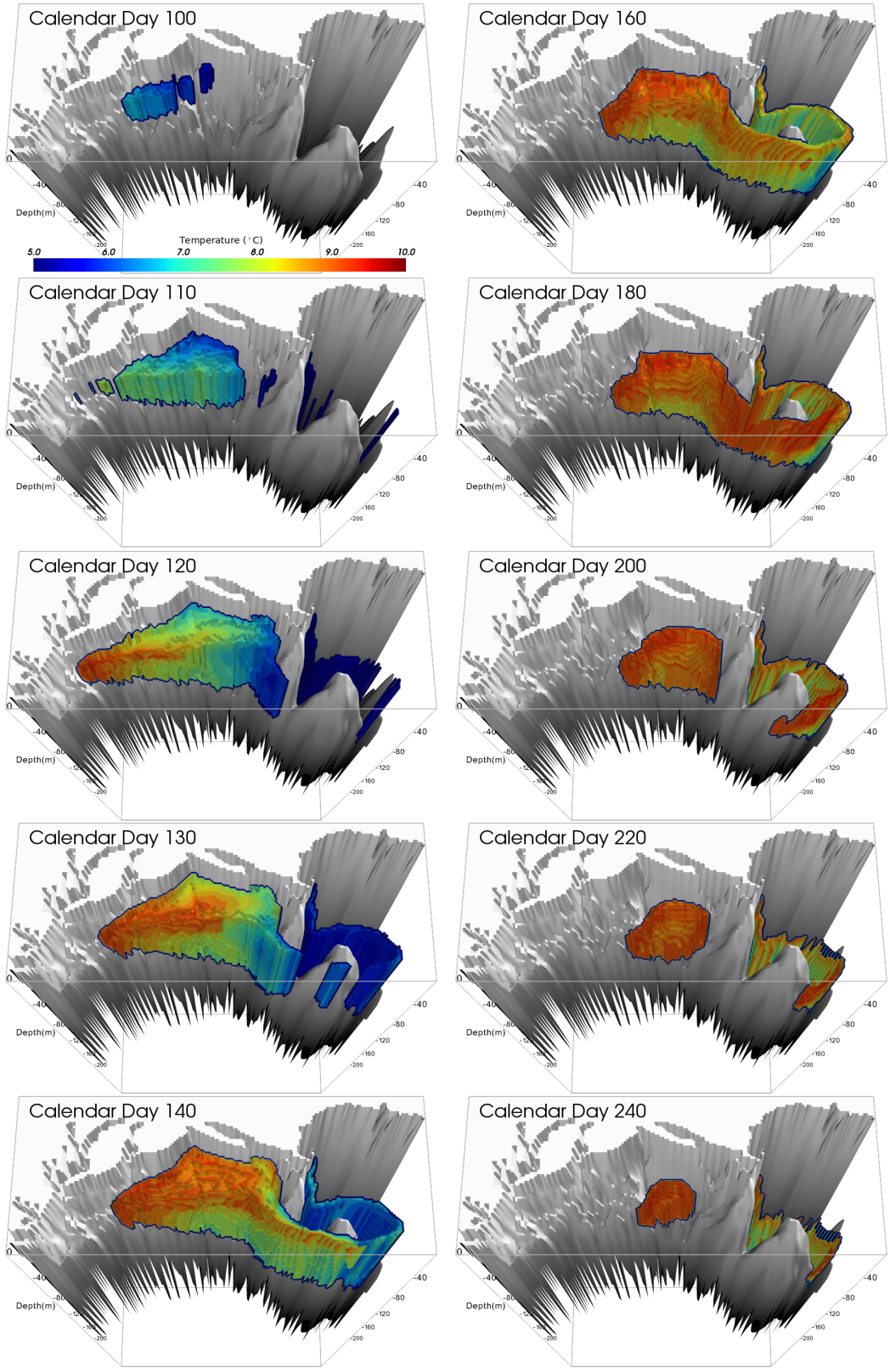

Figure 2.4: Three-dimensional profiles of the Cold Pool temperature on calendar day 100, 110, 120, 130, 140, 160, 180, 200, 220, and 240 after applying the Cold Pool Quantification method on the 50-yr (1958-2007) climatology model solution.

region. Meanwhile, the northern extent of the Cold Pool continues to expand up-shelf with the development of stratification until it gets connected with the sub-MLD cold and fresh waters of GB on the outer-shelf between the 80-100 m isobaths (Figure 2.6). The initial expansion of the Cold Pool is due to the spatial patterns and temporal evolution of the development of the thermal stratification in the MAB. The subsequent retreat is associated with warming of the Cold Pool, so that it exceeds the threshold value of the temperature criterion - 10 °C.

After calendar day 140, the Cold Pool's total volume begins to decrease due to enhancement of surface warming (Figure 2.4). The most prominent decrease in volume is located in the relative-shallow regions including the southern MAB and the inner-shelf region of the MAB (Figure 2.6). The southern edge of the Cold Pool quickly retreats northward between calendar days 140 and 180. Simultaneously, due to cumulated warming and strong mixing near the Nantucket Shoals and the southern flank of GB, the Cold Pool begins to break-down near the Great South Channel on calendar day 180. The Cold Pool becomes a horizontally-isolated water mass enclosed by warmer temperatures in all directions. The horizontally isolated Cold Pool continues to diminish and finally disappears near of the Hudson Shelf Valley.

After calendar day 140, the Cold Pool's total volume begins to decrease due to enhancement of surface warming (Figure 2.4). The most prominent decrease in volume is located in the relatively shallow regions including the southern MAB and the inner-shelf region of the MAB. The southern edge of the Cold Pool quickly retreats northward between calendar days 140 and 180. Simultaneously, due to cumulated warming and strong tidal mixing near the NS and the southern flank of GB, the Cold Pool begins to break-down near the Great South Channel on calendar day 180. The Cold Pool becomes a horizontally-isolated water mass enclosed by warmer temperatures in all directions. The horizontally isolated Cold Pool continues to diminish and finally disappears near of the HSV.

Based on the Cold Pool's characteristics during its *onset - peak - decline* annual cycle, we defined three stages representing its evolution. These stages are also plotted with different colors in the background of Figure 2.5. Stage I is a Cold Pool volume-expanding stage from the onset (calendar day 95) to the peak of the Cold Pool volume (calendar day 139). This is the stage when the Cold Pool begins to develop as well as the onset of the water column stratification. The total volume of the Cold Pool has a fast expansion from zero to the maximal total volume during Stage I (44 days) (Figure 2.5a). Seasonal variation of the Cold Pool volume distribution in the along-shelf direction in Figure 2.5e suggests the maximum volume contribution comes from the south of NS - the NES, (+871 km^3), which is considered as the winter remnant source water of the Cold Pool [Houghton et al., 1982]. The secondary volume contribution is from the Northern NYB (NNYB, +822 km^3). During this stage, across-shelf-averaged upper boundary of the Cold Pool reaches as high as 12 m depth in the Southern MAB (SMAB), and gradually deepens to 18 m in the NES region (Figure 2.5b and 2.5f). The depth of lower boundary also deepens from 30 m in the SMAB to 60 m in the NES region (Figure 2.5c and 2.5g).

Both Stages II and III are volume-decreasing stages and have a northward retreat of the Cold Pool southern edge. The splitting point is selected to be calendar day 180 for the climatological case, when the Cold Pool starts to become a horizontally-isolated water mass. During Stage II, decrease of Cold Pool volume happens with even contributions from the Southern NYB (SNYB, -319 km^3), NES (-313 km^3) and NNYB (-282 km^3) regions (Figure 2.5e). Among these three regions, SNYB has the largest deepening of both upper (13.2 m) and lower (14.3 m) boundaries, and the NES has the minimum deepening (upper: 8.3 m; lower: 5.0 m) on average. During Stage III, the maximum volume decrease is controlled by the NES (559 km^3) and NNYB (539 km^3) regions. The upper boundaries of all three regions keep deepening during Stage III. For the lower boundaries, unlike

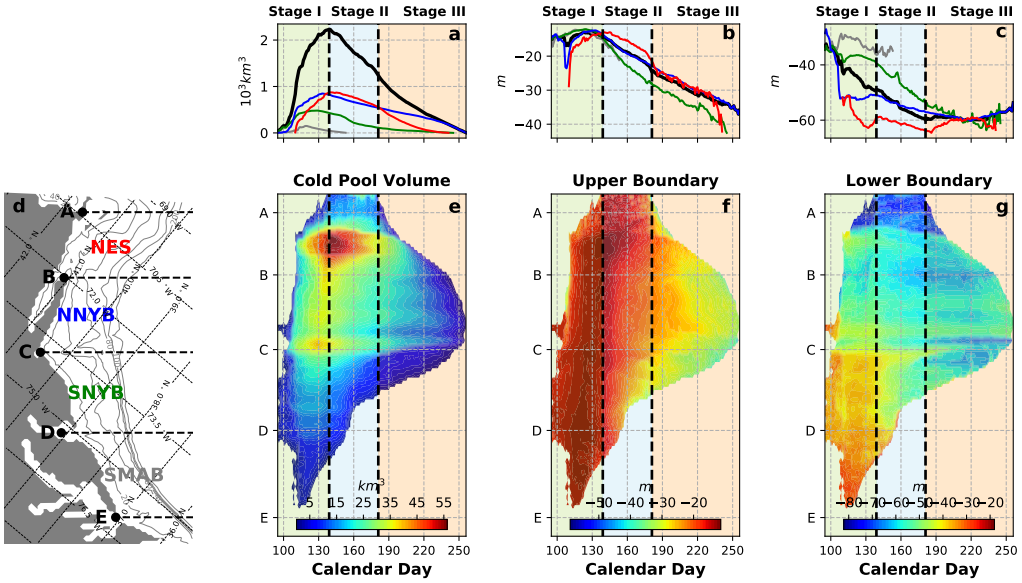

Figure 2.5: One-dimensional time series of the Cold Pool (a) total volume (km^3), and the depth of (b) upper boundary and (c) lower boundary (m) over the Mid-Atlantic Bight (MAB, black), New England Shelf (NES, red), Northern New York Bight (NNYB, blue), Southern New York Bight (SNYB, green) and Southern Mid-Atlantic Bight (SMAB, gray). The three stages of the Cold Pool event - Stage I, II, and III, are separated by black dashed lines and represented by different colors in the background. Panel (e) shows the geographical locations in the along-shelf direction: A - the Nantucket Shoals, B - the Montauk Point, C - the Sandy Hook, D - the Delaware Bay, E - the Chesapeake Bay. The rest three panels show the seasonal variation of the Cold Pool (f) total volume, (g) upper boundary depth, (h) lower boundary depth in the along-shelf direction.

NNYB and SNYB, the NES region shallows from 65 m to 59 m depth during the first half of the Stage III, coincidental with the retreat of the northern extent.

2.4.2 Cold Pool Temperature and Salinity

We quantify the seasonal variability in the horizontal structures of the Cold Pool temperature, salinity, and currents, and compute respective depth-averaged quantities (Figure 2.6). The depth-averaged fields of temperature and salinity highlight that the Cold Pool is not a horizontally well-mixed water mass during most of its timespan. In the early volume-expanding stage, the temperature gradient is mainly along-shelf. For example, on calendar day 120, the depth-averaged temperature of the Cold Pool in the south New England Shelf is approximately 6 °C, increasing in the equatorward direction. Following, the across-shelf temperature gradient becomes as pronounced as the along-shelf gradient until the horizontal temperature difference finally vanishes after calendar day 240 (Figure 2.6). For the depth-averaged salinity of the Cold Pool, the horizontal structure shows different patterns than temperature. Across-shelf salinity gradient is strong throughout the stratified season. In general, it is relatively fresh near the coastline as a result of local river discharge, with a salinity of 32.5 psu, increasing offshore to a maximum value of 34 psu (which we define as the boundary to separate the Slope Water on the shelf-break).

The warming rate of the Cold Pool minimum temperature varies among regions (Figure 2.7a). The SMAB region has the maximum rate during Stage I (1.80 °C/month) and Stage II (1.44 °C/month). Among the rest of the three regions, the NES has the minimum warming rate (1.41 °C/month) during Stage I, NNYB has the minimum warming rate (0.30 °C/month) during Stage II, and SNYB has the minimum warming rate (0.48°C/month) during Stage III. Regional variations in warming rates indicates an equatorward migration of the Cold Pool.

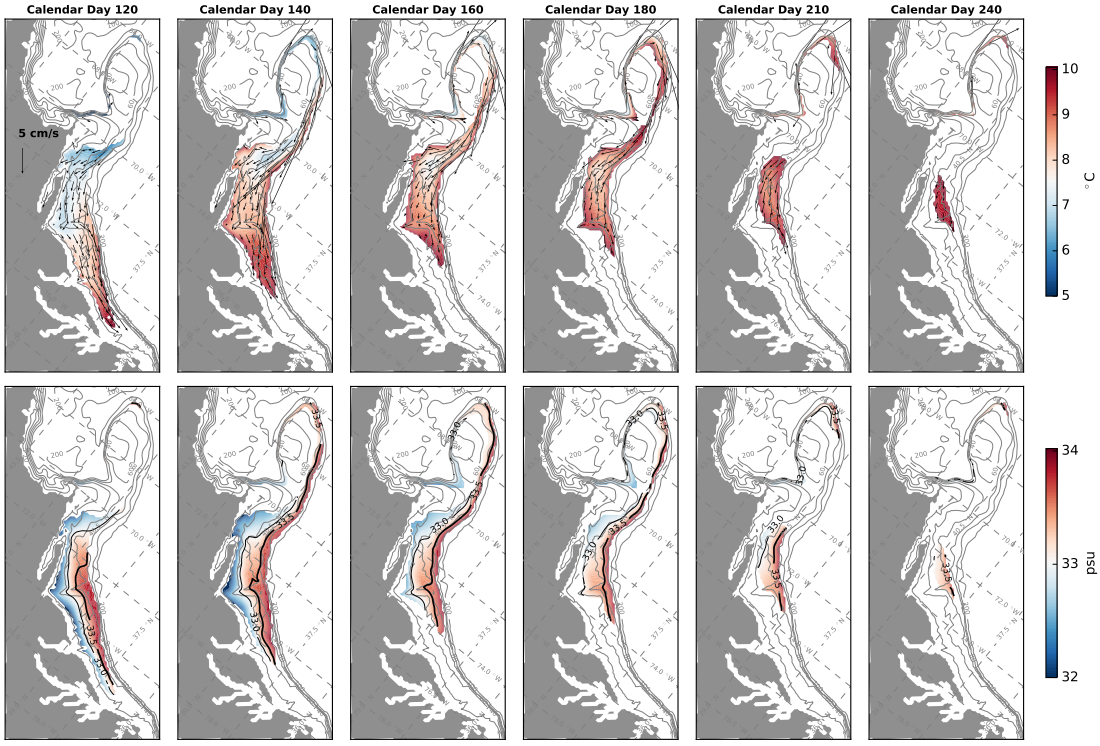

Figure 2.6: Depth-averaged temperature and currents (upper panels) and depth-averaged salinity (lower panels) of the Cold Pool over the MAB and GB shelf region on calendar day 120, 140, 160, 180, 210, and 240 based on the 50-yr climatology model result. The 33- and 33.5-psu isohalines are plotted in black solid lines in the lower panels, and the 33.5-psu isohaline is thickened.

Similarly, the salting rates of the Cold Pool minimum salinity also vary regionally, except during Stage I, when all four regions have a freshening process due to the increase of river runoff in the spring (Figure 2.7b). During Stage II, salting rates increase from the NES to the SMAB, which are 0.68, 0.69, 0.78 and 1.52 psu/month, respectively. During Stage III, the minimum salting rate is in the NNYB (0.24 psu/month) and SNYB (0.22 psu/month) regions. The NES has a slightly higher salting rate of about 0.31 psu/month.

To further evaluate the Cold Pool temperature's seasonal variability, we calculate the Cold Pool minimum temperature and salinity in the along-shelf direction and compute the Cold Pool cores (defined as minimum depth-averaged Cold Pool temperatures). The seasonal variation of the Cold Pool minimum temperature suggests that initially there are two main cold water sources (Figure 2.7e). One is located in the north of the HSV, with the initial temperature obtained as low as 5.1°C on calendar day 95; the other is located between A and B - in the south of the NS, with the lowest temperature approximately at 5.6 °C on calendar day 110 (Figure 2.7e). The southern cold water source is quickly warmed and its southward traveling path is hard to identify south of the HSV. However, for the northern cold source, the Cold Pool cores move southward, with warming rates about 0.04 °C/day during Stage I and 0.03 °C/day during Stages II and III, which is consistent with values reported in Houghton et al. [1982] and Lentz [2017] (about 1 °C/month). Following these Cold Pool cores, we can track the coldest water patch traveling down the shelf for the duration of the Cold Pool event. The along-shelf traveling velocity of the Cold Pool cores are about 2.6 cm/s during Stage II and about 2 cm/s during Stage III (Figure 2.7c and 2.7g).

The Cold Pool minimum salinity is mainly located on the inner shelf of the New York Bight (from B - the Montauk Point to D - the Delaware Bay) and south of the NS (between A and B) with values as low as 31.4 psu during Stage I (Figure 2.6). There is a large increase in the Cold Pool minimum salinity

during Stage II, from 31.5 psu on calendar day 145 to 32.3 psu on calendar day 160. This quick increase in minimum salinity is possibly associated with mixing due to upwelling-favorable winds, which leads to Cold Pool volume shrinkage of relatively fresh water in the inner shelf of the New York Bight. Because of mixing with offshore Slope Water, the Cold Pool minimum salinity increases at a rate of 0.27 psu/month during Stage III. The Cold Pool salinity minima, however, do not have such a clear down-shelf traveling path as the temperature minima except during Stage III (Figure 2.7f). The salinity-minimum path started from the latter half of Stage II indicates that there may be an upstream input of water to the Cold Pool.

2.4.3 Southwestward Progression of the Cold Pool

We investigate the temporal evolution of the Cold Pool by tracking its extent and location of the Cold Pool cores on specific calendar days (Figure 2.8). The horizontal distribution of the Cold Pool cores suggests that it is initially located south of New England during Stage I. Given the Stratification Criterion, the Cold Pool emerges after calendar day 115 (north of the NS is well mixed before then; Figure 2.7). The Cold Pool cores propagate continuously southwestward along the 60-m isobath with an average speed of approximately 2.0 cm/s (Figure 2.8). We observe that the retreat speed of the Cold Pool southern extent varies in time. The southern extent first expands southward and reaches its southernmost point on calendar day 115 due to development of stratification. Then, it retreats quickly at an average speed of 6.39 cm/s from calendar day 115 to 155, due to enhanced warming and mixing in the relatively-shallow southern MAB region. Then, it retreats more slowly at an average speed of 1.71 cm/s between calendar day 175 and 235. The slow-down of the southern boundary retreat suggests it could be related to the advection of Cold Pool water, which overcomes the surface warming and mixing (see discussion in Section 3.5).

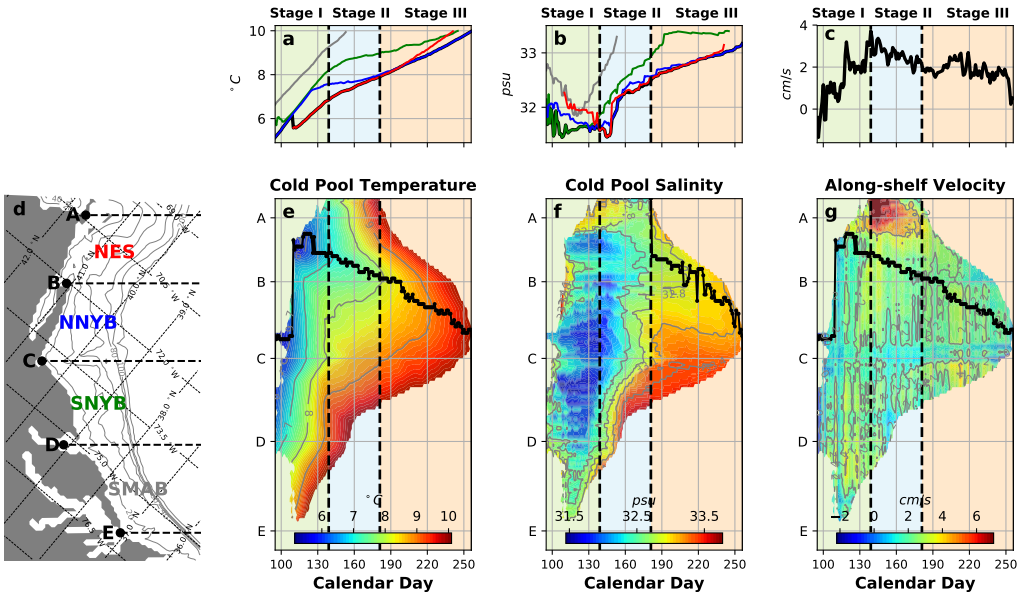

Figure 2.7: One-dimensional time series of the Cold Pool (a) minimum temperature (°C) and (b) minimum salinity (psu) over the MAB (black), NES (red), NNYB (blue), SNYB (green) and SMAB (gray), and (c) along-shelf velocity (m/s) of the Cold Pool cores. The lower four panels are the same as Figure 2.5, but show the seasonal variation of the Cold Pool (e) minimum temperature, (f) minimum salinity, and (g) along-shelf velocity in the along-shelf direction. Locations of the Cold Pool minimum temperature in the along-shelf direction on each calendar day are marked as black dots in panel (e) and (g). Similarly, locations of the Cold Pool minimum salinity in the along-shelf direction on each calendar day of Stage III are marked as black dots in panel (f).

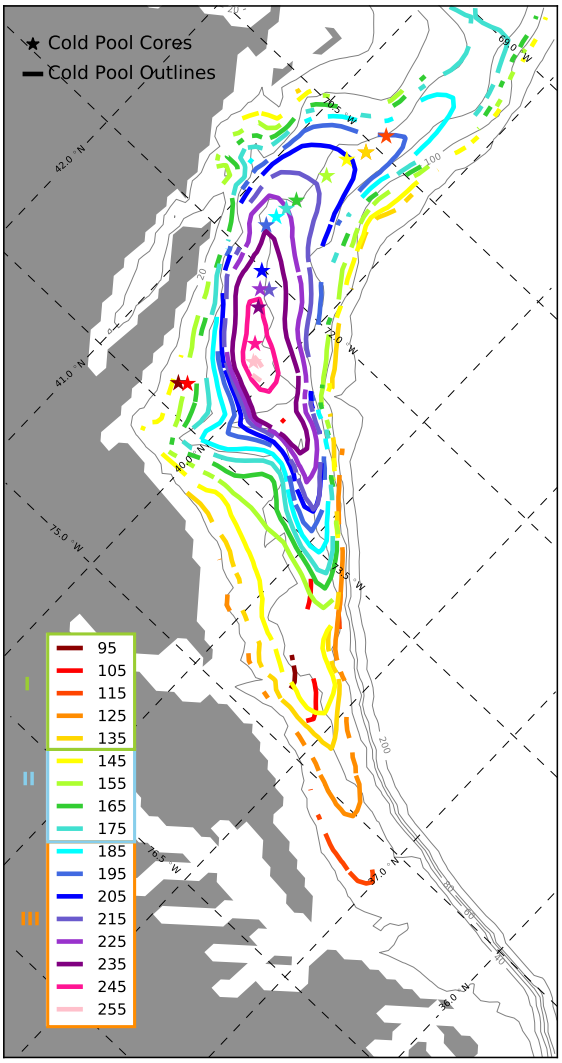

Figure 2.8: The horizontal extents (contours) and positions of the Cold Pool cores (stars) of the Cold Pool on calendar days from 95 to 255, every 10 days per contour/star, represented by different colors.

In contrast, the northern extent of the Cold Pool retreats faster than the southern edge from the initiation of Stage III. Estimated from the contours on calendar days 175 to 235, the northern edge retreats approximately 2.6 times faster than the southern boundary, at an average speed of 4.46 cm/s (Figure 2.8). This suggests that horizontal advection has different impact on the northern and southern Cold Pool boundaries retreat speed. The upstream water at the southeast corner of GB exhibits enhanced warming and mixing. The down-shelf advection of this water mass in the northeast of the MAB then warms the Cold Pool. In the southern edge of the Cold Pool, the down-stream advection of the Cold Pool water supresses temperatures. A detailed quantitative investigation of the relative importance of advection versus vertical mixing is discussed in Section 3.5.

2.5 Cold Pool Heat Budget

We investigate the heat balance of the near-bottom layer, where the Cold Pool is located. We divide the water column into two layers at a depth of 30 m and consider the bottom layer over the mid- and outer-shelf.

2.5.1 The Depth-averaged Heat Budget

We time- and depth-average the heat balance terms of the near-bottom layer for Stages I, II, and III over the MAB and GB continental shelves in order to quantify the relative contributions of the advective heat flux and the downward diffusion of heat from the surface layer during the Cold Pool evolution (Figure 2.9). Neglecting horizontal diffusion, the depth-averaged heat balance of the near-bottom layer can be written as:

$$\underbrace{\frac{1}{h_b}\int_{\eta}^{\xi_{30}} \frac{\partial T}{\partial t}\, dz}_{\text{Qtrend}} = \underbrace{\frac{1}{h_b}\int_{\eta}^{\xi_{30}} K_v\, \frac{\partial^2 T}{\partial z^2}\, dz}_{\text{V-Diffusion}} \underbrace{- \frac{1}{h_b}\int_{\eta}^{\xi_{30}} (\boldsymbol{u}\cdot\nabla T + w\frac{\partial T}{\partial z})\, dz}_{\text{Advection}} \quad (2.3)$$

where T represents temperature (°C), $\boldsymbol{u}$ is horizontal velocity vector (m/s), and w is vertical velocity (m/s), K_v is the vertical diffusion coefficient (m^2/s), h_b is water depth of the bottom layer below the 30-m depth, ξ_{30} refers to the 30-m depth separating the surface layer and the bottom layer and η represents the physical bottom. Equation (2.3) states that time rate of change in the heat storage of the near-bottom water column is balanced by the vertical diffusion from the upper layer and horizontal and vertical advective heat fluxes.

We first examine the instantaneous rate of change averaged over the three stages of the Cold Pool. Spatial patterns of heat budget terms highlight the importance of advection in regulating the geographical difference in warming rates during the three stages (Figure 2.9).

For the bottom layer, warming rates of vertical diffusion from the surface layer (depth above 30 m) have a distinct difference between the Georges Bank-Nantucket Shoals (GBNS) region (shallow regions within the 80-m isobath of GB and within 60-m isobath of the NS) and the rest of the domain. The warming effect of vertical heat diffusion from the surface layer is increasing over the GBNS region during the three stages (Stage I-III: +0.07, +0.14, +0.20 °C/day on average). However, the rest of the domain has a consistent warming rate of approximately +0.02 °C/day on average from vertical heat diffusion, with slightly higher values towards the coast.

Similarly, the spatial pattern of the advective heat flux for the bottom layer also has a distinct difference between the GBNS region and the rest of the domain. Except the crest of GB, heat advection over the GBNS region has an enhancing cooling effect during the three stages (Stage I-III: -0.02, -0.07, -0.15 °C/day on average). Accordingly, the outer-shelf of the GBNS region (80-to-200 m isobath of GB and northern MAB) has an enhancing warming effect during the three stages (Stage I-III: +0.01, +0.02, +0.03 °C/day on average). Especially over the mid-shelf (between 60- and 80-m isobaths) of northern MAB, heat advection turns

from a cooling effect (-0.01 °C/day) during Stage I to a warming effect (+0.03 °C/day) during Stage III. Therefore, the spatial difference in heat advection, accompanied by the consistent warming pattern from vertical heat diffusion, plays an important role in regulating the spatial pattern of warming trends of the bottom layer.

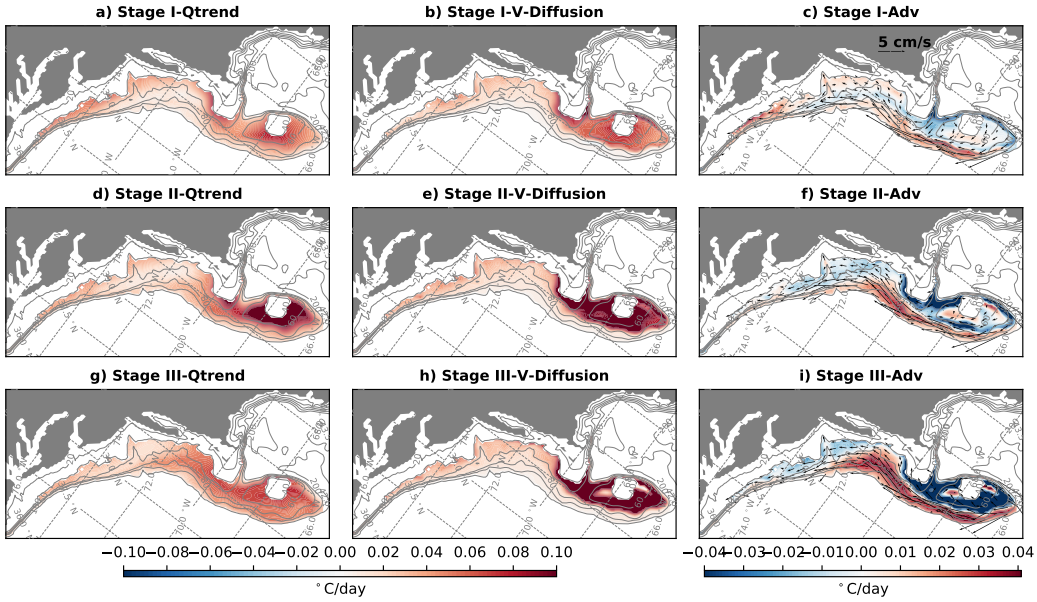

Figure 2.9: The depth-averaged heat budget (unit: °C/day) of the bottom layer (below 30-m depth) over the MAB and GB continental shelf, averaged during the three stages of the Cold Pool based on equation 2.3: (a, d, g) heat trend (Qtrend), (b, e, h) vertical heat diffusion from the surface layer (V-Diffusion), (c, f, i) heat advection (Adv).

2.5.2 Three-dimensional Heat Budget

We investigate the warming/cooling effects of the advective term in both the horizontal and vertical directions. The MAB continental shelf is split into three near-bottom subdomains and we then compute heat balance within each control volume. The three subdomains are the same as those in Figure 2.5 and 2.7, below the 30 m depth. Note that between 40- to 100-m isobaths and the GBNS regions are not included (Figure 2.10a). Neglecting the horizontal diffusion term, the heat

budget equation for a control volume in the near-bottom layer can be expressed as:

$$\underbrace{\frac{1}{V}\int_V \frac{\partial T}{\partial t}\,dV}_{\text{Qtrend}} = \underbrace{\frac{1}{V}\int_V K_v\,\frac{\partial^2 T}{\partial z^2}\,dV}_{\text{V-Dif}} \underbrace{-\ \frac{1}{V}\int_V u\frac{\partial T}{\partial x}\,dV}_{\text{X-Adv}} \underbrace{-\ \frac{1}{V}\int_V v\frac{\partial T}{\partial y}\,dV}_{\text{Y-Adv}} \underbrace{-\ \frac{1}{V}\int_V w\frac{\partial T}{\partial z}\,dV}_{\text{Z-Adv}} \tag{2.4}$$

where T represents temperature, (u, v, w) represent three-dimensional velocities, and K_v is the vertical diffusion coefficient (m^2/s), V is total volume of the control volume. The volume-averaged heat budget equation states that time rate of change in heat storage is balanced by vertical heat diffusion from the upper layer and the advection of heat from three different directions. The cumulative heat balance of Equation (3.2) can be expressed as:

$$\int_{t_0}^{t} \text{Qtrend}\ dt' = \int_{t_0}^{t} \text{V-Dif}\ dt' + \int_{t_0}^{t} \text{X-Adv}\ dt' + \int_{t_0}^{t} \text{Y-Adv}\ dt' + \int_{t_0}^{t} \text{Z-Adv}\ dt' \tag{2.5}$$

where t_0 is the initial time for time integrating.

The cumulative heat budgets of the three subdomains suggest that, during the stratified seasons, warming of the near-bottom layer is positively influenced by vertical diffusion and vertical and along-shelf advection of heat. Across-shelf advection of heat in the NNYB and SNYB regions contribute negatively (Figure 2.10). The NES region has opposite contributions from the x- and y-direction advection terms. Among the three subdomains, SNYB region has the largest residuals (horizontal diffusion), which is about 0.2 °C/month during Stage II and III (Figure 2.10).

We calculate average warming/cooling rates of each heat budget term within each stage for the three subdomains (Figure 2.11). In the vertical direction, vertical diffusion of heat from the upper layer is consistent and nearly constant for the three subdomains throughout the stratified seasons (about 0.6 °C/month). In the NES and NNYB region, vertical diffusion warms the near-bottom layer at warming rates of 0.5, 0.6, 0.6 °C/month for the three stages, respectively. In

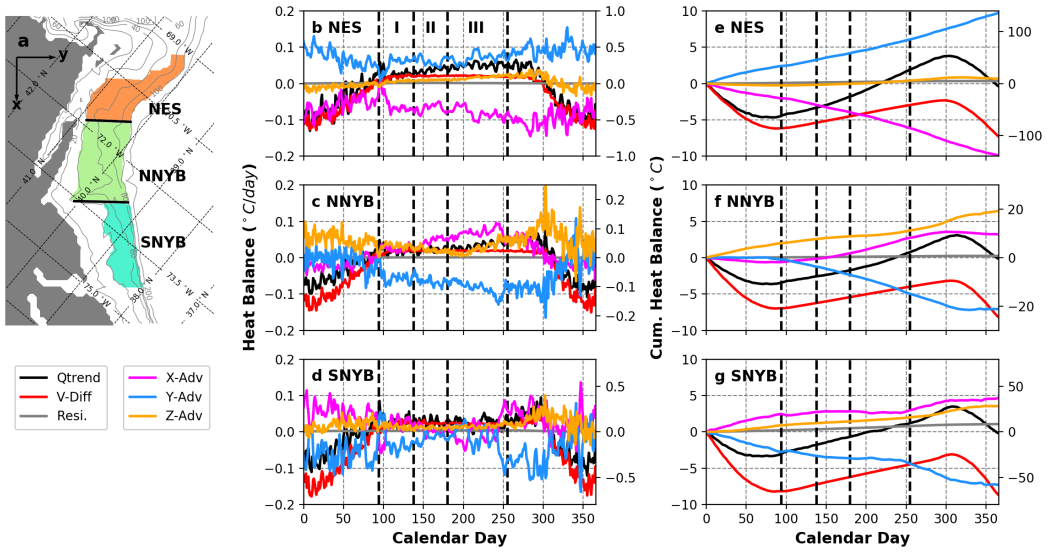

Figure 2.10: (a) Locations of the three subdomains/control volumes (NES, NNYB, SNYB) between 40- to 100-m isobaths and below the 30-m depth, represented by different colors. The positive direction of x-axis is towards the down-shelf direction, and the y-axis is towards the across-shelf direction, as shown in this panel. (b)-(d) Volume-averaged heat budget (°C/day) of these three control volumes based on Equation 3.2. (e)-(g) Cumulative heat budget of the three control volumes based on Equation 3.3. For the advective terms, X-Adv, Y-Adv and Z-Adv, their y-axis are on the right hand side of each panel. Different heat budget terms are plotted in different colors, as show in the legend boxes.

the SNYB region, vertical diffusion has slightly higher warming rates of 0.6, 0.7, 0.7 °C/month for each stage. Therefore, if we consider vertical diffusion as the only source of heat for the near-bottom layer, there will not be any geographical difference in the net warming rates and the Cold Pool, the NES and NNYB will all warm at the same rate.

However, the net warming rates of the three near-bottom regions vary significantly throughout the three stages (Figure 2.11). During Stages I and II, the NNYB region has a minimum Qtrend of about 0.6 °C/month. The NES and SNYB regions have higher warming trends (NES: 0.8, 1.1 °C/month; SNYB: 0.9, 0.8 °C/month). During Stage III, warming trends decrease from 1.5 °C/month in the NES, to 1.0 °C/month in the NNYB, to 0.8 °C/month in the SNYB. These geographical differences are consistent with observations of temperature in each subdomain, indicating that vertical diffusion of heat from the upper layer is not the dominant process.

In the NES region, the warming of the near-bottom layer during the three stages is mainly due to an increase of vertical advection of heat from the top layer. Vertical diffusion is nearly constant throughout the three stages. X-advection balances Y-advection, with the total horizontal advection (X- plus Y-advection) having an enhanced cooling effect from -0.5, to -1.0, to -1.6 °C/month during the three stages. However, the warming effect from the vertical advection increases at a faster rate from +0.7 to +1.4, to +2.4 °C/month. Therefore, the warming trend of the near-bottom NES increases from +0.8, to +1.1, to +1.5 °C/month.

In the NNYB region, the near-bottom warming trend is consistently low during the first two stages (+0.6 °C/month). Again, the vertical diffusion term is almost the same throughout the three stages. Vertical advection of heat balances with the horizontal advection during the first two stages. Unlike the NES region, the cooling effect of horizontal advection decreases from -1.1 to -0.8 °C/month. The warming effect of vertical advection also decreases from 1.2 to 0.8 °C/month

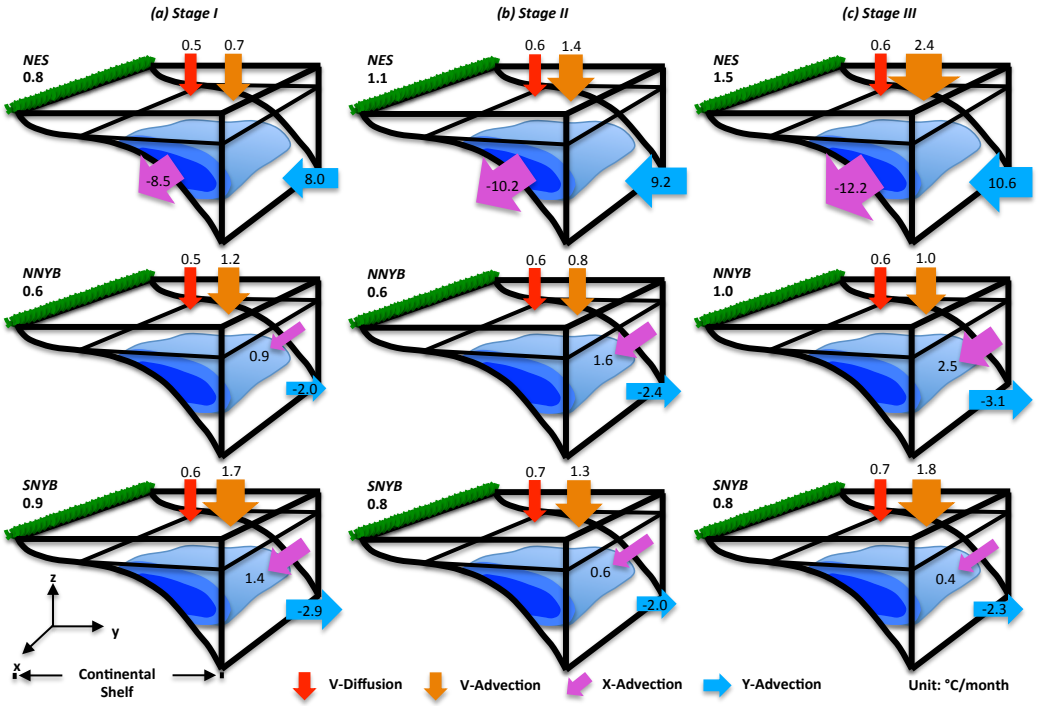

Figure 2.11: Schematic figures of heat balances for the three near-bottom subdomains - NES, NNYB, SNYB during (a) Stage I, (b) Stage II and (c) Stage III. The black bold numbers on the upper left corner of each panel represent warming rate of the control volume (left-hand term of Equation 3.2). The four right-hand heat budget terms of Equation 3.2 are represented by arrows in different colors. Positive numbers indicate warming effect, and negative values mean cooling effect.

because more heat is trapped in the upper surface layer. This is associated with a stronger stratification. Decrease of the cooling effect from horizontal advection is due to an increase in the X-advection term from 0.9 to 1.6 °C/month, larger than the increase in the Y-advection from -2.0 to -2.4 °C/month. The warming trend increases to 1.0 °C/month during the third stage. This is due to a larger increase of heat advection in the x-direction to 2.5 °C/month, and the cooling effect of horizontal advection is decreasing from -0.8 to -0.6 °C/month. Warming rate from vertical advection also increase to 1.0 °C/month during Stage III, associated with fall breakdown of stratification. In other words, the warming trend of the near-bottom NNYB region is mainly regulated by variations of vertical advection and the increase of the X-advection of heat.

Unlike NES and NNYB, the SNYB region has nearly the same, or slightly decreasing warming trends throughout the three stages (+0.9, +0.8, +0.8 °C/month). The warming effect from advection in the x-direction decreases throughout three stages (1.4, 0.6, 0.4 °C/month) and the cooling effect from Y-advection decreases as well (-2.9, -2.0, -2.3 °C/month). Similar to NNYB, the warming effect from vertical advection decreases from 1.7 to 1.3 °C/month from Stage I to II, but increase to 1.8 °C/month. Therefore, the net effect from the advection term turns from a weak warming rate at 0.2 °C/month (Stage I) to a weak cooling rate at -0.1 °C/month (Stage II and III).

2.5.3 Vertical Diffusion versus Advection

Figure 2.12 compares the relative contributions of vertical diffusion relative to each advective term. According to Lentz [2017], the warming of the Cold Pool is either due to vertical mixing - the vertical diffusion term in our Equation 3.2, or lateral mixing with the Slope Water - horizontal diffusion (residual) term in Equation 3.2. In our analysis, vertical mixing dominates the warming trends of the SNYB region, where the advection terms are balanced. The warming trend of the

near-bottom NNYB region is also dominated by vertical mixing (diffusion) during the first two stages. However, during Stage III, vertical advection is a significant factor in increasing the warming trend. For the NES region, vertical advection of heat dominates the increase of the warming trend, which is mainly associated with tidal mixing. Lateral mixing (horizontal diffusion) is nearly constant during the three stages and negligible for the NES and NNYB regions.

Therefore, on the seasonal time scale, an increase of vertical advection of heat from the upper layer in the NES region, associated with tidal mixing, warms its near-bottom layer as well as brings more advective heat in the along-shelf direction. An increase of the along-shelf advection does not increase the warming trend of the near-bottom NNYB region due to a decrease of vertical advection and an increase of across-shelf advection of heat. Thus, the NNYB region remains relatively cooler. Advection of this cooler water decreases the warming effect from along-shelf advection in the SNYB region, where warming trends become nearly constant and somewhat lower.

Thus, we confirm the importance of vertical advection of heat in the NES region and the down-stream advection of warm and the Cold Pool waters during the stratified seasons. Continuous and constant vertical mixing do influence the reduction of the Cold Pool volume and horizontal extent. However, it is vertical and horizontal advection that modulate the equatorward progression of the Cold Pool. The down-shelf advection of upstream warmed water from NS and southern flank of GB accelerates the northern extent retreat process. In contrast, at the southern extent of the Cold Pool, vertical mixing compensates horizontal advection, which slows its southern contraction, as we presented in Section 2.4.3.

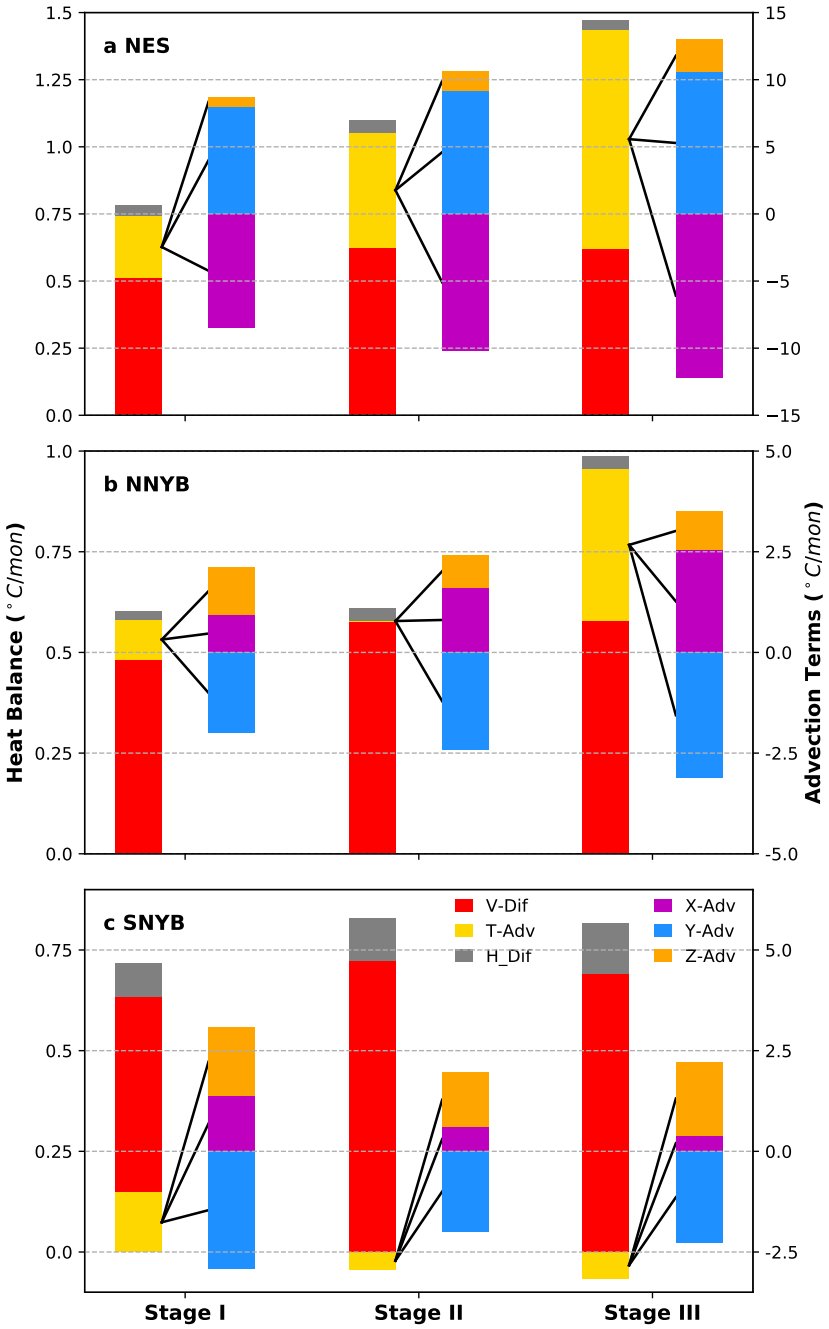

Figure 2.12: Bar plots of heat balances for the three near-bottom subdomains - (a) NES, (b) NNYB and (c) SNYB during three stages. The warming trends of the control volume are contributed by vertical diffusion (red), total advection (yellow) and the residuals (gray). The total advection are a sum of X-advection (purple), Y-advection (blue) and Z-advection (vertical advection, orange), with y-axis on the right hand side of each panel.

2.6 On the Possible Origins of the Cold Pool

We investigate the possible downstream path of the Cold Pool using the modeled fifty years of near-bottom temperature anomalies. Based on our previous analysis in Section 2.4, the Cold Pool cores travels along the 60-m isobath, from the south of the NS, to the HSV. We investigate further the path and origin of Cold Pool water before the onset of stratification. Both strong tidally-mixed winter water of the NS [Houghton et al., 1982] and upstream colder water sources (e.g. GB, GoM) [Hopkins and Garfield III, 1979, Han and Niedrauer, 1981, Fairbanks, 1982, Brown et al., 2015] have been suggested as possible sources.

In order to track the possible source water of the Cold Pool before the stratified seasons, we performed a lead-lag correlation analysis on the 50-year near-bottom (below 30 m depth) depth-averaged temperature anomalies T_a' (Figure 2.13). The lead-lag correlations are applied between near-bottom depth-averaged temperature anomalies T_a' of a grid point and those of the rest whole shelf region. The positions of the Cold Pool cores on calendar day 120 (during Stage I), calendar day 130 (during Stage I), calendar day 155 (during Stage II), calendar day 200 (during Stage III), and calendar day 255 (finally disappeared), are selected as base points in the lead-lag correlation analysis.

The near-bottom depth-averaged temperature anomalies T_a' are calculated as temperature anomalies both in time and horizontal space. First, the near-bottom depth-averaged temperature T_b is computed by averaging temperatures vertically from 30 m depth to the bottom. Second, to remove the seasonal signal (which could result in geographical phase difference), the 50-year climatological seasonal cycle (daily) of near bottom depth-averaged temperature $< T_b >$ is deducted for each horizontal point. Finally, the horizontal mean of temperature anomalies T_a over the shelf domain on each time step is deducted in order to discern the distinctive colder water mass. Equations computing the near-bottom

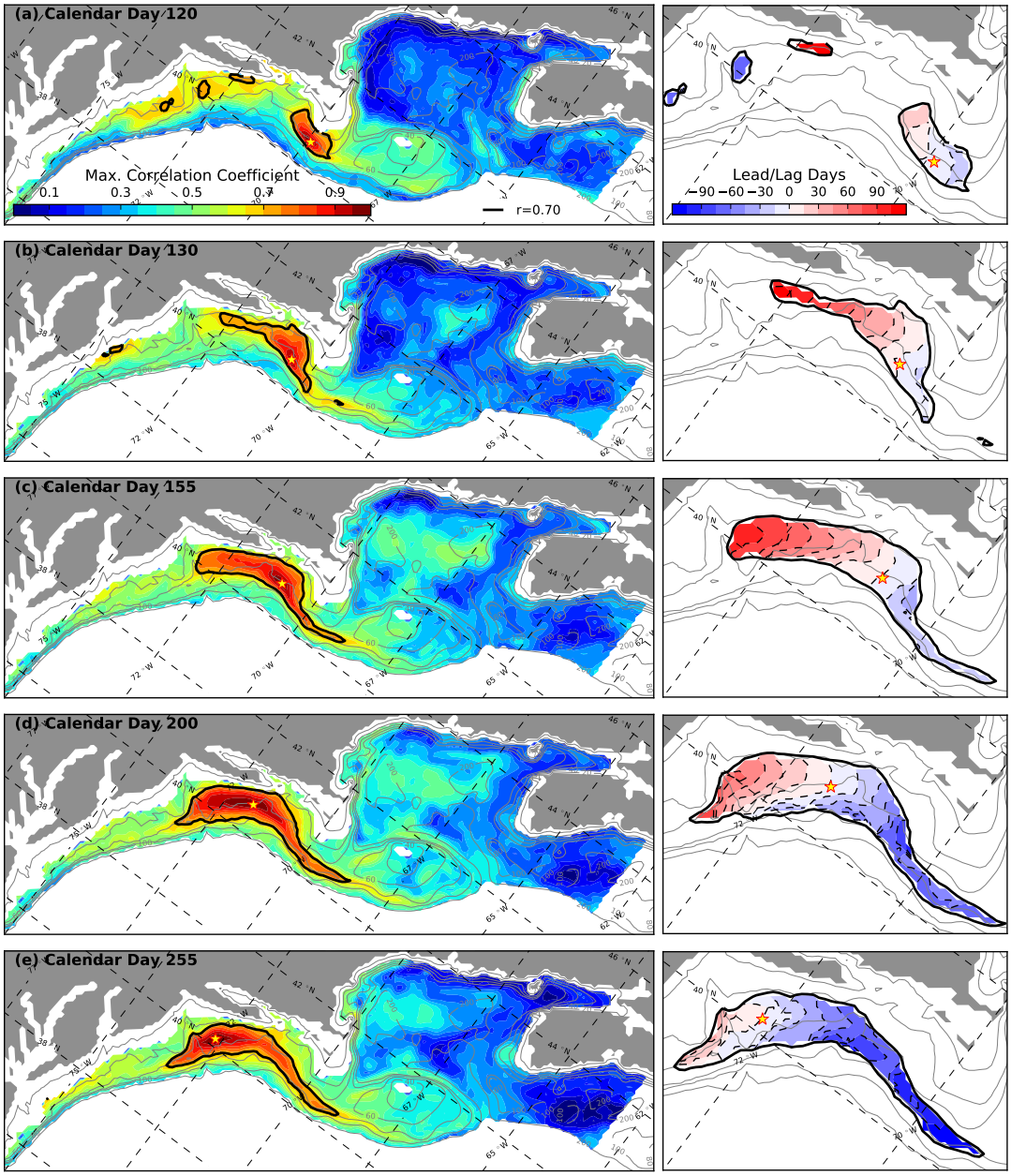

Figure 2.13: Lead-lag correlation analysis on the near-bottom (30 m depth to the bottom) depth-averaged temperature anomalies. Left panels: the maximum correlation coefficients irrespective of lead/lag days for the positions of the Cold Pool cores on (a) calendar day 120, (b) calendar day 130, (c) calendar day 155, (d) calendar day 200, and (e) calendar day 255. Right panels: the respective lead/lag days when reaching the maximum correlations on calendar days 120, 130, 155, 200 and 255. Correlations that do not reach 95% significance are masked. Positions of the base points are marked as yellow stars. The region with correlation coefficient larger than 0.7 is outlined by the black solid contours.

depth-averaged temperature anomalies T'_a are illustrated as follows:

$$T_a = T_b - < T_b > \tag{2.6}$$

$$T'_a = T_a - \overline{T_a} \tag{2.7}$$

where $< T_b >$ represents time average of 50-year seasonal near-bottom depth-averaged temperature T_b, $\overline{T_a}$ represents horizontal mean of temperature anomalies over the shelf domain.

The maximum correlation coefficients irrespective of lead/lag days highlight the spatial distribution of the Cold Pool water, without the limit of the 10 °C isotherm. The highest correlation regions (maximum correlation coefficient ≥ 0.7 irrespective of lead/lag days) on different calendar days denote the locations that are statistically probable Cold Pool water (Figure 2.13). The lead/lag days when maximum correlation obtained increases in the down-shelf direction, suggesting the possible downstream path of the Cold Pool water. On calendar day 120 (by the end of April), the Cold Pool is confined into an elliptical shape over the mid-shelf in the southeast of the NS (Figure 2.13a), which confirms the conclusion of Houghton et al. [1982] that the local tidally-mixed winter water is the main source water of the Cold Pool. Another high-correlation region is located at the near-shore of the New York Bight, shoreward of the 60-m isobath. However, they are not continuous in space and especially in lead/lag days when maximum correlation obtained. On calendar days 130 and 155, the maximum correlation regions move down-shelf and gradually expand in both up-shelf and down-shelf direction (Figure 2.13b and 2.13c). Down-shelf expansion of the maximum correlation region is along the mid-shelf (40 to 60 m isobaths), which is mainly due to advection of the Cold Pool water; while up-shelf expansion is along the 80-m isobath, which indicative of upstream advection from the southern flank of GB. On calendar days 200 and 255, the maximum correlation regions continue its down-shelf expansion over the mid-shelf (40 to 80 m isobaths) as a result of advection of the Cold Pool

water (Figure 2.13d and 2.13e).

Therefore, we conclude that the Cold Pool is not only originated from winter remnant water from the NS, but also has an upstream source traveling from the southern flank of GB along the 80-m isobath. The upstream source water continuously mixes with the local remnant winter water and forms the mixed Cold Pool water, which travels southwestward along the shelf between the 40 and 80 m isobaths.

2.7 Summary

The Cold Pool is a distinct cold and relatively fresh water mass, with a temperature lower than 10 °C and a salinity of less than 34 *psu*. It develops below a shallow seasonal thermocline and is located over the mid- and outer-shelf in the Mid-Atlantic region. Following this definition, we employed three criteria to capture and quantify the Cold Pool based a 50-year (1958-2007) high-resolution regional ocean model hindcast: (1) Temperature & Salinity Criteria, (2) Stratification Criterion, (3) Location Criterion. The model exhibits significant skill in capturing the Cold Pool characteristics including seasonal variability of both surface and subsurface temperatures in the MAB.

The Cold Pool is a continuous and persistent feature that experiences an *onset - peak - decline* cycle during its annual cycle. Typically it first emerges around early April, reaches maximum volume around mid-May and then gradually disappears around mid-September. Three stages of the Cold Pool event are defined according to its evolution and characteristics. The Cold Pool volume has a fast expansion during the first stage, mainly contributed from the south of NS, which is considered as the winter remnant source water of the Cold Pool [Houghton et al., 1982].

The depth-averaged and across-shelf fields of temperature and salinity highlight that the Cold Pool is not a horizontally well-mixed water mass during most of its duration. One of the prominent feature of the Cold Pool is that the Cold Pool cores move equatorward, with warming rates at about 0.1 °C/month during the three stages of its evolution. Following the temperature minima, we can track that the coldest water patch travels down the shelf along the 60-m isobath at a speed of 2-3 cm/s starting south of the NS to the HSV. The Cold Pool salinity minima, however, do not exhibit the same clear down-shelf traveling path as temperature. However, the salinity-minimum path that begins during Stage II indicates there may be an upstream input of source waters to the Cold Pool.

The northern extent of the Cold Pool retreats 2.6 times faster than the southern extent during Stage III. We suggest that horizontal advection plays an key role in setting the difference in northern and southern extent retreat speeds. When the upstream water from the southern flank of GB has enhanced warming and mixing, the down-shelf advection of upstream water acts to warm the northern edge of the Cold Pool; while in the southern edge of the Cold Pool, the down-stream advection exerts a cooling effect.

Spatial patterns of the near-bottom depth-averaged heat budget terms suggest that advection, rather than vertical diffusion, regulates the geographical difference in the warming rates during the three stages of the Cold Pool evolution. The continuous, and almost constant, vertical mixing does influence the shrinking of the Cold Pool volume and its horizontal extent. However, it is the vertical and horizontal advection that regulates the spatial warming rate and progression of the Cold Pool. The analysis of the heat balance within each near-bottom control volume confirms the importance of vertical advection of heat in the NES region and down-stream advection of warmed water in NNYB and Cold Pool water in SNYB during the stratified seasons.

In order to investigate the origins and path of the Cold Pool before the stratified seasons, we performed a lead-lag correlation analysis on the 50-year near-bottom temperature anomalies. This analysis suggests that the Cold Pool not only originates from winter remnant water from the NS, but also has an upstream source that travels from the southern flank of GB along the 80-m isobath. Further analysis (using either Lagrangian or passive tracers) to further track the sources of Cold Pool water is beyond the scope of this paper, which focuses on the seasonal variability.

This study is the first to examine the seasonal evolution of the Cold Pool using a long-term, high-resolution numerical model. The detailed model evaluation on the shelf serves as the foundation for further exploration of the interannual variability and long-term trends of the Cold Pool in this region. Further work is also warranted in order to explore the possible impacts of offshore contributions to the Cold Pool including the onshore motion of the shelf-break front, Slope Water and Gulf Stream warm-core ring intrusions, and the interaction between summer/fall storms and the breakdown of the Cold Pool.

2.8 Appendix

2.8.1 Inverse Distance Weighting Method

In the model evaluation process, the corresponding model values are interpolated using the Inverse Distance Weighting Method, where the weighted factor is chosen as the reciprocal of distance between the observation location and its nearby four model grid points:

$$T = \frac{\sum_{i=1}^{4} w_i t_i}{\sum_{i=1}^{4} w_i}; \; w_i = \frac{1}{D_i} \tag{2.8}$$

where w_i represents weighted factor of each of the four nearest grid values, D_i indicates horizontal distance between the observation location and each of the four nearest grid locations, t_j represents the corresponding temperature value of the four grid points, and T represents the interpolated model value at a specific depth.

2.8.2 Cross-shelf Hydrography Comparison

We compare model results with surface-to-bottom temperature and salinity vertical profiles along transects across the MAB during the years 2006 and 2007. The dataset is available on the THREDDS Data Server at Department of Marine and Coastal Sciences at Rutgers University (`http://tds.marine.rutgers.edu/thredds/catalog/cool/glider/mab/Gridded/old/catalog.html`). The model outputs are interpolated onto the same time and location as the observational data in both the vertical and horizontal directions, using the Inverse Distance Weighting method (Equation 2.8).

Here, we present comparisons of two cross-shore transects between AUGV profiles and model outputs, acquired when the Cold Pool was forming during the summer of 2006 and 2007 as shown in Figure 2.14 and 2.15. Figure 2.14 shows comparisons of temperature and salinity profiles achieved by the AUGV mission employed during June 14 to June 29, 2006 and those in the model, respectively. Figure 2.15 shows another set of comparisons of temperature and salinity profiles achieved by AUGV during July 18-29, 2007. Trajectories of both missions are plotted respectively in the left panels of Figure 2.14 and 2.15.

The model captures the overall structure and temporal variability of both temperature and salinity profiles during these two synoptic Cold Pool events. We note that (1) the near-bottom temperature in the model was biased higher by 1.21-2.24 °C compared to observed values, and (2) the thermocline in the model was shallower by 5-10 m compared to the observation. Importantly, the model

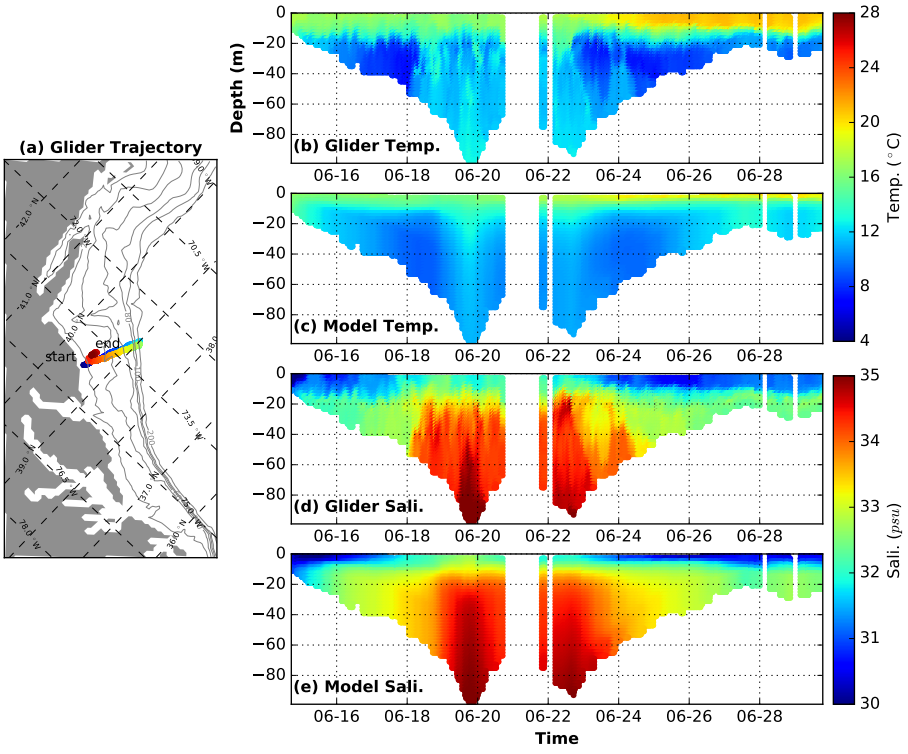

Figure 2.14: Comparisons of across-shelf temperature and salinity profiles between glider observation (one particular AUGV mission during June 14-29, 2006) and the correspondent model interpolated result. (a): trajectory of the glider mission, starting from nearshore region off southeast New Jersey traveling across-shelf to the shelf break region and then traveling back across-shelf to the inner-shelf region; Right four panels: Hovmöller diagrams of (b) Glider Temperature, (c) Model Temperature, (d) Glider Salinity, and (e) Model Salinity profiles with depth in the y-axis and time in the x-axis.

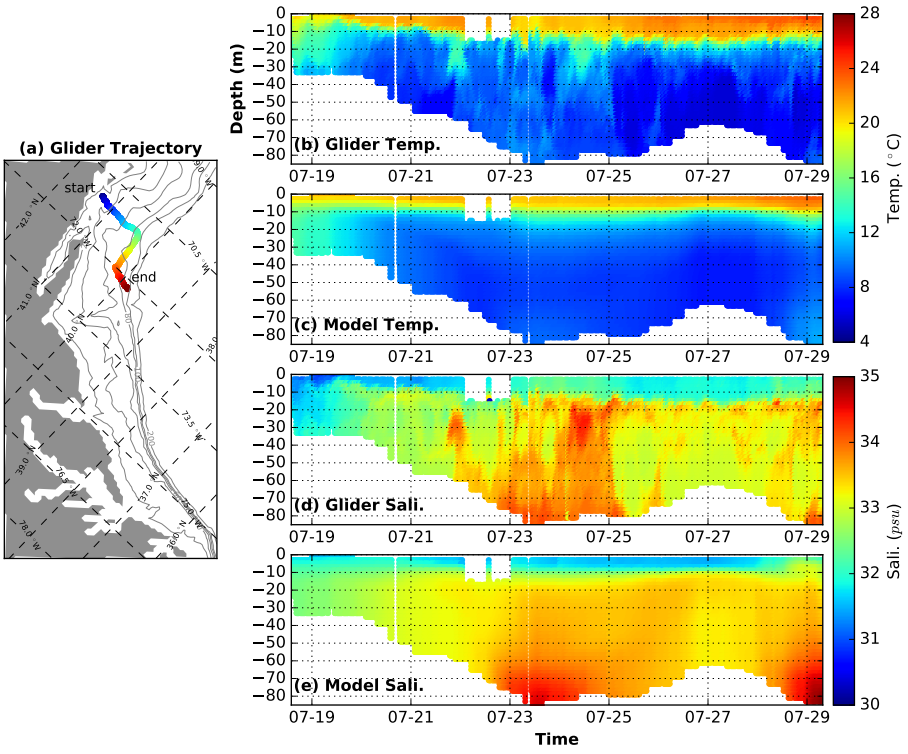

Figure 2.15: Same as Figure 2.14 but during July 18-29, 2007, with a zig-zag trajectory of glider mission, starting from nearshore region off Rhode Island traveling across-shelf to the shelf-break region and then traveling down-shelf and shoreward to the 60 m isobath region south off Long Island Sound and finally seaward to the shelf break.

does capture the relative cold and fresh subsurface water mass between the 20 and 70 m isobaths during the two synoptic Cold Pool events.

2.8.3 Comparison of a Cross-shelf Temperature Transect and Bottom Temperature during 1979

Monthly-averaged temperature transects along the Nantucket Shoals Flux Experiment (NSFE79) array are compared between the model solutions and observation results of Houghton et al. [1982] from April to September of the year 1979 (Figure 2.16). The transect along the NSFE79 array is nearly in the across-shelf direction, perpendicular to the local isobaths. Longitudes and latitudes of the six mooring stations along the NSFE79 array are obtained from Beardsley et al. [1985], for model interpolation. During April, the near-shore region (shallower than 100-m depth) is cold (below 6 °C) and well-mixed, with the temperature gradient increasing in the offshore direction. The isotherms begin tilting toward the shelf in the surface layer with the enhancement of surface heating. The distinct cold water mass has been formed in May, capped by warmer surface water and also isolated by the warmer near-shore and shelf-break waters. The Cold Pool begins shrinking in volume and increasing in temperature during the summer months (June, July, August and September). Month-by-month comparisons of temperature cross-sections along the NSFE79 array, shows the model is capable of capturing the seasonal variability of the thermal feature during the Cold Pool event of 1979.

We further compared the distribution of the MAB BT between the model and observations from Houghton et al. [1982] for the year 1979 (Figure 2.17). The observed distribution of BT were based on six hydrographic surveys conducted by the NEFSC over the MAB continental shelf in 1979, which is part of the Marine Resources Monitoring Assessment and Prediction (MARMAP) program

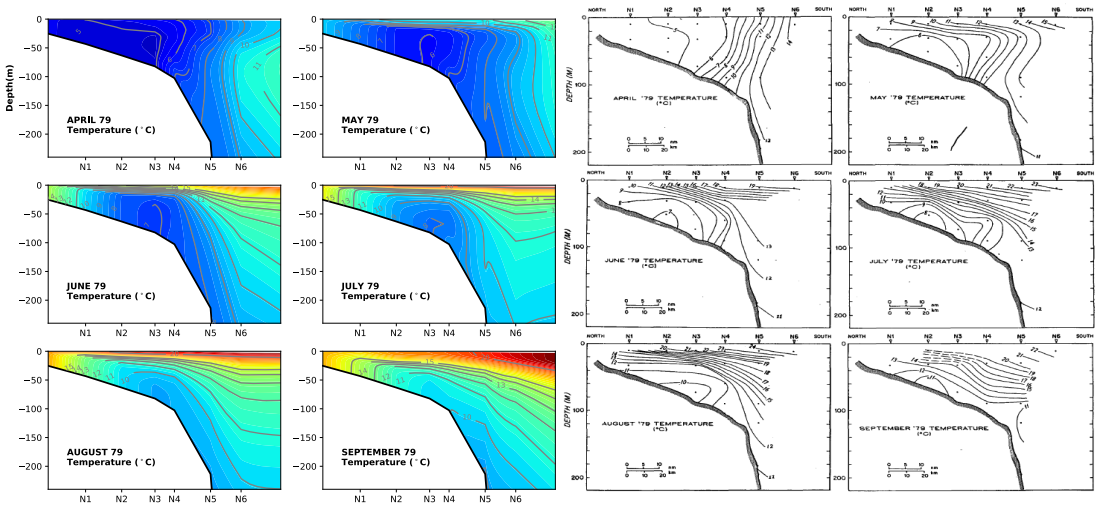

Figure 2.16: Comparisons of monthly-averaged temperature transects along the NSFE79 array between the model (left) and observation (right).

[Houghton et al., 1982]. In the early spring (February 23 - March 15), BT of the MAB continental shelf is colder in the nearshore region and reaches its coldest value (below 2 °C) near the NS. Due to enhanced surface heating and mixing, BT in the NS increases quickly and shuts down the connection of the coldest water patch with the nearshore region. The coldest BT in May is located in the mid-shelf between the 60- and 80-m isobaths, and travels equatorward along the shelf. During following months (June, July and August), the cold water patch continues moving southwestward along the shelf, with an increasing temperature. By the end of the summer (September 3 - October 29), the coldest BT is located near the HSV. Although the distribution of BT in the model is not exactly the same as that of the observed BT, for example there is no secondary cold patch during the summer seasons (June - October), and the BT has a warm bias of 1-2 °C, the model does capture the spatio-temporal variation of the coldest water patch traveling equatorward from the NS to the HSV.

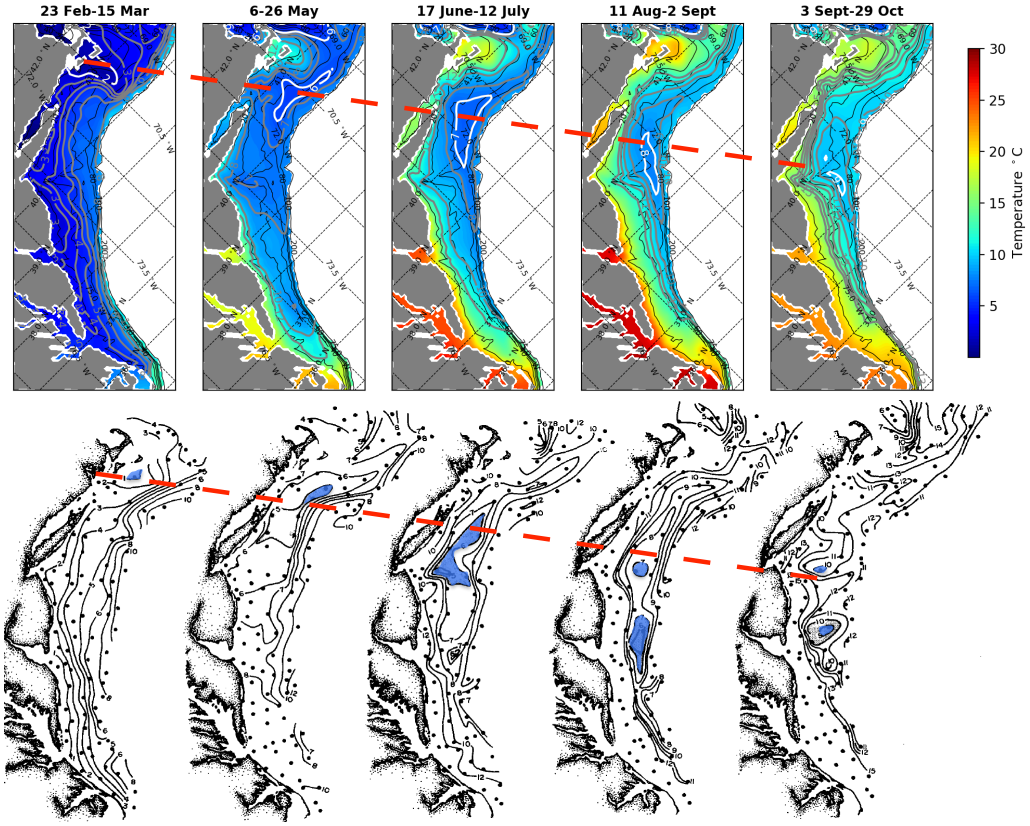

Figure 2.17: Comparisons of bottom temperature distributions between the model (upper panels) and observations (lower panels) from the MARMAP program during the year 1979. The isotherms of 2, 6, 7, 8, 9 °C in the model BT horizontal distribution is plotted in white contours. The minimum temperature of the coldest water patch in the observation is covered in blue. Two red dashed lines represent the equatorward progression of the minimum temperature in the model and observations, which are parallel to each other.

2.8.4 Temperature Criterion Selection

The Cold Pool Quantification method in Section 3.3.3 uses 10 °C as the threshold value for Temperature Criterion. We test the robustness of our results by changing the temperature criterion from 10 °C to 11 °C and 12 °C, the Cold Pool's total volume, average temperature, average salinity, and average thickness are then computed and compared for 50-year climatology (Figure 2.18). Results shows that the Cold Pool goes through the same *onset* - *peak* - *decline* cycle under 11 °C or 12 °C. The Cold Pool emerges at the same time (calendar day 95), but peaks in total volume at calendar day 139, 140 and 148, and ends at calendar day 256, 284 and 302, respectively under the 10, 11 and 12 °C. Similarly, the transition day when the Cold Pool shifts from Stage II to Stage III is postponed (calendar day 179, 205 and 231) as the threshold value for Temperature Criterion increases.

The Temperature Criterion is not the key factor affecting quantification of the Cold Pool during the early spring, as the MAB is still cold and fresh and development of stratification is just beginning at this time. Total volumes, average temperatures, average salinities, and average thickness of the Cold Pool are exact the same during the first 21 days of Stage I for the three cases. During Stages II and III, the Cold Pool warming rate increases (0.57, 0.60, and 0.61 °C/month during Stage II; 0.40, 0.48, and 0.62 °C/month) as the threshold values of Temperature Criterion increase. The Cold Pool salting rate does not have an obvious effect from the increasing Temperature Criterion, except the maximum average salinities have a slight increase from 33.35 to 33.37 and 33.42 *psu*. In general, the higher the Temperature Criterion, the larger the Cold Pool's volume and the longer the Cold Pool exists. The maximum total volume of the Cold Pool increases by 8.7% and 14.4% as the Temperature Criterion increases from 10 °C to 11 °C and 12 °C. Though it is possible to de-bias the model results,

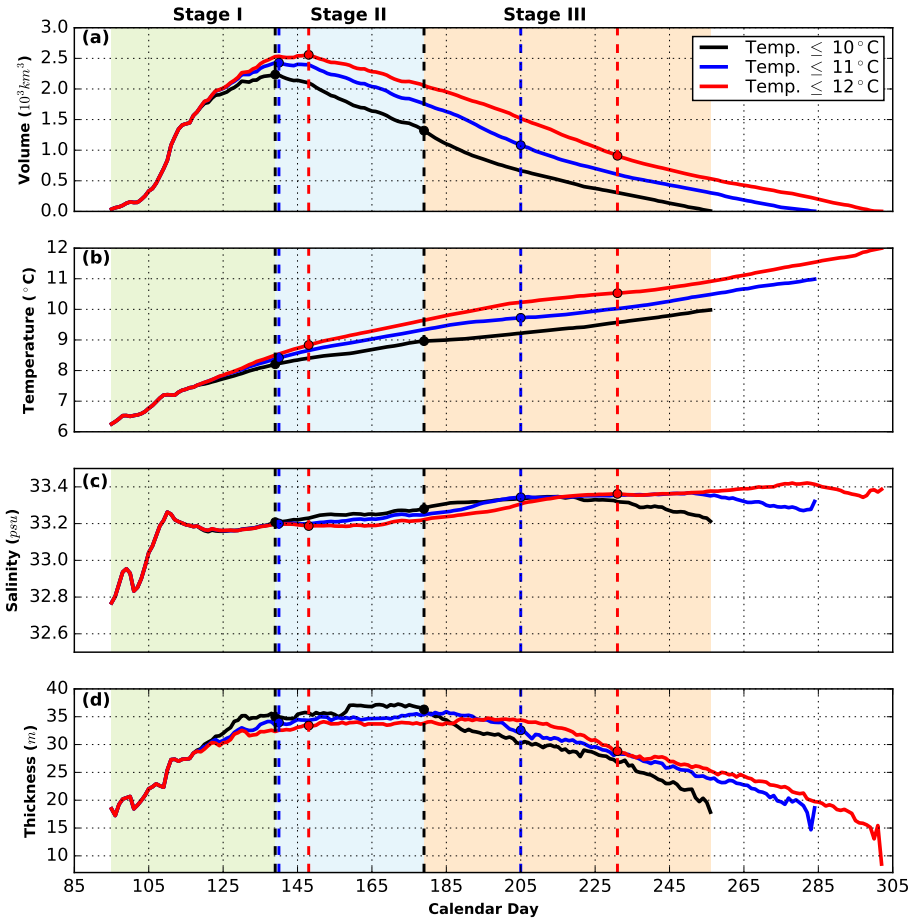

Figure 2.18: Comparisons of (a) total Cold Pool volume, (b) average Cold Pool temperature, (c) average Cold Pool salinity, and (d) average Cold Pool thickness under three different Temperature Criteria - 10 °C (black), 11 °C (blue), and 12 °C (red). The three stages under each criteria are separated by dashed lines in their respective colors. The three stages for the Temperature Criterion $\leq$ 10 °C are also denoted in same three colors in the background as in Figure 2.5 and 2.7.

given the temporally and spatially sparse observations, we chose to work with the dynamically consistent model results without modification.

Chapter 3

Inter-annual Variability of the Mid-Atlantic Bight Cold Pool

3.1 abstract

The Mid-Atlantic Bight (MAB) Cold Pool is a bottom-trapped cold (lower than 10 °C) and fresh (lower than 34 psu) water mass, that is isolated from the surface by the seasonal thermocline, and is located over the mid- and outer-shelf of the MAB. The interannual variability of the Cold Pool is investigated based on a long-term (1958-2008) high-resolution regional model of the Northwest Atlantic Ocean. Results show that the Cold Pool exhibits significant year-to-year variability in persistence time, volume and temperature. Based on the persistence time, volume and volume-averaged temperature, a Cold Pool Index (CPI) is defined and computed in order to represent the strength of the Cold Pool. Anomalous strong and weak years are investigated using a composite analysis based on the CPI. The equatorward progression and horizontal distribution in temperature and salinity of the Cold Pool during summer are compared between strong and weak Cold Pool years. A detailed quantitative study of the volume-averaged heat budget of the Cold Pool region between strong and weak Cold Pool years suggests that abnormal warming/cooling from initial temperature and horizontal advection drives the interannual variability in temperature. The depth-averaged temperature anomaly in the Cold Pool region is largely determined by the initial temperature anomaly in the early spring, suggesting a potential for seasonal predictability.

3.2 Introduction

The Mid-Atlantic Bight (MAB) is one of the most ecologically- and economically-important habitats of the northeast U.S. shelf. Over the past few decades, the MAB shelf warming has been documented not only in the surface layer [Friedland and Hare, 2007, Fulweiler et al., 2015, Shearman and Lentz, 2010], but also in near-bottom waters [Forsyth et al., 2015, Kavanaugh et al., 2017]. Ocean warming has been associated with declines of abundances and poleward shifts of distribution of cold-water species over the U.S. northeast continental shelf [Gawarkiewicz et al., 2014, Nye et al., 2009, 2011]. As a seasonally prominent thermal feature, the Cold Pool exerts a strong influence on the recruitment and settlement of several cold-temperatures fish species in the MAB ecosystem [Miller et al., 2016, Sullivan et al., 2005], as well as phytoplankton and zooplankton productivity [Flagg et al., 1994, Bi et al., 2014].

The Cold Pool is a bottom-trapped cold and fresh (usually below 10 °C and 34 psu) water mass isolated from the surface by a seasonal thermocline, located over the mid- and outer-shelf of the MAB. The spatial and seasonal variability of the Cold Pool has been investigated by using both observations and models [Houghton et al., 1982, Lentz, 2017, Chen et al., 2018a]. It is a continuous and non-stationary feature that experiences an annual cycle of *onset - peak - decline*. It first emerges around early April, reaches maximum volume around mid-May and then gradually disappears around mid-September. The core of the Cold Pool has been recorded to travel along the 60-m isobath at a speed of 2-3 cm/s on a 50-year average, from south of the New England shelf to the Hudson Shelf Valley [Chen et al., 2018a].

Differing theories were proposed about the origins of the Cold Pool. Fundamentally, there are two possible origins of the Cold Pool, which can be classified

as local- and remote-origins. The remnant winter water over the MAB continental shelf is considered the local source. Past work suggests that the Cold Pool forms with strong winter mixing and becomes isolated from the surface due to the onset of summer stratification in the water column, with no renewal from upstream sources [Bigelow and Sears, 1933, Ketchum and Corwin, 1964, Houghton et al., 1982, Ou and Houghton, 1982]. The upstream cold water sources, such as cold waters from the Gulf of Maine (GoM) and Georges Bank (GB) are considered as remote source of the Cold Pool [Hopkins and Garfield III, 1979, Han and Niedrauer, 1981, Fairbanks, 1982, Brown et al., 2015]. Based on a lead-lag correlation analysis on the near-bottom temperature anomalies of the MAB and GB, Chen et al. [2018a] suggests that the Cold Pool not only originates from winter remnant water over Nantucket Shoals, but also has an upstream source traveling from the southern flank of GB along the 80-m isobath during the spring.

Due to limited observations for long periods, the inter-annual characteristics and long-term variability of the Cold Pool are still widely unknown. In this study, we investigate the inter-annual variability based on a 50-year (1958-2007) high-resolution model of the Northwest Atlantic Ocean [Kang and Curchitser, 2013, 2015, 2017]. Strong and weak Cold Pool years are differentiated and investigated according to a derived Cold Pool Index, which represents the strength of the specific event.

This paper is organized as follows. In Section 4.3, we introduce the high-resolution model, model evaluation and the Cold Pool quantification methods. Section 3.4 presents the interannual variability of the Cold Pool variables and the summer evolution between strong and weak Cold Pool years. In Section 3.5, heat budgets of the Cold Pool region of both strong and weak Cold Pool years are investigated. Finally, we will summarize the results in Section 3.6.

3.3 Method

3.3.1 ROMS-NWA Model

The long-term (1958-2007) high-resolution numerical simulation of the Northwest Atlantic Ocean was performed with ROMS, a split-explicit, free-surface, terrain-following, hydrostatic, primitive equation [Shchepetkin and McWilliams, 2005]. The model domain extends from the Gulf of Mexico to the Gulf of St. Lawerence as shown in the background of Figure 3.1. Horizontal resolution is about 7 km on average. In the vertical, there are 40 terrain-following levels, with water depth varying from 10 m to 5500 m. The model employs K-Profile Parameterization scheme for vertical mixing in the boundary layer and ocean interior [Large et al., 1994]. The model's initial and oceanic boundary forcing are derived from the re-analysis data of Simple Ocean Data Assimilation version 2.1.6 [Carton and Giese, 2008]. The Coordinated Ocean-ice Reference Experiments (CORE.v2; 1948-2007) data sets provide atmospheric forcing, which includes air temperature, sea level pressure, humidity, wind, solar radiation, and precipitation. The model implements riverine freshwater flux input from the global river discharges runoff of Dai et al. [2009]. Ten major tidal components, which was extracted from TPXO dataset,are used to simulate tides [Egbert and Erofeeva, 2002]. Standard circulation state variables, for example, temperature, salinity, and currents, are archived at a daily interval.

The ROMS-NWA model has been used to study eddy characteristics and energetics and impacts of mesoscale eddies on the vertical nitrate flux in the Gulf Stream region [Kang and Curchitser, 2013, 2015, 2017, Kang et al., 2016, Zhang et al., 2018a], and seasonal variability of the Cold Pool over the Northeast US continental shelf [Chen et al., 2018a]. Our study also focuses on the MAB and GB shelf regions with depth between 20 m and 200 m, as indicated in the red box in

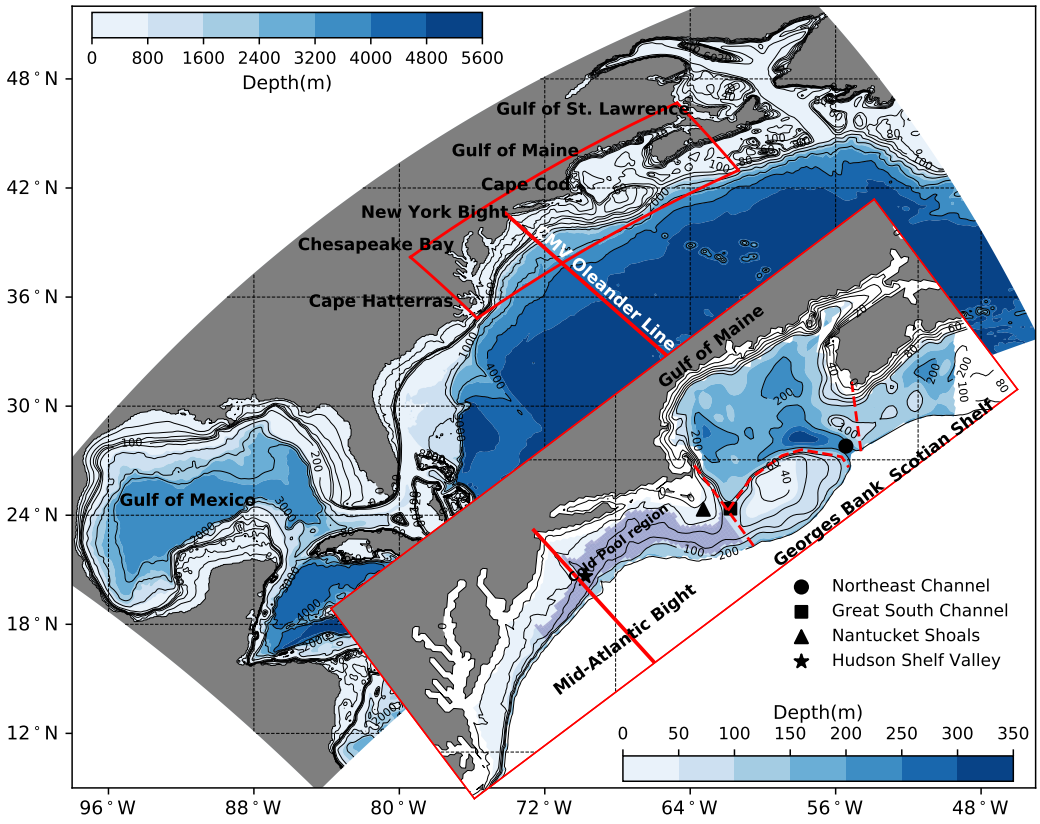

Figure 3.1: Bathymetry of the NWA-ROMS model domain (in the background; colorbar: upper left) and the study area (zoomed red box; colobar: lower right). Contours of the model domain are given every 20 meters from 0 to 100 m, every 100 meters from 100 to 200 m, and every 1000 meters from 1000 to 5000 m. Contours of the zoomed study area are given every 20 meters from 0 to 100m and every 100 meters from 100 to 200m. Red dashed lines denote boundaries between four sub-domains of the study area: Middle Atlantic Bight, Georges Bank, Gulf of Maine, and Scotian Shelf with depth between 20 and 200 m. The CMV Oleander Line is represented by the red solid line. Special topography, such as Hudson Shelf Valley, Nantucket Shoals, Great South Channel, and Northeast Channel are marked with different markers (shown in the lower right legend) in the zoomed red box. The Cold Pool region is plotted in purple.

Figure 3.1. Previous work carried out extended model evaluation over the MAB continental shelf, including a comparison with trawl survey datasets calibrated from the Northeast Fishers Science Center (NEFSC) and cross-shelf glider observations from the Center for Ocean Observing Leadership at Rutgers University, described in Chen et al. [2018a]. We further perform model evaluation using the vessel *CMV Oleander* expendable bathythermograph (XBT) dataset presented in Section 3.3.2. Another comparison of bottom temperature and monthly-averaged temperature transects in one particular year 1979 are performed between model and observation results in Houghton et al. [1982].

3.3.2 Model Evaluation

Model evaluation on the seasonal time scale has been included in Chen et al. [2018a]. Here we perform model evaluation of temperature on the interannual time scale, using two long-term observational datasets: (1) Northeast Fisheries Science Center (NEFSC) Trawl Survey datasets(1963-2007; `comet.nefsc.noaa.gov/cgi-bin/ioos/ioos.pl`); (2) the vessel *CMV Oleander* XBT datasets (1977-2007; `po.msrc.sunysb.edu/Oleander/XBT/NOAA_XBT.html`).

The NEFSC trawl surveys provide long-term records of both sea surface temperature (SST) and bottom temperature (BT) that located within the MAB region. The model and observation datasets are separated into summer-stratified (April to October) and winter-mixed (November to March) months for each year. Here we focus on the summer-stratified (Cold Pool-existing) months of each year and explore its comparison with model result on the interannual time scale. Corresponding model values are calculated using the Inverse Distance Weighting Method, same and as described in detail in Chen et al. [2018a]. Results show that the model is not only capable in capturing seasonal variability, but also the interannual variability of temperature over the MAB shelf (Figure 3.2). Although the model has a warm bias of 1.71 °C in summer bottom temperature over the

whole time series, the bias keeps relatively consistent with a correlation coefficient reaching 0.83. For the SST, the warm bias decreases to 0.43 °C and the correlation coefficient is about 0.99.

The vessel *CMV Oleander* XBT dataset provides temperature transects through the Northwest Atlantic regions including the continental shelf and slope, the Slope Sea, the Gulf Stream and the northwestern Sargasso Sea (Figure 3.1). Here we only focus on this long-term temperature structures on the MAB shelf (between 20- and 200-m isobaths). Comparisons of vertical temperature profiles on the shelf has been included in Figure 3a and 3b of Chen et al. [2018a]. For comparisons over the same summer-stratified (April-October) months on the interannual time scale, the model and observational datasets are vertically separated into a near-surface layer and a near-bottom layer at 30 m depth. Generally, the model overestimates the temperature in both near-surface and the near-bottom layers. By averaging observational values within each year, yearly-binned near-surface and near-bottom temperatures between model and observation suggest that the model has consistent warm bias with observation over the summer-stratified months. The bias is about 0.72 °C in the near-surface layer and about 1.02 °C in the near-bottom layer. The correlation coefficients between yearly-binned model and observation temperatures are 0.96 for both the near-surface and near-bottom layers. The RMSEs of near-surface and near-bottom temperatures between model and observation are 0.75 °C and 1.05 °C, respectively. In general, model performance in both near-surface and near-bottom temperatures shows significant agreement with observational values over the long-term time series.

3.3.3 Quantification of the Cold Pool and the Cold Pool Index

Chen et al. [2018a] define the Cold Pool as a relatively cold (below 10 °C) and

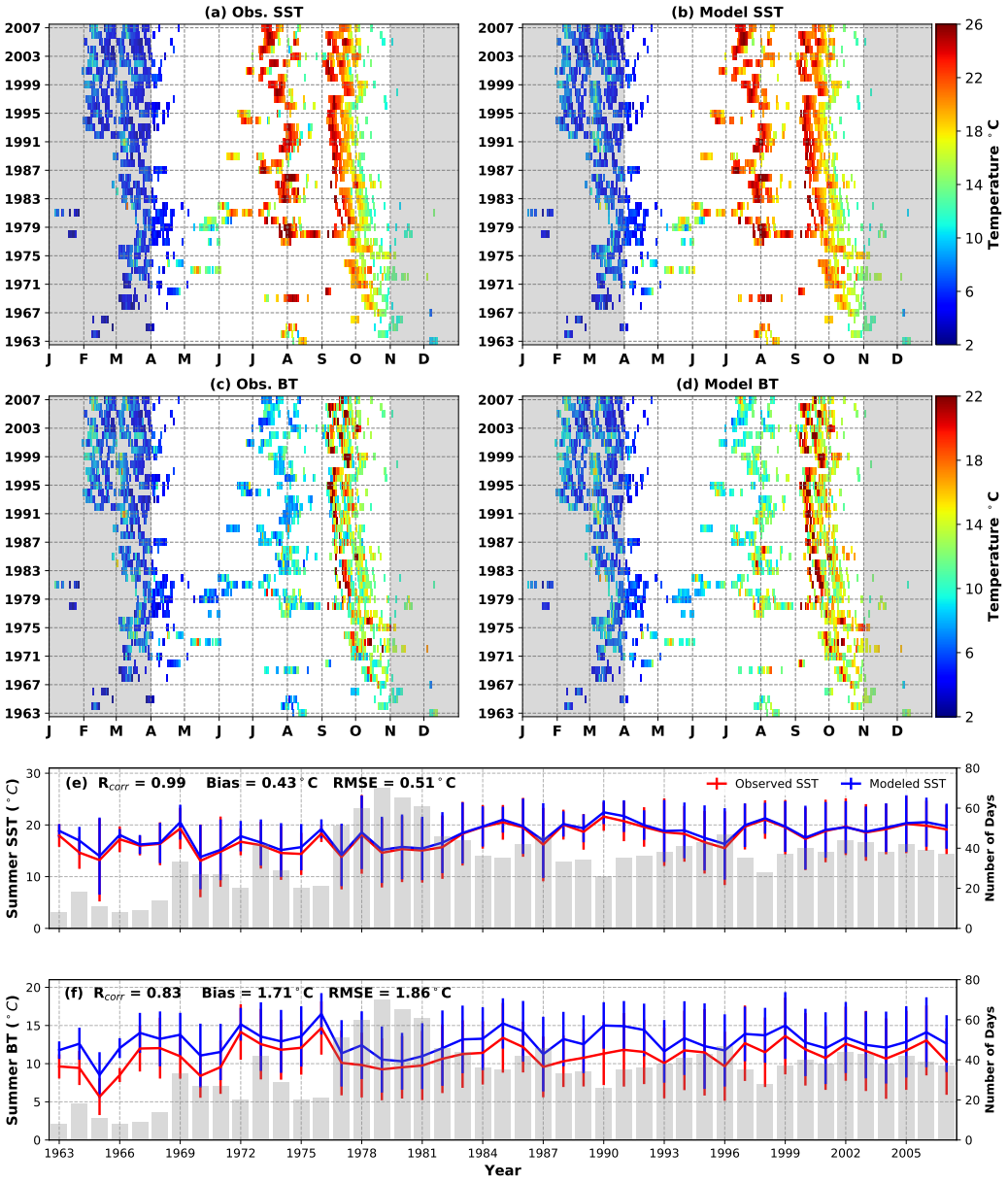

Figure 3.2: Observed sea surface temperature (SST) from NEFSC trawl surveys (a) vs. interpolated model values (b) with x-axis representing days within a year and y-axis representing year from 1963 to 2007. Data points that collected within summer-stratified months (April-October; with white background) are used for computation of yearly-binned values, as shown in (e) and (f). Panel (c) and (d) are the same as (a) and (b), but for observed bottom temperature (BT) vs. model values. Panel (e) and (f) shows comparisons of yearly-binned SST and BT between observation (red) and model (blue) during summer-stratified months. The gray bars in the background represent number of observational days within each year. Error bars of each line in (e) and (f) show plus/minus one standard deviation of each variable.

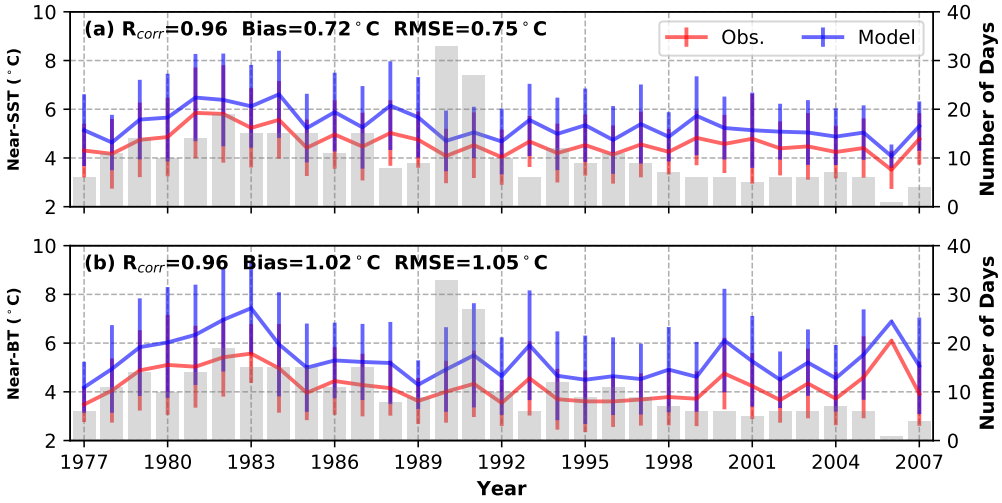

Figure 3.3: Comparisons of yearly-binned near-surface (a) and near-bottom (b) temperatures between observation (red) from Oleander XBT datasets and ROMS-NWA model (blue). The gray bars in the background represent number of observational days within each year. Error bars of each line show plus/minus one standard deviation of each variable.

fresh (below 34 psu) water mass located over the mid- and outer-shelf of the MAB, below the seasonal thermocline. Following this definition, they put forth three corresponding criteria to represent and quantify the Cold Pool. (1) Temperature & Salinity Criteria: temperature of the Cold Pool is lower than 10 °C; salinity is defined to be less than 34 *psu*, in order to separate the Cold Pool from the Slope Water [Mountain, 2003]; (2) Stratification Criterion: the Cold Pool develops along with the onset of thermal stratification, which is determined by calculating the mixed layer depth (MLD); (3) Location Criterion: the Cold Pool remains below the MLD, between the 20 and 200 m isobaths, with no direct contact with the air-sea interface. According to the Cold Pool's persistence time, volume magnitude, and volume-averaged temperature, we compute a Cold Pool Index (CPI) in order to evaluate the strengths of the Cold Pool during the 50 years of simulation. We define the CPI as the time-integrated Cold Pool volume multiplying by the difference between 10 °C and Cold Pool temperature for each year, and then

standardize it by the respective climatological value:

$$CPI = \frac{\int V \cdot (10 - T)\ dt - \int V_c \cdot (10 - T_c)\ dt}{\int V_c \cdot (10 - T_c)\ dt} \tag{3.1}$$

where V and T represent the Cold Pool total volume and volume-averaged temperature during each year, V_c and T_c represent the respective 50-year climatological values, and 10 °C is the threshold value for the Temperature Criterion of the Cold Pool definition.

By applying these three criteria, we can quantify the interannual variability of the Cold Pool and variations in its volume, temperature, salinity, density and progression velocity. In this study, we perform a Composite Analysis on the interannual variability of the Cold Pool based on the CPI for the 50 years (1958-2007). Those years whose CPI are above one standard deviation (STD) of 50-year CPI are regarded as strong Cold Pool years; while those below one STD are considered as weak Cold Pool years. The other years that are within one-standard deviation are considered as normal years. Correlations between the time series of the CPI and state variables are presented in Section 3.4.

3.4 Interannual Variability of the Cold Pool

In this section, we examine the interannual variability of the MAB Cold Pool with respect to its total volume, volume-averaged density, temperature, and salinity based on the Cold Pool quantification method (Figure 3.4). The Cold Pool characteristics during strong and weak Cold Pool years are then compared using the Composite Analysis.

3.4.1 Persistence of the Cold Pool

The persistence of Cold Pool events (length of time that the feature exists) varies interannually during the fifty years (1958 - 2007; Figure 3.4). The duration of the

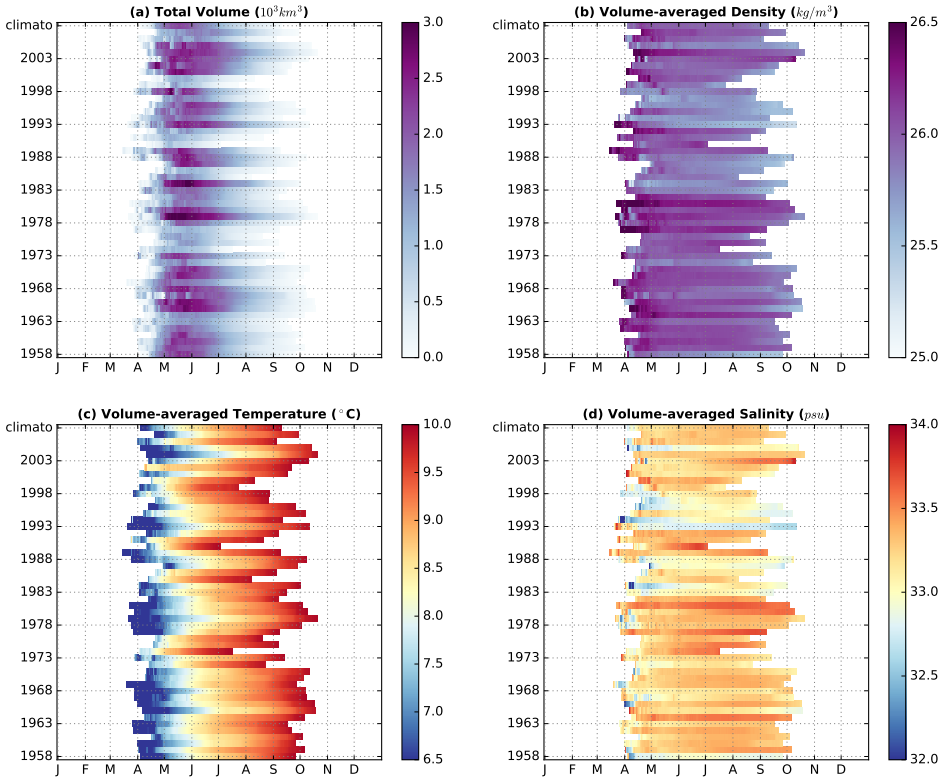

Figure 3.4: Inter-annual variations of the Cold Pool with respective to its (a) total volume(10^3 km^3), (b) mean thickness (m), (c) volume-averaged salinity (psu), and (d) volume-averaged temperature (°C) within the MAB region from 1958 to 2007. The y-axis of each panel of Figure 3.4 represents year from 1958 to 2007 and the climatological year on top of the year 2007. While the x-axis represents days from calendar day 1 to calendar day 366 for each year.

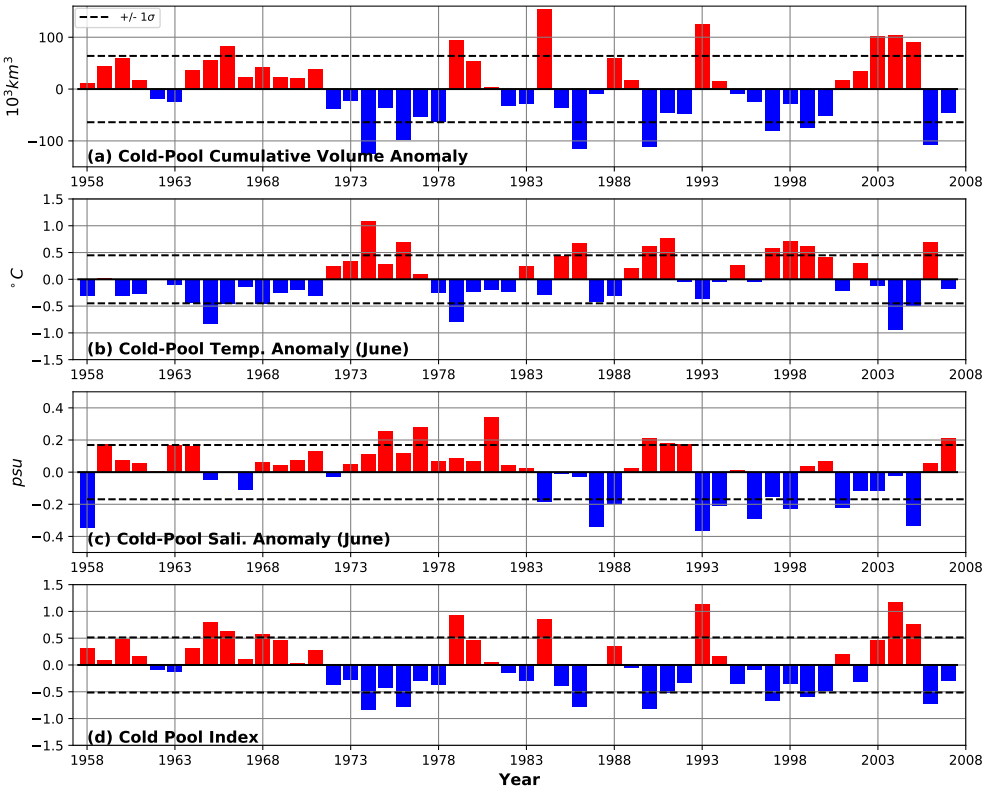

Figure 3.5: Inter-annual variations of the Cold Pool with respective to its (a) total volume anomaly (10^3 km^3), (b) average temperature anomalies for June (m), (c) average salinity anomaly for June (psu) from 1958 to 2007.

Cold Pool is 167±29 days on average, with a range from 85 days (year 1990) to 214 days (year 1979). The average starting day of the Cold Pool is on Calendar Day 95±10, ranging from Calendar Day 74 (year 1989) to Calendar Day 119 (year 1987). The average peak day is on Calendar Day 140±9, ranging from Calendar Day 112 (year 2002) to Calendar Day 158 (year 1964). However, the average end day of the Cold Pool is on Calendar Day 262±25, which has the largest interannual variation, ranging from Calendar Day 186 (year 1990) to Calendar Day 295 (year 1979, 2004). Therefore, persistence length of the Cold Pool mainly depends on when the Cold Pool ends.

3.4.2 Cold Pool Volume

The Cold Pool volume also exhibits strong year-to-year variability. Its peak volume shows large differences from year to year (Figure 3.4 a). For the years 1984 and 1979, the peak values of the Cold Pool's total volume could reach 3.2×10^3 km^3. While for the year 1990, the peak value is one third of that number (1.15×10^3 km^3). It suggests that the larger peak value of the Cold Pool volume, the longer the persistence time. The correlation coefficient between peak volume and persistence length of the Cold Pool is 0.69, with significance level nearly equal to 1. However, the Cold Pool peak volume does not have significant correlations with minimum temperature ($r = -0.29$) and mean temperature ($r = -0.45$) that it reached during each year. Compared with the Cold Pool peak volume, the cumulative Cold Pool volume has a relatively higher correlation with the minimum ($r = -0.43$) and mean ($r = -0.61$) temperatures during the 50 years.

3.4.3 Cold Pool Temperature

Volume-averaged Cold Pool temperature shows a significant seasonal and interannual variability from year 1958 to 2007 (Figure 3.4 c). For the years 1969 and

1977, minimum temperature of the Cold Pool reached 4.01 and 4.21 °C. However for the year 2002, the Cold Pool minimum temperature reached 8.32°C. The colder (warmer) minimum temperature of the Cold Pool does not suggest it has a large (small) cumulative volume. The cumulative Cold Pool volume anomaly is about zero during the year 1969 and is below one standard deviation during 1977; however, it is above one standard deviation during 2002 (Figure 3.5 a). In contrast, the cumulative Cold Pool volume anomaly is highly correlated with average Cold Pool temperature anomalies in May and June, with correlation coefficients equal to -0.71 and -0.82, respectively. Except for the year 2002, those years with above-one STD cumulative Cold Pool volume anomalies are always accompanied by negative temperature anomalies in June (Figure 3.5 b).

3.4.4 Cold Pool Salinity & Density

Unlike total volume and volume-averaged temperature, volume-averaged Cold Pool salinity and density have little seasonal variation. Except for year 1984, 1987, 1997, and 2003, the volume-averaged Cold Pool salinity variations for the other years are less than 0.6 psu from the start of April. For seasonal variation in Cold Pool density, only five years (1965, 1983, 1987, 1993 and 1995) have variations of more than 0.6 kg/m^3. Similarly, interannual variability of the Cold Pool salinity and density are not highly correlated with those of volume and temperature (Figure 3.5). The Cold Pool density and salinity have significant interannual variability, but they do not have strong correlations with the total volume and temperature. The correlations between cumulative Cold Pool volume and volume-averaged salinity in May ($r = -0.38$) and June ($r = -0.46$) are much less significant when compared to that with volume-averaged temperature. The correlations between cumulative Cold Pool volume and density in May and June are about zero.

3.4.5 Composite Analysis of Strong and Weak Cold Pool Years

We perform a Composite Analysis to investigate the Cold Pool characteristics during strong Cold Pool years (1960, 1965, 1966, 1968, 1979, 1980, 1984, 1993, 2004, and 2005) and weak Cold Pool years (1974, 1975, 1976, 1986, 1990, 1991, 1999, and 2000) based on the CPI values (Figure 3.6). The Cold Pool events initiate at nearly the same time during strong and weak Cold Pool years, but the average persistence period is about 6.5 months (196 days) for strong years and about 4 months (121 days) for weak years (Figure 3.6 a). The average maximum volume for strong years is about 2.8 $\times 10^3$ km^3, twice of that for weak years.

In order to explore the spatio-temporal variations of the Cold Pool between strong and weak years, we plot the Hovmöller diagrams of volume, minimum temperature and minimum salinity with the y-axis representing along-shelf distance and x-axis representing calendar days. We find the largest difference in Cold Pool volume is located mainly between the Nantucket Shoals (location A) and the Montauk Point (location B) in the along-shelf direction. The minimum temperature of the Cold Pool is about 2 °C colder during the Stages II and III of strong years than that of weak years. However, the warming rate of the Cold Pool is consistent (0.03 °C/day) during strong and weak years. The average traveling path for the Cold Core (location of minimum temperature) initiates from south of the Nantucket Shoals for both strong and weak years. However, the Cold Core disappears in the Hudson Shelf Valley (location C) during strong years and off Montauk Point (location B) during weak years.

In general, the weak Cold Pool years not only have lower volumes and temperatures, but higher salinities (Figure 3.6 c), although the correlation between the CPI and Cold Pool salinity anomalies in June are relatively low ($r = -0.39$) for

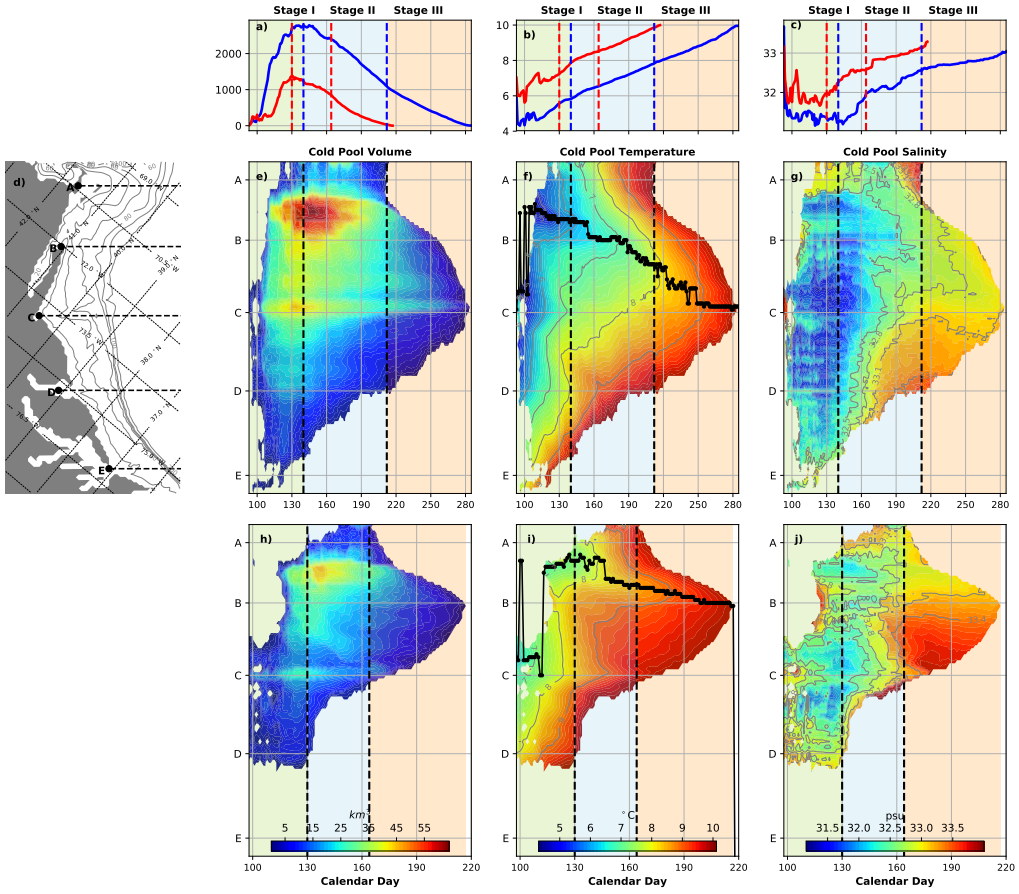

Figure 3.6: Hovmöller diagrams of e) & h) the Cold-Pool volume (km^3), f) & i) the Cold-Pool minimum temperature (°C), and g) & j) the Cold-Pool minimum salinity (psu) during the average strong and weak Cold Pool years; and their respective one-dimensional time series in the upper three panels - a), b), and c). The red lines represent weak Cold Pool year and the blue lines represent strong Cold Pool year. Panel d) shows the geographical locations in the along-shelf direction, from A - the Nantucket Shoals, B - the Montauk Point, C - the Sandy Hook, D - the Delaware Bay, E - the Chesapeake Bay. Minimum temperatures in the along-shelf direction on each calendar day are marked as black dots in panel f). The three stages of both strong and weak Cold Pool events - Stage I, II, and III, are separated by dashed lines with blue (strong) and red (weak) colors.

the 50-year time series. Except for the year 1986, the Cold Pool salinity anomalies during the rest of the weak years are all positive. For the years 1974 and 1990, temperature and salinity anomalies are both above one-standard deviation. However, for strong Cold Pool years, there is no such relationship with salinity anomalies. Only years 1993 and 2005 have temperature and salinity anomalies below one-standard deviation. Weak years not only have relatively higher salinities, but also have a faster salting rate of the Cold Pool. The increasing rate of minimum salinity of the Cold Pool during Stage II and III of the weak Cold Pool years is about 0.007 psu/day, faster than that during strong Cold Pool years (0.005 psu/day).

We compare the horizontal distributions of depth-averaged temperature of the Cold Pool and cold bottom water over the shelf from the MAB to the SS on the same calendar days 120, 150 and 180 between strong and weak years (Figure 3.7). During the weak years, the depth-averaged temperature of the Cold Pool is much warmer than that of strong Cold Pool year on the same calendar day. There is no appearance of the Cold Pool in the southern MAB (south of the Hudson Shelf Valley) after May in weak years. Another distinct difference between strong and weak Cold Pool years is the depth-averaged temperature of the cold bottom water in the GB and GoM, especially along the Northeast Channel. The warmer waters in the Northeast Channel further warms water in the eastern GoM, resulting from the counter-clockwise circulation. Similarly, depth-averaged salinity of the Cold Pool also shows that weak years have much saltier waters in the Cold Pool (Figure 3.7). The 33.6-psu isohaline reaches the 50-m isobath and as far north as 41 °N on calendar day 120 during weak years; while it is only located near the shelf-break of the southern MAB on the same day of the strong years. The depth-averaged salinity of the cold bottom water over the GoM also suggest a saltier inflow of subsurface waters in the Northeast Channel.

The inflow of warmer and saltier waters through the Northeast Channel and

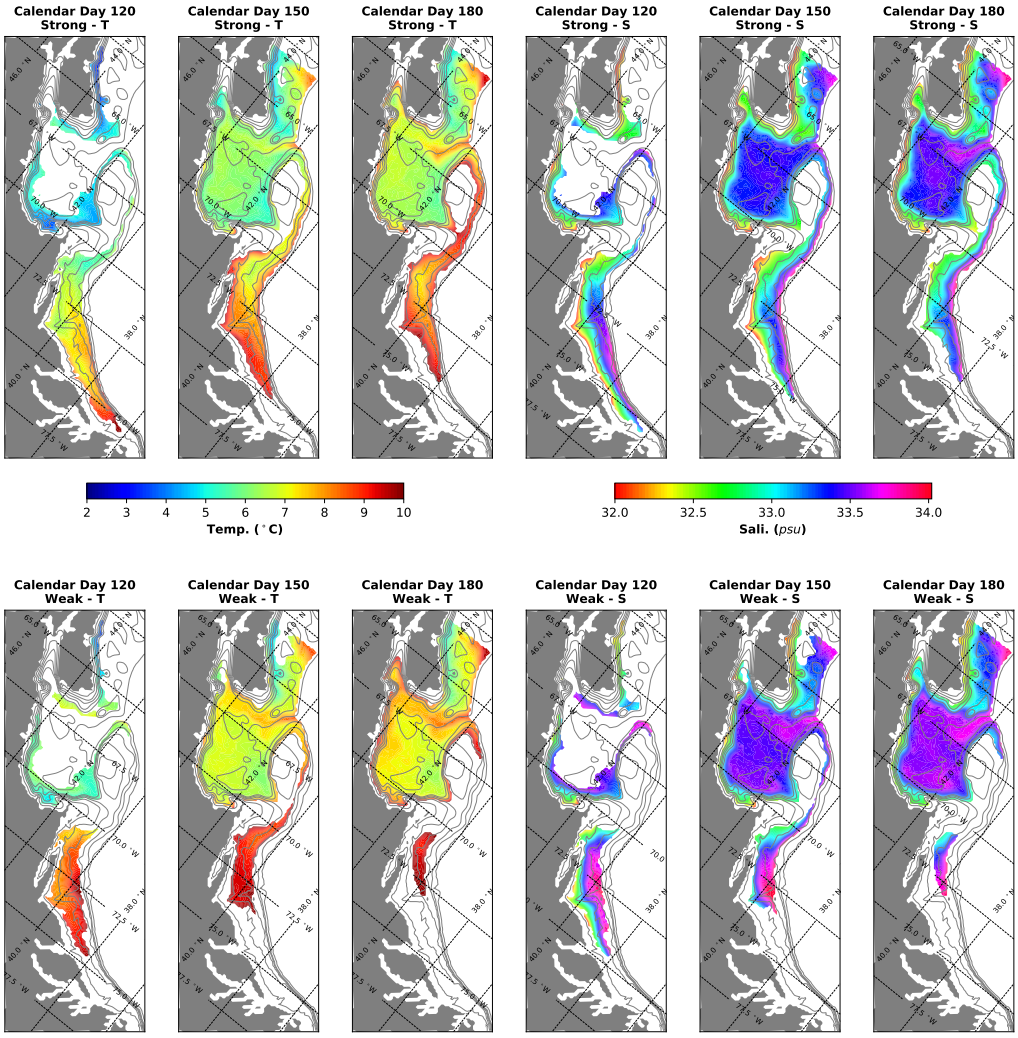

Figure 3.7: Horizontal distributions of depth-averaged temperature and salinity of the Cold Pool over the MAB and cold bottom water over the GB, GoM and SS on Calendar Day 120, 150 and 180 of strong and weak Cold Pool years.

invasion of warmer and saltier waters near the shelf-break of the MAB and GB suggest the subsurface feature on the shelf may be highly correlated with the Gulf Stream path or the impacts of warm-core rings from the Gulf Stream. Nye et al. [2011] reported that the distribution and abundance of silver hake (a cold-water-favorable species on the shelf) in the spring is highly correlated with fall Gulf Stream path and the latter leads the former by about 6 months. A detailed investigation of the relationship between the Cold Pool and the Gulf Stream path has been included in a following study.

3.4.6 Summer Progressions during Strong and Weak Cold Pool Years

The Cold Pool is not a stationary cold water mass below the thermocline, but has a southwestward progression over the mid- and outer-shelf during summer. To highlight the interannual variations of the Cold Pool movement and evolution between strong and weak Cold Pool years, average Cold Pool extents and Cold Core positions (locations of minimum depth-averaged temperatures of the Cold Pool) during strong and weak years are computed and compared in Figure 3.8.

There are some similarities in the Cold Pool summer evolution in strong and weak Cold Pool years. Both Cold Cores in strong and weak years initiate in the south of the New England, and travel in the southwestward direction along the 60-m isobath. However, the difference in Cold Pool evolutions between strong and weak years are prominent: (1) the average Cold-Core traveling speed of the strong year is about 2.1 cm/s, faster than that of weak year (1.5 cm/s); (2) the Cold Core of the strong year finally disappears in the Hudson Shelf Valley, while the Cold Core of the weak year disappears off the Montauk Point; (3) the retreating speed of the Cold Pool northern extent (4.2 cm/s) for the strong year is faster than that of the southern extent (2.1 cm/s) during Stage III, while for the weak year, the Cold Pool's southern extent retreats at almost the same speed as the northern extent (4.2 cm/s).

The northern extent's retreating speed is related to advection of upstream warm water, together with surface warming and mixing [Chen et al., 2018a]. However, the southern extent's retreating speed is related to the advection of the Cold Pool water, which competes with surface warming and mixing. Thus, the different warming/cooling effects due to advection in the northern and southern extents leads to significantly different retreating speeds, in particular during strong Cold Pool years. For weak years, the fast retreat of the Cold Pool southern

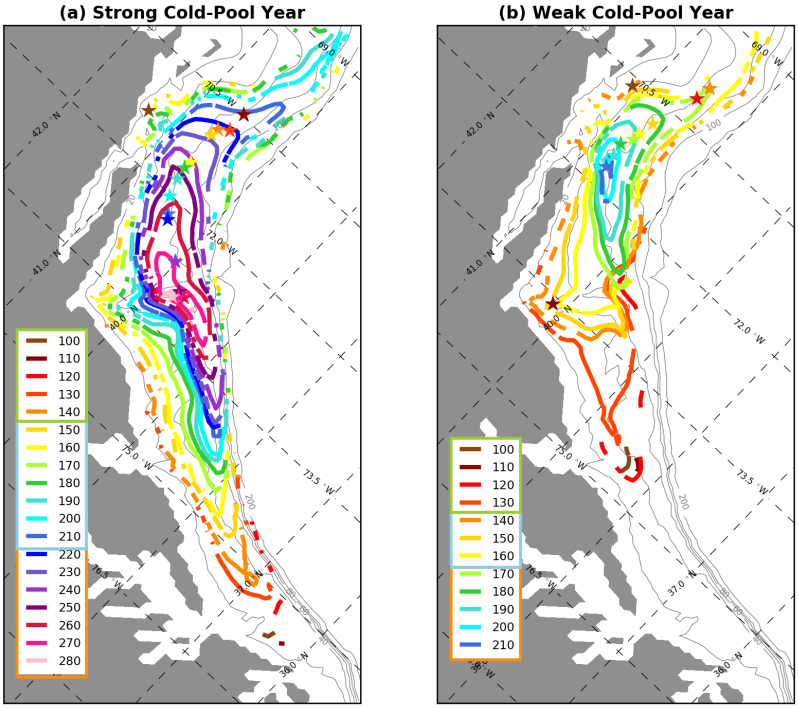

Figure 3.8: The horizontal extents (contours) and positions of the Cold Cores (stars) of the (a) strong Cold Pool event and (b) weak Cold Pool event on calendar days from 100 to 280 and from 100 to 210, every 10 days per contour/star-marks, represented by different colors.

extent suggests the advection of the Cold Pool water is too weak to compete with surface warming and mixing. A detailed quantitative study of relative importance of horizontal advection versus surface warming between strong and weak Cold Pool years is investigated in Section 3.5.

3.5 Volume-averaged Heat Budget of the Cold Pool Region

In order to investigate the difference in heat balance between strong and weak years, we compute volume-averaged heat budget of the near-bottom (below 30 m depth) control volume over the Cold Pool region (Figure 3.9 a). The Cold Pool region is considered as the near-bottom region over the mid- and outer-shelf (between 40 and 100-m isobaths) of northern MAB (Figure 3.1; represented in purple). For a near-bottom control volume V, the volume-averaged heat balance can be written as:

$$\underbrace{\frac{1}{V}\int_V \frac{\partial T}{\partial t}\,dV}_{\text{Qtrend}} = \underbrace{\frac{1}{V}\int_V K_v \frac{\partial^2 T}{\partial z^2}\,dV}_{\text{V-Dif}} \underbrace{- \frac{1}{V}\int_V u\frac{\partial T}{\partial x}\,dV}_{\text{X-Adv}} \underbrace{- \frac{1}{V}\int_V v\frac{\partial T}{\partial y}\,dV}_{\text{Y-Adv}} \underbrace{- \frac{1}{V}\int_V w\frac{\partial T}{\partial z}\,dV}_{\text{Z-Adv}} \tag{3.2}$$

where T represents temperature, u, v, w represent velocities at three different directions, V is total volume of the control volume, K_v is the vertical diffusion coefficient (m^2/s). The volume-averaged heat budget equation states that time rate of change in the heat storage is balanced by the net air-sea heat flux and horizontal advective heat fluxes. The cumulative heat balance of Equation (3.2) can be expressed as:

$$\int_{t_0}^{t} \text{Qtrend}\; dt' = \int_{t_0}^{t} \text{V-Dif}\; dt' + \int_{t_0}^{t} \text{X-Adv}\; dt' + \int_{t_0}^{t} \text{Y-Adv}\; dt' + \int_{t_0}^{t} \text{Z-Adv}\; dt' \tag{3.3}$$

where t_0 is the initial time for time integrating. The average temperature of the control volume can be expressed as:

$$T(t) \;=\; T(t_0) \;+\; \int_{t_0}^{t} \text{Qtrend}\; dt' \tag{3.4}$$

where $T(t_0)$ is the initial temperature at time t_0. The time series of heat budget terms for each year begins from November 1^{st} of the previous year. The time series is separated into cooling and warming periods based on the values of instantaneous heat trend; which is easy for discussion. The cooling period is from November to mid-March, while the warming period is from mid-March to the end of October.

3.5.1 Composite Analysis between Strong and Weak Years

The cumulative volume-averaged heat balance of the Cold Pool region has a distinct difference in heat advection between weak and strong years during the cooling period (Figure 3.9). Total heat advection has a warming effect on the Cold Pool region during this period, mainly contributed by the horizontal advection term in the y-direction. The warming rate from total advection of the weak years has a larger-than-climatology weakening during the cooling period. The total advection warms the Cold Pool region by 5.62 °C in weak years, and by 4.70 °C in strong years, which contributes about 0.92 °C difference in early spring (mid-March) between strong and weak years. However, vertical diffusion in weak years has a slightly larger cooling effect during this period, which compromises the difference by 0.14 °C. Therefore, without consideration of initial temperature difference on November 1st, Cold Pool region has a warmer temperature by about 0.75 °C in the early spring in weak years than strong years. During the warming period, temperature difference contributed from total advection enlarges to 1.82 °C by the end of May, and maintains to about 1.89 °C during the summer (June-July-August) (Figure 3.9). Similarly, temperature difference contributed from vertical diffusion also enlarges to -0.61 °C by the end of May, and maintains

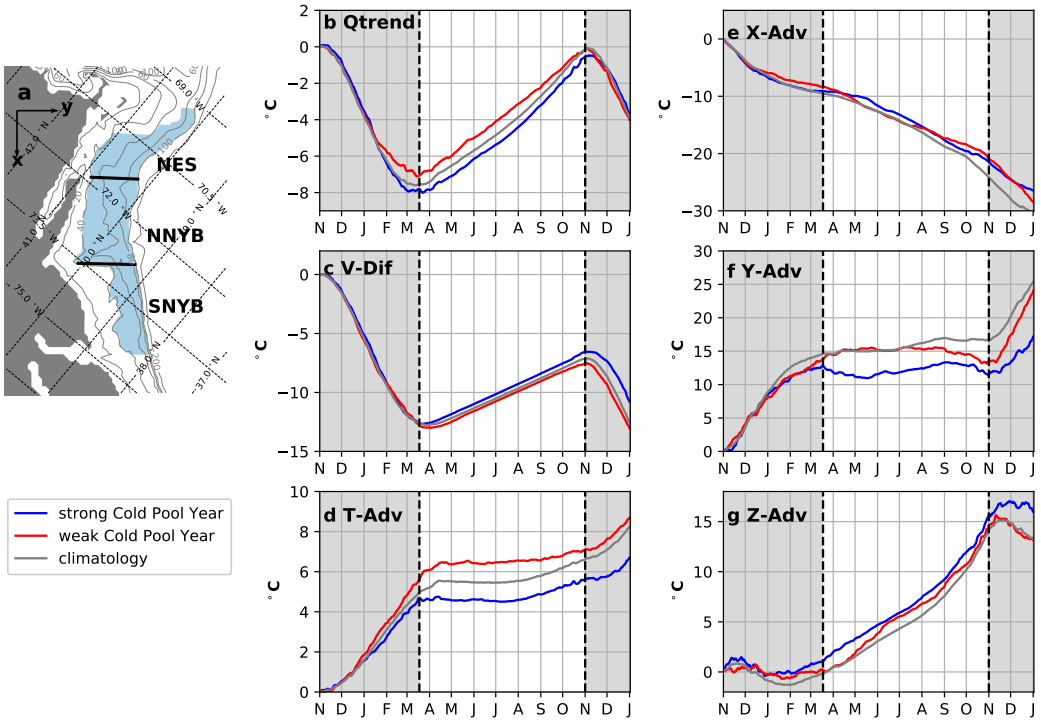

Figure 3.9: (a) Location of the near-bottom control volume between 40- and 100-m isobaths and below the 30-m depth, which is separated into three subregions - the New England Shelf (NES), the Northern New York Bight (NNYB) and the Southern New York Bight (SNYB). (b)-(g) Cumulative volume-averaged temperature budget terms (unit: °C) of strong (blue) and weak (red) Cold Pool years and the 50-year climatology (gray) based on Equation 3.3: (b) heat trend (Qtrend), (c) vertical diffusion (V-Dif), and (d) total advection (T-Adv), which combines three advective terms in different directions: (e) x-direction advection (X-Adv), (f) y-direction advection (Y-Adv), and (g) veritical advection (Z-Adv). The time series of heat budget terms begins from November 1st of the previous year.

to about -0.62 °C during the summer. This implies that, during the warming period, the difference in vertical diffusion (weak minus strong) does not make positive contributions to the temperature anomaly in cumulative heat trends, but rather an increasing negative contribution during the warming period. It is the positive deviation (weak minus strong) in total advection between weak and strong Cold Pool years that compensates for the negative contribution from the vertical diffusion. Therefore, the Cold Pool region is warmer by about 1.27 °C in weak years than strong years during the summer.

This temperature difference in the summer between weak and strong years is mainly contributed by horizontal advection in the y-direction, compared with the other two advective terms. The y-direction heat advection has a warming effect (0.57 °C/month) in the spring (March-April-May) of weak years, but a cooling effect (-0.45 °C/month) in the spring of strong years. This distinct difference in warming rates in spring between weak and strong years contributes to the enhancement in temperature difference in the summer. The initial temperature of the cooling period is about 6.82 °C for strong Cold Pool years and 7.33 °C for weak years. According to Equation (3.4), the warmer initial temperature in weak years augments the temperature difference of the following summer to 1.78 °C on average between weak and strong years, which is comparable with the difference in the Cold Pool minimum temperature between weak and strong events (Section 3.4.5). Therefore, we suggest that warmer initial temperature in the early spring (mid-March) and higher positive deviations in y-direction advection between weak and strong Cold Pool years are the two main factors that contribute to warmer temperatures of the Cold Pool region during the summer.

3.5.2 Interannual Variability in Heat Budget Terms

Based on the composite analysis on the Cold Pool temperature in Section 3.4.5, warming rates of the Cold Pool minimum temperature keeps consistent (about

1 °C/month) between weak and strong years, even though the minimum temperature in weak years is warmer by about 2 °C during the summer than that in strong years. Analysis on the 50-year net warming rates (represented by the Qtrend term in Equation 3.2) of the Cold Pool region suggests that there is little difference between strong and weak years (Figure 3.10). The net warming rates of the Cold Pool region is about 0.90 °C/month on average during the spring (March-April-May) and about 1.24 °C/month during the summer (June-July-August). The net warming rates in the spring ranges from 0.53 °C/month in 1990 to 1.27 °C/month in 1996, and in the summer it ranges from 0.37 °C/month in 1976 to 2.04 °C/month in 1971. The minimum warming rates are obtained in weak Cold Pool years rather than strong years. The average warming rates among strong and weak years are the same in the spring, with a value of 0.89 °C/month. The correlation analysis between the CPI and warming rates in spring and summer suggest that they are not significantly correlated with each other. This suggests that the net warming rates in spring and summer do not correlate with the strength of the Cold Pool events. Strong Cold Pool years may have larger net warming rates in the spring and summer. However, net warming rates do have impact on the temperature at the end of summer. Interannual variation in temperatures at the end of August is significantly correlated with summer net warming rates ($R_{corr} = 0.65$, $p < 1e - 6$).

Although the net warming rates does not show large correlation with strong and weak Cold Pool years, its interannual variability does exist and is mainly controlled by the interannual variations of total advection (Figure 3.10). The correlation coefficient between the net warming rates and total advection reached 0.94 in the spring and 0.92 in the summer. However, interannual variation in vertical diffusion does not correlate with net warming rates neither in spring nor in summer. Among the advective terms, only advection in y-direction has a relatively-high correlation coefficient of 0.45, significant at 99% confidence level.

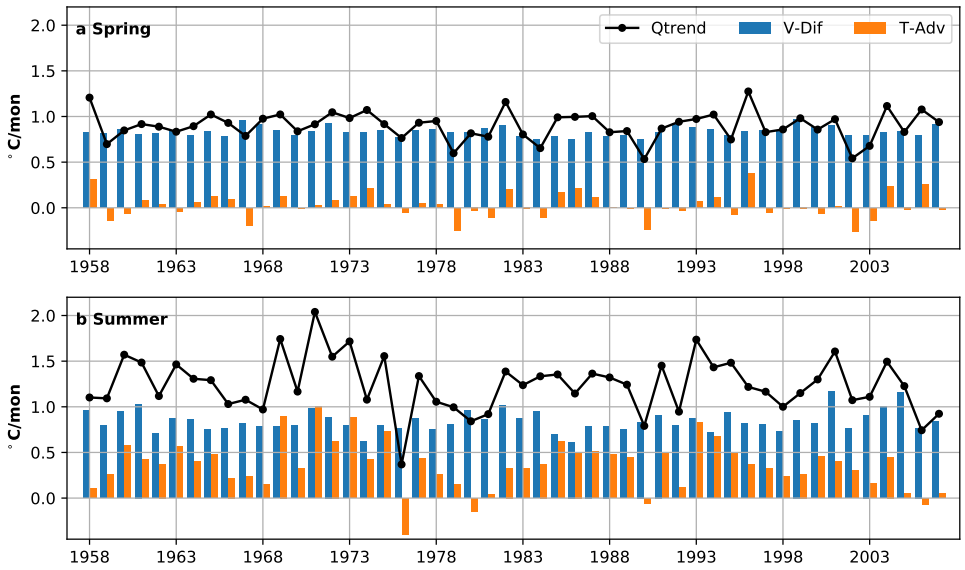

Figure 3.10: Interannual variability of volume-averaged heat budget terms (unit: °C/month) during the (a) spring (March-April-May) and (b) the summer (June-July-August). According to Equation 3.2, rate of change in temperature (Qtrend) is contributed by vertical diffusion (V-Dif) and total heat advection (T-Adv).

This suggests that the net warming rates in the spring and summer are mainly modulated by the total heat advection, rather than vertical heat diffusion.

Unlike the net warming rates, interannual variation in the initial temperature in the early spring is significantly correlated with the CPI, with a correlation coefficient of 0.92. The temperature of the Cold Pool region in the spring and summer are both significantly correlated with the CPI, with correlation coefficients equal to 0.92 and 0.67, respectively.

3.5.3 Relative Importance of Initial Temperature and Advection

Considering the impact of initial temperature on the strength of Cold Pool events, we investigate the relative importance of initial temperature and total advection

during cooling and warming periods. Anomalies of heat budget terms from the respective climatological values are computed and compared among strong and weak years for both the cooling and warming periods (Figure 3.11). According to Equation (3.4), the average temperature of the Cold Pool region is determined by the initial temperature at mid-March, the cumulative vertical heat diffusion and total heat advection. The correlation between the time series (1959-2007) of average temperature of the Cold Pool at the end of May and the temperature calculated from the heat budget equation is about 0.96 with 100% significance level. The correlation between the time series of the CPI and the average temperature of the region at the end of May (Figure 3.11 a) is about -0.85. Therefore, it is reasonable to use the temperature in the Cold Pool region calculated from the heat budget equation as an indicator of the Cold Pool strength.

During the spring of warming period (mid-March to the end of May), the Cold Pool region has a negative temperature anomaly (-0.56 °C), on average, during the strong years (Figure 3.11 b). On average, the temperature anomaly for strong years is mainly driven by the initial temperature anomaly at mid-March (-0.54 °C). The anomalies from Qtrend (-0.03 °C) exerts minor influence on the temperature anomaly from mid-March to May of strong years. Similarly, weak years have a positive temperature anomaly (+0.64 °C) during the same period, which is mainly forced by the initial temperature at mid-March (+0.66 °C) (Figure 3.11 c). During this period, the advective terms in all three directions and vertical diffusion are also in compensation with each other and exert minor influence (-0.02 °C). The initial temperature anomalies at the beginning of the warming period sets the character of the temperature anomaly in the late spring and early summer for both strong and weak Cold Pool years. However, there are some exceptions. For some strong years, for example 1979 and 1984, total advection contributes more negative anomalies than the initial temperature.

To further investigate relative contributions of initial temperature in the early

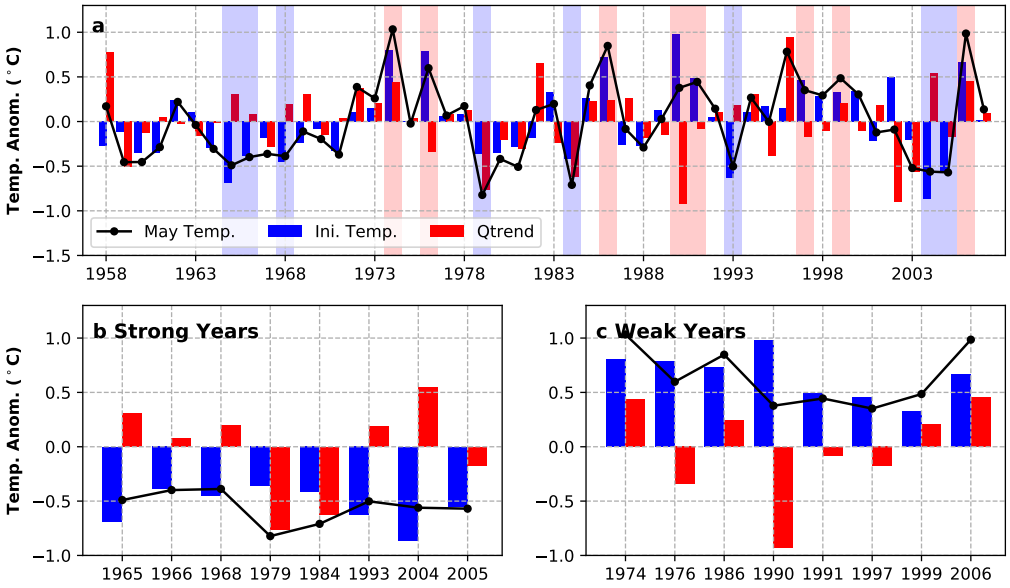

Figure 3.11: Relative importance in temperature anomalies (compared to 50-year climatology; unit: °C) of the Cold Pool region during the spring of warming period (mid-March to the end of May) from the initial temperature (blue) and Qtrend (red) for (a) all 50 years, (b) strong and (c) weak Cold Pool years. The net volume-averaged temperature anomalies of the Cold Pool region are shown in black solid lines in each panel. Strong and weak Cold Pool years are indicated by blue and red background colors in (a), respectively.

spring (mid-March) and warming rate to interannual variations in the temperature of the Cold Pool region, we performed correlation analysis between monthly temperature and the calculated heat budget terms. Results suggest that monthly temperature of the Cold Pool region is consistently correlated with calculated temperature based on the heat budget equation, with a coefficient of about 0.9. The initial temperature in the early spring has a decreasing correlation with monthly temperature of the Cold Pool region. The correlation coefficient decreases from 0.80 in April to only about 0.27 in October. However, total advection has an opposite situation. The correlation between monthly temperature and total advection increases from 0.5 in April to 0.75 in October. This suggest that, from April to July, it is the initial temperature that controls the interannual variation in temperature of the Cold Pool region; however from August to October, total advection take controls in impacting temperature variation of the Cold Pool region. The sub-domains of the NES, NNYB and SNYB have similar results, but have a difference in the time of shift.

To sum up, during the warming period, the volume-averaged temperature anomaly in the Cold Pool region is largely determined by the initial temperature anomaly in the early spring. Vertical mixing does not positively contribute to the abnormal cooling/warming of the Cold Pool region, but usually was a counter effect. Total advection contributes to positive temperature anomaly in weak years and negative anomaly in strong years, but it is usually smaller than the initial temperature anomaly in the early spring. There are exceptions for some years. The relationship between initial temperature anomaly in the early spring and temperature anomaly in the Cold Pool region suggests a seasonal predictability that warrants further investigation.

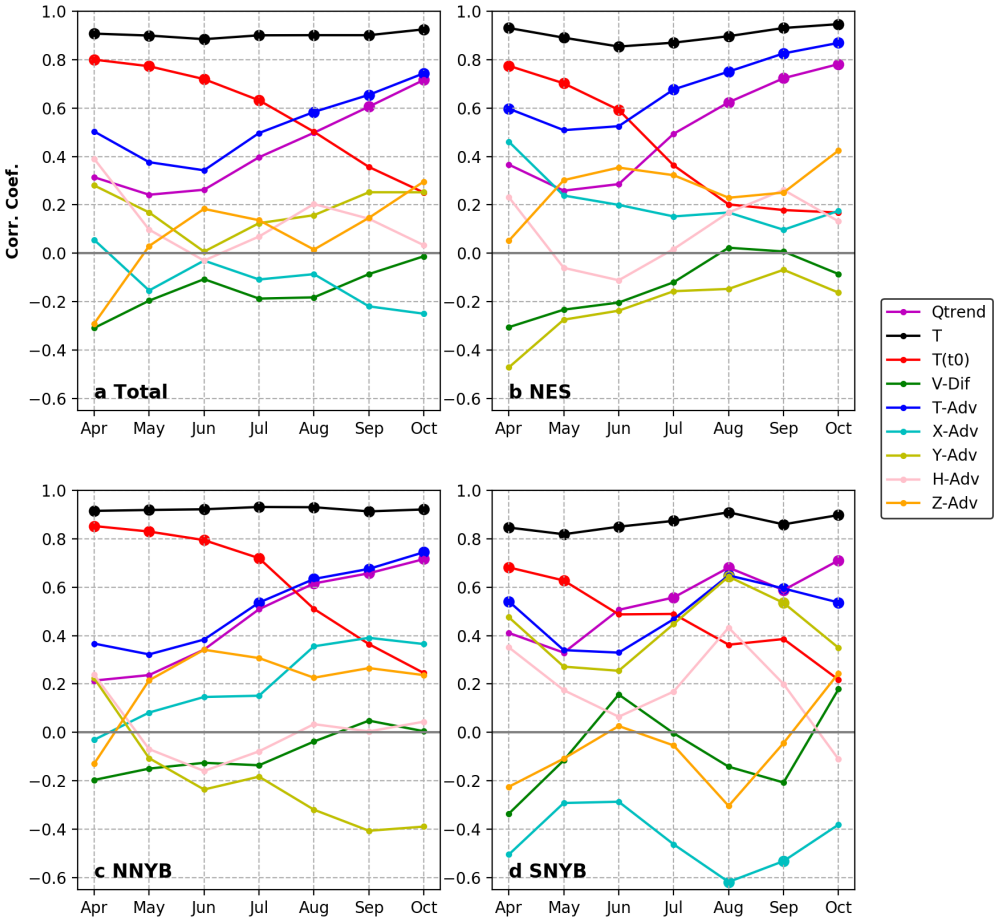

Figure 3.12: Relative contributions of initial temperature in the early spring (mid-March) and warming rate to interannual variations in the temperature of (a) whole Cold Pool region, (b) New England Shelf (NES), (c) Northern New York Bight (NNYB) and (d) Southern New York Bight. Correlation coefficients are computed between monthly-averaged temperature of the region and calculated heat budget terms, according to Equation 3.3 and 3.4. Correlations that with p value ¡ 1e-4 are plotted in larger markers.

3.6 Summary

In this study, we investigate the interannual variability of the Cold Pool based on the long-term (1958-2007) high-resolution regional numerical model. The persistence of the Cold Pool shows significant interannual variability during the 50 years of integration. The Cold Pool peak volume also exhibits significant interannual variability, with a positive correlation ($r = 0.69$) with the persistence time. The accumulated Cold Pool volume exhibits relatively weak negative correlations with minimum temperature ($r = -0.43$) and mean temperature ($r = -0.61$), suggesting that colder (warmer) minimum temperatures are not necessarily associated with a larger (smaller) total volume. The volume-averaged Cold Pool temperature shows a strong seasonal variation as well as significant interannual variability during the 50 years. The cumulative volume anomaly is highly correlated with average Cold Pool temperature anomalies in May and June, with correlation coefficients equal to -0.71 and -0.82, respectively. However, the correlations between the cumulative Cold Pool volume anomaly and average salinity anomalies in May ($r = -0.38$) and June ($r = -0.46$) are less significant when compared to temperature.

Based on the persistence time, volume and volume-averaged temperature, we computed the Cold Pool Index (CPI) in order to evaluate the strength of the Cold Pool in a given year. Strong and weak years are identified according to their CPI values. Except for 1986, weak years all have relatively high salinities. In contrast, during strong years, there is no significant relationship with salinity. The equatorward progression of the Cold Pool during summer varies between strong and weak years, such that: (1) the average cold-core propagation speed is 2.1 cm/s during strong years, faster than that of weak years (1.5 cm/s); (2) the northern extent of the Cold Pool area retreats faster than that of the southern extent during strong years, while it retreats as fast as the southern extent during

weak years; (3) the core of the Cold Pool finally disappears in the Hudson Shelf Valley for strong years and off the Montauk Point for weak years. During strong years, horizontal advection of the Cold Pool water compensates surface warming and mixing in the southern retreat process, slowing the retreat speed. During weak years, advection of Cold Pool water is too weak to overcome warming and mixing from the surface.

A detailed quantitative study of the volume-averaged heat budget of the Cold Pool region between strong and weak years was also investigated. Results suggest that a warmer initial temperature and higher positive deviations in total advection are the two main factors that contribute to warmer temperatures of the Cold Pool region during the summers of weak years. Abnormal warming/cooling from the initial temperature and horizontal advection impact the interannual variability in the temperature of Cold Pool events. By computing the relative importance of horizontal advection and initial temperature during the cooling and warming period, we concluded that the volume-averaged temperature anomaly in the Cold Pool region is largely determined by the initial temperature anomaly in the early spring, and additionally contributed to by total advection.

Here, we quantified the significant interannual variability of the MAB Cold Pool. It is beyond the scope of this paper to fully explore the large-scale drivers of that variability. In following work, we will explore the variability in the Northwest Atlantic continental shelf in relation to North Atlantic climate. Furthermore, the relationship between the initial temperature anomaly in the early spring and the temperature anomaly in the Cold Pool, as presented in this paper, suggests that seasonal predictability may be possible, which warrants further investigation.

Chapter 4

Changes of Bottom Waters over the Mid-Atlantic Bight Continental Shelf in Connection with the Gulf Stream and the North Atlantic Oscillation

4.1 Abstract

The Cold Pool average location has been reported to have a poleward shift during its weak (warmer) years, along with a northward shift of the Gulf Stream position. Interannual characteristics of the Cold Pool are quantified using a high-resolution hindcast simulation of the Northwest Atlantic Ocean. The relationship between the Cold Pool temperature and the north-south shift of the Gulf Stream position are investigated. The spring Cold Pool temperature has a significant positive correlation with the annual Gulf Stream index. Besides, the fall Gulf Stream position is significantly correlated with the Cold Pool temperature in the following spring, enhancing the use of the fall Gulf Stream position as a leading indicator of the Cold Pool temperature. The Cold Pool temperature also has a positive response to the winter NAO, with the Cold Pool temperature lagging the NAO by approximately 2 years. The possible mechanistic link between the Cold Pool temperature, Gulf Stream position and the NAO are discussed.

4.2 Introduction

The Mid-Atlantic Bight (MAB) Cold Pool is a distinctive bottom-trapped cold and fresh water mass below the seasonal thermocline, and located over the mid- and outer-shelf of the MAB [Houghton et al., 1982, Chen et al., 2018a, Chen and Curchitser, 2018b]. The Cold Pool water, as part of the MAB shelf water, is one of the most important water masses of a large-scale buoyancy-driven coastal current system flowing from the Labrador Shelf to the MAB. There is ample evidence showing that the Cold Pool has an important impact on the marine ecosystem of the MAB, especially on the recruitment and settlement of several cold-temperatures commercially important fish species, e.g., silver hake and yellowtail flounder [Nye et al., 2011, Miller et al., 2016, Sullivan et al., 2005].

Variations of temperatures over the continental shelf have been reported in relation with intrusion of warm core rings and the GS water masses [Gawarkiewicz et al., 2012, Zhang and Gawarkiewicz, 2015, Gawarkiewicz et al., 2018], as well as changes in the offshore slope waters and intrusion of the slope waters [Petrie and Drinkwater, 1993]. The slope waters are a mixture of colder and fresher LSW and Warm Slope Water (WSW) influenced by the GS [Smith et al., 2001, Drinkwater et al., 1998, Mountain, 2012]. It has long been recognized that the hydrography of the slope waters strongly depends on the transport of the deep Labrador Current (LC) (100-300 m) that travels southward along the continental shelf from the tail of the Grand Banks to the southwestern flank of Georges Bank [Petrie and Drinkwater, 1993, Drinkwater et al., 1998]. During the years of higher than average transport, the LSW could reach as far south as the MAB [Drinkwater et al., 1998]. However during low-transport years, WSW is dominant as the Labrador Slope Water is primarily restricted to the north [Drinkwater et al., 1998]. The southward transport of the colder and fresher LSW is suggested to be related to the an increase of the LC, which is further associated with a decrease

in the North Atlantic Oscillation (NAO) index [Drinkwater et al., 1998]. The percent of Labrador Slope Water (LSW) inflow into the Gulf of Maine (GoM) at depth through the Northeast Channel was estimated and found to be negatively correlated with the NAO with a lag of 2 years [Mountain, 2012].

The NAO is recognized as the most significant pattern of the large-scale atmospheric circulation in the North Atlantic [Stephenson et al., 2003]. It is characterized as the difference in the pressure gradient between the Azores High (AH) and the Icelandic Low (IL). During positive NAO phases, the lower-than-usual IL intensifies as well as the westerly winds over the Labrador Sea, which is a region of deep-water formation [Visbeck et al., 2003]. Decrease in air temperature and increase in the heat loss from the ocean cools the ocean and further increases deep winter convection [Drinkwater et al., 1998, Franks, 2015]. Outflow of Labrador Sea Water has three separate branches: towards the European Basin; southeastward under the North Atlantic Current (NAC); southwestward towards the Grand Banks as part of the Labrador Current [Franks, 2015]. Among these, the newly-formed Labrador Sea Water flows preferentially southeastward under the NAC, causing a decrease in the southwestward transport of the LC along the continental shelf [Bersch et al., 2007].

Oppositely, negative NAO phases with reduced pressure gradient between the AH and the IL leads to decreased winds and warmer sea temperature, which further reduces deep winter convection in the Labrador Sea. Subsequently, the southwestward transport of the LC increases along the Labrador continental shelf and into the Slope Sea. The NAO forced temperature signal continues propagating southwestward from their high latitude source regions to the lower latitudes, along the outer continental shelf and slope regions of the Northwest Atlantic [Greene et al., 2013]. The significant relationship between the NAO and southward transport of the LC is reconfirmed and investigated by Han et al. [2010]

based on satellite altimetry data and conductivity-temperature-depth observations.

It also has been documented that changes in sea surface temperature (SST) and circulation in the Slope Sea is strongly correlated with changes in the north-south shift of the GS position [Franks, 2015]. The flow of water from the Labrador Shelf to the Slope Sea is suggested to be the main process that impacts the north-south fluctuations of the GS [Rossby and Benway, 2000, Rossby, 1999]. According to Franks [2015], the reduction of southwestward transport of the LSW allows for the northward shift of the GS during positive NAO years; while increase of the LSW transport during negative NAO years is suggested to precede southward shifts of the Gulf Stream. It has been reported that the northward (southward) shift of the Gulf Stream has a 2-year lag with positive (negative) NAO [Taylor and Stephens, 1998, Joyce et al., 2000].

Many recent studies have predicted the spatial distribution and biomass of marine organisms over the shelf by using the GS path index and the NAO index as predictors [Xu et al., 2018, Davis et al., 2017]. However, as an important media linking the organisms and the large-scale processes, how the Cold Pool responds to the north-south fluctuations and the phases of the NAO have not been investigated yet, due to limited temporal and spatial resolution of observation. Therefore, a high-resolution hindcast model of the Northwest Atlantic Ocean is used to investigate the possible mechanism. Seasonal and interannual variability of the Cold Pool have been investigated by applying a quantification method to this high-resolution model [Chen et al., 2018a, Chen and Curchitser, 2018b]. In this study, we investigate the long-term changes of the Cold Pool temperature and its relationship with the north-south shift of GS and response to fluctuations of the NAO, in order to understand the likely mechanistic link among the Cold Pool temperature, the GS position and the NAO.

This paper is organized as follows. In Section 4.3, we introduce the Cold Pool

data produced and quantified from a high-resolution model, as well as the NAO and GS index used in this study. Section 4.4 includes the relationship behind the Cold Pool spatial shift along with the GS position, and its response to the NAO. Finally, we will discuss the results and possible mechanistic linkage between the Cold Pool and the NAO in Section 4.5.

4.3 Data and Methods

The interannual characteristics of the Cold Pool has been investigated in Chen and Curchitser [2018b] using a long-term (1958-2007) high-resolution (horizontal: about 7 km; vertical: 40 terrain-following layers) Regional Ocean Modeling System (ROMS) simulation of the Northwest Atlantic Ocean, extending from the Gulf of Mexico to the Gulf of St. Lawerence. The model captures the spatial variability of the Cold Pool from seasonal to interannual time scales by applying three quantification criteria following its definition [Chen et al., 2018a]: (1) *Temperature & Salinity Criteria*: the Cold Pool temperature is below 10 °C; salinity is defined to be lower than 34 *psu*, in order to separate the Cold Pool from the slope waters [Mountain, 2003]; (2) *Stratification Criterion*: the Cold Pool develops along with the onset of thermal stratification, which is determined by calculating the mixed layer depth; (3) *Location Criterion*: the Cold Pool is located below the mixed layer, between the 20- and 200-m isobaths of the MAB, with no direct contact with the air-sea interface. In this study, we focus on understanding the relationship between the Cold Pool temperature and the GS position and its response to the NAO. Mean (yearly-averaged), spring (April-June) and summer (July-September) temperatures of the Cold Pool are used in the analysis.

The GS index is an index that well describes the north-south shift of the GS position. It is constructed based on historical subsurface temperature data at 200m depth between 55 ° and 75 °W. An Empirical Orthogonal Function

analysis was used to extract the dominant mode of the mean location of the 15 °C isotherm at the 200m depth. Details in the construction of the index are given in [Joyce et al., 2000]. Seasonal and annual-mean values of the GS index are used in this study. Positive (negative) values of the GS index indicate a northward (southward) shift. The January-March(JFM) mean NAO index is calculated as the winter NAO index (available at www.cpc.ncep.noaa.gov/products/precip/CWlink/pna/nao.shtml). Pearson correlations are calculated between the Cold Pool temperature and seasonal GS index, as well as the winter NAO index, in order to identify significant statistical relationships. A quadratic fit of each time series is calculated to investigate and compare their long-term trends from 1958 to 2007.

4.4 Results

4.4.1 Shift in the Cold Pool Spatial Distribution

According to Chen and Curchitser [2018b], strong (1960, 1965, 1966, 1968, 1979, 1980, 1984, 1993, 2004, and 2005) and weak (1974, 1975, 1976, 1986, 1990, 1991, 1999, and 2000) Cold Pool years are identified based on their Cold Pool index. Composite analysis of strong and weak years shows significant interannual oscillations in the Cold Pool characteristics (volume, temperature and persistence time) and its summer progression (Figure 4.1). Strong years have a longer persistence time (about 6.5 months from early April to October) than the weak years (about 4 months from early April to the end of July) [Chen and Curchitser, 2018b]. The Cold Pool mean temperature is about 2 °C warmer during the weak years and its volume is only about one-third of that in strong years [Chen and Curchitser, 2018b].

The Cold Pool also have larger horizontal extents during strong years, both in the along-shelf and across-shelf direction. For example, on calendar day 180 of

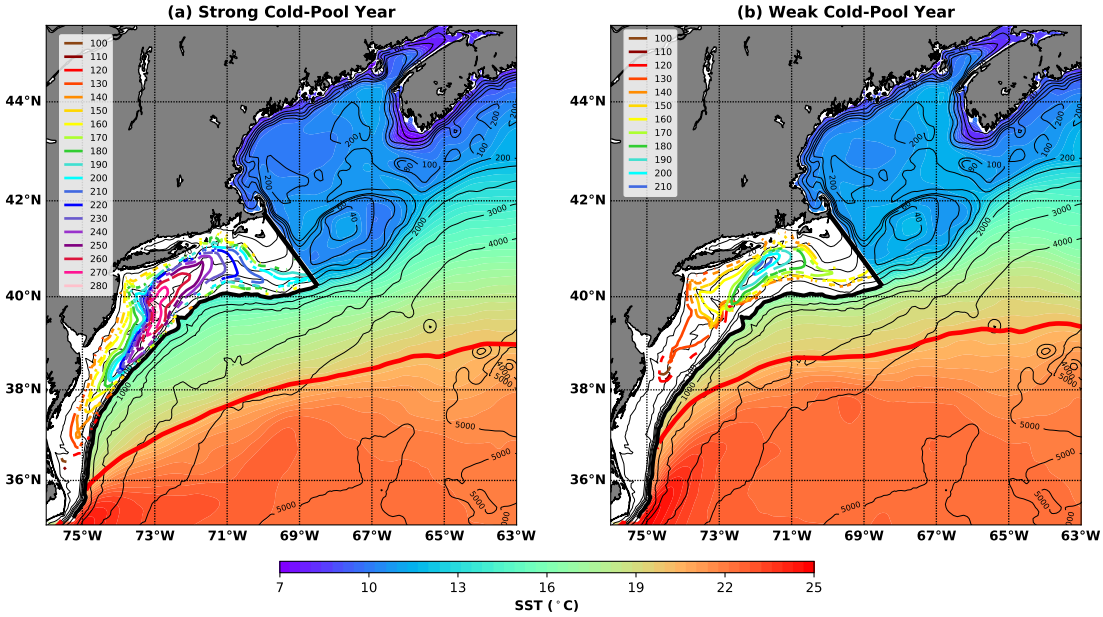

Figure 4.1: Shift in spatio-temporal distribution of the MAB Cold Pool and the corresponding annual-mean SST over the Northwest Atlantic Ocean during (a) strong and (b) weak Cold Pool years. Horizontal extents of the Cold Pool during strong and weak years are contoured in different colors on calendar days from 100 to 280 and from 100 to 210, every 10 days per contour. The 20 °C isotherms of annual-mean SST are plotted in red in both panels, indicative of the Gulf Stream position. The black line in each panel demarcates the boundary between the MAB and the rest region. Contours of depth are given every 20 meters from 20 to 100 m, every 100 meters from 100 to 200 m, and every 1000 meters from 1000 to 5000 m.

strong years, the Cold Pool reaches the 38 °N of latitude in the south and spreads over the 40- to 100-m isobaths in the across-shelf direction; while for the same day of weak years, the southern extent of the Cold Pool is around the 40 °N, and the Cold Pool only spreads over the 40- to 70-m isobaths. Additionally, spatial distribution of the Cold Pool have an obvious shift between strong and weak years (Figure 4.1). The average location of the Cold Pool has a poleward shift during weak years when compared with strong years. During the summer, the Cold Pool travels southwestward and gradually dissolves mainly in the along-shelf direction. It finally disappears near the Hudson Shelf Valley during strong years but much northward off the Montauk Point during weak years.

Figure 4.1 also shows the corresponding sea surface temperature (SST) distribution over the Northwest Atlantic Ocean during strong and weak Cold Pool years. The GS position is indicated by the 20 °C isotherm. The relative GS position during strong and weak Cold Pool years indicates that the GS has a poleward shift as well during the weak years. In addition, the surface slope water between the continental shelf and the Gulf Stream and surface GoM water are both warmer during weak Cold Pool years. Further investigations on the relationship between the Cold Pool and the GS position are given in Section 4.4.2.

4.4.2 Relationship between the Cold Pool Temperature and the Gulf Stream Position

The GS originates from the North Atlantic Equatorial Current, begins from the Florida Strait and diverges northeastward near the Cape Hatteras [Franks, 2015]. It is also the surface limb of the Atlantic Meridional Overturning Circulation (AMOC), with a northward transport of warm and salty waters from low to high latitudes [Buckley and Marshall, 2016]. It has been suggested that the GS north-south position, rather than its velocity, width and volume transport, plays

a dominant role in affecting the adjacent waters [Rossby and Gottlieb, 1998]. To quantify the relationship observed in Figure 4.1, we perform cross-correlation and lead-lag correlation analysis on the 50-year time series between the Cold Pool temperature and the Gulf Stream path index from 1958 to 2007.

The cross-correlation analysis shows that the Cold Pool temperature is significantly correlated with the annual GS index (Figure 4.2; Table 4.1). The correlation coefficient between annual GS path index and Cold Pool mean temperature is about 0.45, significant above the 99.9% confidence level. Compared with summer Cold Pool temperature, the spring temperature has a higher correlation relationship with the annual GS index ($r = 0.52$; $p < 0.001$). After removing the linear trends of both time series, the correlations are almost the same and still statistically significant at the 99.9% confidence level. This implies that the Cold Pool temperature, in particular its spring temperature has a significant correlation with the GS north-south shift. The positive correlation coefficients are coherent with our previous hypothesis that the Cold Pool temperature increases (decreases) when the GS position has a northward (southward) shift. Linear regressions of the Cold Pool temperatures on the annual GS index also confirm the positive relationship between the two time series (Figure 4.3). Among them, the linear regression of spring Cold Pool temperature on the annual GS index has a maximum coefficient of determination ($r^2 = 0.274$, $p < 10^{-4}$), indicating a close association between the two series.

Table 4.1: Cross-correlation between annual-mean GS index and Cold Pool (CP) mean, spring and summer temperatures.

Annual GS index &	With trend	Without trend
Mean CP temp.	r=**0.45**; p=0.001	r=**0.45**; p=0.001
Spring CP temp.	r=**0.52**; p<0.001	r=**0.50**; p<0.001
Summer CP temp.	r=**0.44**; p=0.001	r=**0.44**; p=0.001

Figure 4.4 shows the relationship of the long-term changes of the Cold Pool

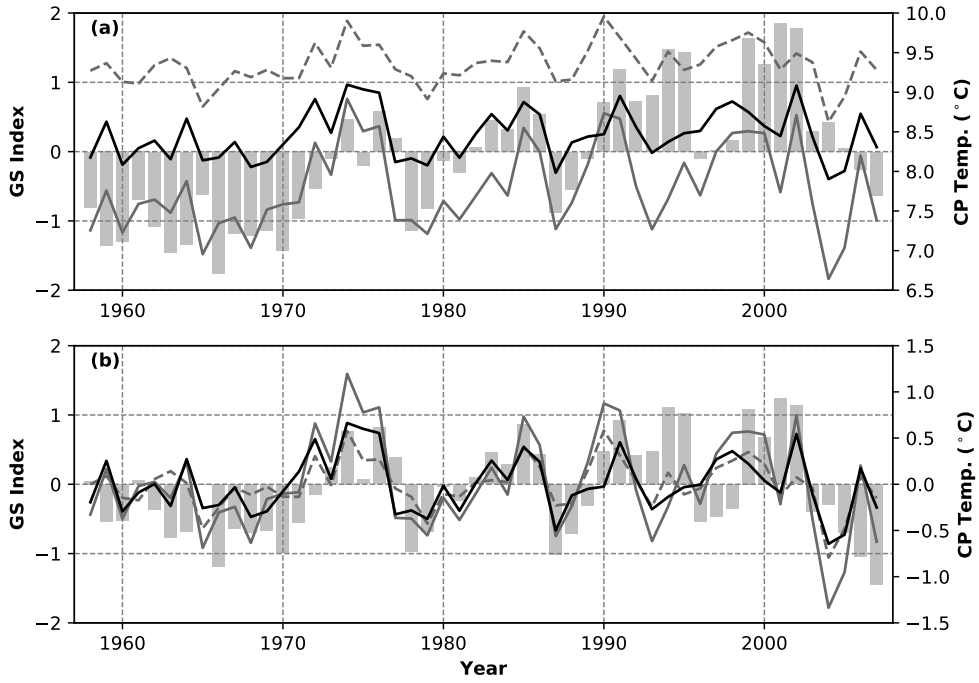

Figure 4.2: Relationship between the annual Gulf Stream position (gray bars) and the Cold Pool mean (black solid), spring (gray solid) and summer (gray dashed) temperatures, with (a) and without (b) linear trends.

spring temperature and annual GS path index. Quadratic fits of both time series are calculated and represent their long-term trends. The Cold Pool spring temperature has a cold period in the 1960s, during which the GS position is negative (southward shift). Later, both spring temperature and the GS index have an increase until 1990s. The correlation between the two time series from 1958 to 1991 reaches the maximum correlation coefficient of 0.71 ($p < 10^{-5}$). However, after the 1990s, the trends of the two time series become different (Figure 4.5). The Cold Pool spring temperature begins to decrease after the 1990s, while the GS position has a gradual increase. The correlation between the two time series from 1991 to 2007 is only about 0.35. The residuals of both time series have a positive relationship as well. A linear regression of the residuals is highly significant ($r^2 = 0.227$ and $p < 0.001$).

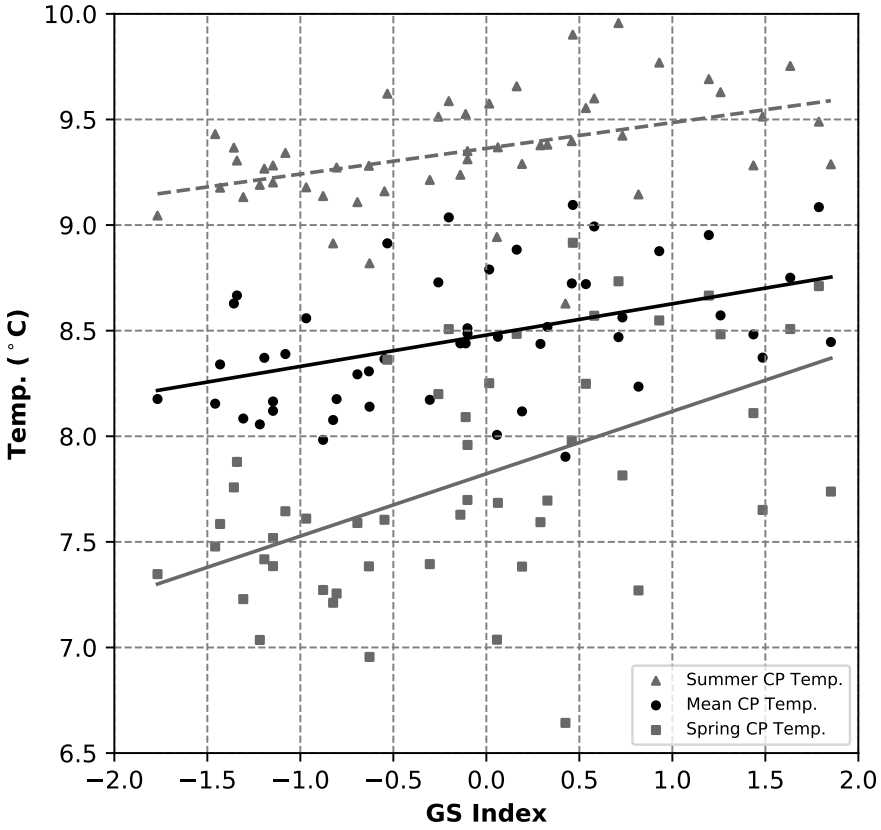

Figure 4.3: Scatter plot of the Gulf Stream position (GS Index; x-axis) versus the Cold Pool mean (black circles), spring (April-May-June; black triangles) and summer (July-August-September; gray squares) temperatures; the straight lines represent the corresponding 1-d linear regression lines.

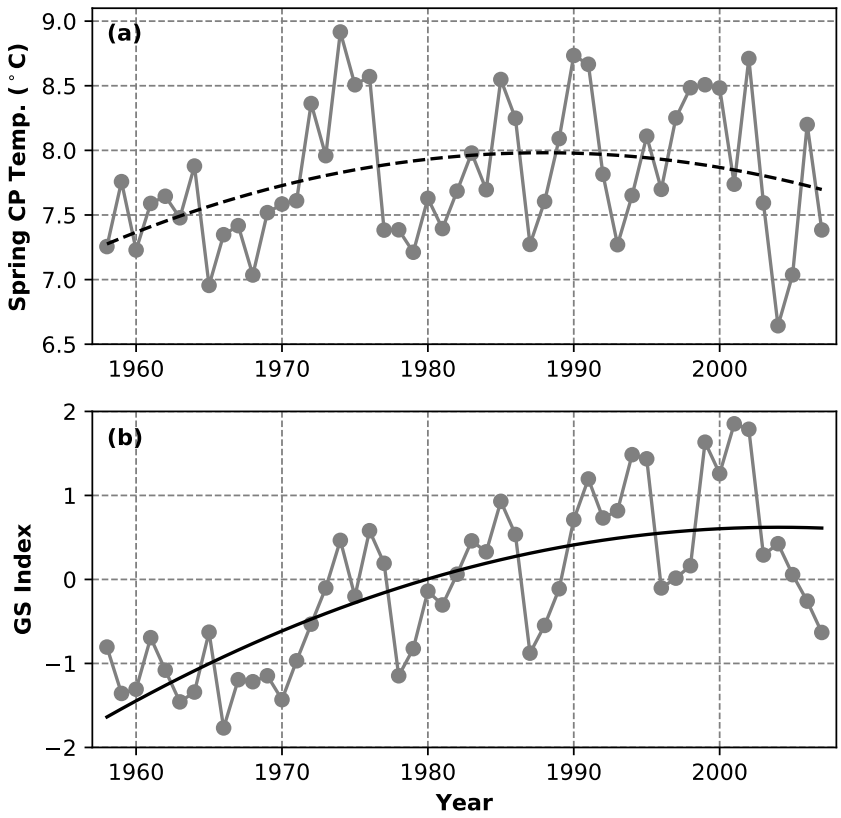

Figure 4.4: (a) Spring Cold Pool (CP) temperatures (gray circles) from 1958 to 2007 and its long-term trend computed by a quadratic fit. (b) The annual GS index (gray circles) and its long-term trend computed by a quadratic fit.

We also perform a lead-lag correlation between seasonal GS indexes and spring Cold Pool temperatures with a lag of 0 to 4 years (Cold Pool temperature lags GS index; Table 4.2). Results show that spring Cold Pool temperatures have the largest correlation with seasonal GS indexes at the same year, with limited ocean memory at a lead or lag of less than one year. The maximum correlation between spring GS position and spring Cold Pool temperature is about 0.50 at zero lag. The maximum lag that is significant at the 99% confidence level is 6 months between the fall GS position and spring Cold Pool temperature ($r = 0.40$). The secondary lag that is above 99% significant is 3 months between the

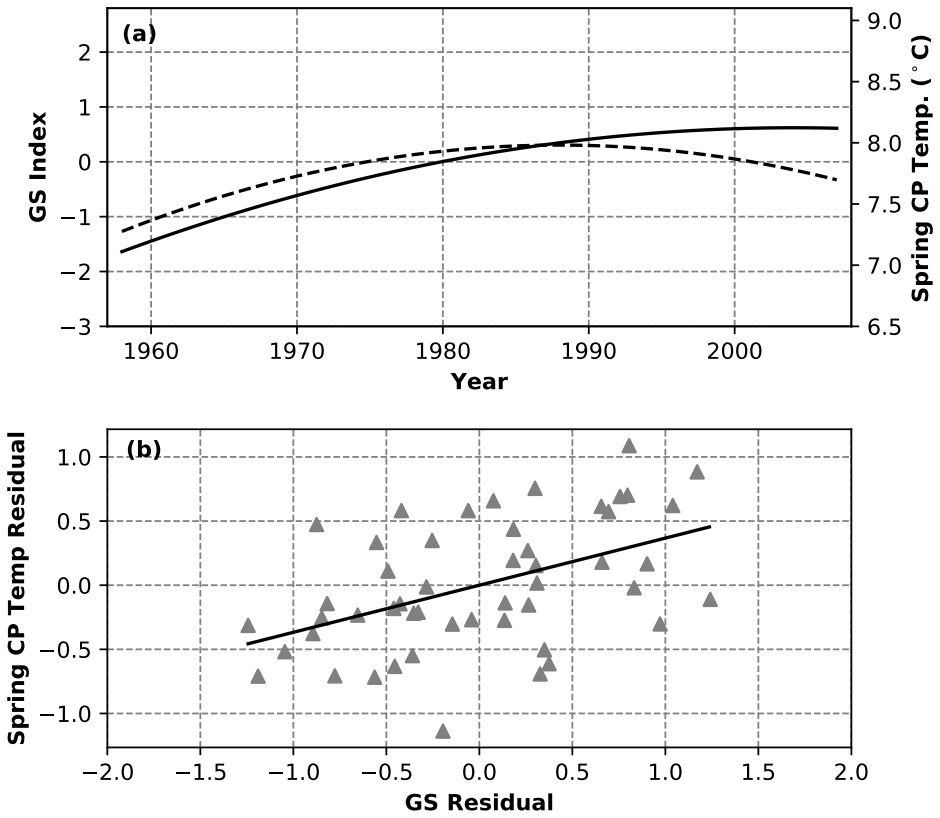

Figure 4.5: (a) Comparison of the long-term trends between spring CP temperature (dashed line) and annual GS index (solid line). (b) Scatter plot of residuals of spring CP temperature and annual GS index and the 1-d linear regression line between them. The regression ($CP = 0.3672 \times GS$) has $r^2 = 0.227$ and $p < 0.001$.

winter GS position and spring Cold Pool temperature, with a increased correlation coefficient of 0.46. However, the lead correlations between the GS position and spring temperature are higher. The summer and fall GS position are highly correlated with spring Cold Pool temperature at a 3-month lead ($r = 0.52$; $p = 10^{-4}$) and a 6-month lead ($r = 0.54$; $p < 10^{-4}$).

Similarly, the lead-lag correlation between seasonal GS indexes and summer Cold Pool temperatures is also significant with leads or lags within a year. At zero lag, the correlation between summer GS position and summer temperature reaches 0.44 ($p < 0.01$). Winter and spring GS position correlate with summer

Table 4.2: Lead-lag correlation coefficients between seasonal GS indexes and the spring Cold Pool (CP) temperature at a lag of 0-4 years.

Spring CP temp. &	Lag 0	Lag 1
Winter GS	r=**0.46**; lag=3m	
Spring GS	r=**0.50**; lag=0m	
Summer GS	r=**0.52**; lag=-3m	r=0.33; lag=9m
Fall GS	r=**0.54**; lag=-6m	r=**0.40**; lag=6m

[a] Only coefficients that are significant at the 95% confidence level are shown.
[b] Bold coefficients are significant at the 99% confidence level.

temperature at lags of 6 months ($r = 0.39$) and 3 months ($r = 0.41$), both significant at the 99% confidence level. For the fall GS position, the correlation with summer Cold Pool temperature are maximized at a lead of 3 months ($r = 0.47$, $p < 0.001$).

Table 4.3: Lead-lag correlation coefficients between seasonal GS indexes and the summer Cold Pool (CP) temperature at a lag of 0-4 years.

Summer CP temp. &	Lag 0	Lag 1
Winter GS	r=**0.39**; lag=6m	
Spring GS	r=**0.41**; lag=3m	
Summer GS	r=**0.44**; lag=0m	r=0.30; lag=1y
Fall GS	r=**0.47**; lag=-3m	r=0.35; lag=9m

[a] Only coefficients that are significant at the 95% confidence level are shown.
[b] Bold coefficients are significant at the 99% confidence level.

To conclude, the Cold Pool temperature is significantly correlated with the GS position at a lead or lag within a year. This implies that the Cold Pool and the GS have a consistent response at a time lag within a year. The maximum correlation and lag months is between the fall GS position and the following spring Cold Pool temperature. This lag relationship enhances the use of the fall GS positions as a predictor of the spring Cold Pool temperature.

4.4.3 Cold Pool Temperature Response to the NAO

Changes of the southwestward transport of the LC along the continental shelf has been suggested to be affected by the NAO [Drinkwater et al., 1998, Bersch et al., 2007]. Besides, the north-south shift of the GS position is linked to low frequency variability in the AMOC [Joyce and Zhang, 2010] and atmospheric forcing in the form of the NAO, with the GS lagging the NAO by approximately 2 years [Taylor and Stephens, 1998]. Our analysis of the correlation between NAO and GS position also suggests a maximum correlation ($r = 0.68$, $p < 10^{-6}$) at the lag of about 2 years (Table 4.4). Both of the LC transport and GS position will have an impact on the Cold Pool. Therefore, in this section, we investigate whether the Cold Pool temperature has a response to the NAO by examining the relationship between the Cold Pool temperature and the large scale atmospheric climate indices - the winter NAO index.

Table 4.4: The maximum correlation coefficients and responding time lags between the seasonal GS indexes and the winter NAO.

Winter NAO &	With trend	Without trend	Time lag
Winter GS	0.66	0.48	lag=2y
Spring GS	0.66	0.48	lag=2.25y
Summer GS	0.67	0.47	lag=2.5y
Fall GS	0.65	0.47	lag=1.75y

Over the 50 years, the phase of the NAO has been shifted from mostly negative in the 1960s and 1970s to mostly positive values in the 1980s and 1990s [Visbeck et al., 2001] (Figure 4.7). Lead-lag correlations suggest that the Cold Pool temperature is significantly correlated with winter NAO at a lag of less than 6 months (Figure 4.6; Table 4.5). The correlation coefficients with the spring ($r = 0.48$) and summer ($r = 0.42$) Cold Pool temperatures at a lag of 3 months and 6 months are both significant at the 99% confidence level. The positive correlations imply that the Cold Pool temperature increases (decreases) when the

NAO has a positive (negative) phase, or there is an increase (decrease) of pressure gradient between AH and IL during the winter.

Table 4.5: Lead-lag correlation between winter NAO index and Cold Pool (CP) spring and summer temperature at a lag of 0-7 years.

Winter NAO &	Lag 0	Lag 1	Lag 2
Spring CP temp.	r=**0.48**;lag=3m	r=0.31;lag=1.25y	r=**0.46**;lag=2.25y
Summer CP temp.	r=**0.42**;lag=6m	r=**0.41**;lag=1.5y	r=**0.42**;lag=2.5y

[a] Only coefficients that are significant at the 95% confidence level are shown.
[b] Bold coefficients are significant at the 99% confidence level.

The positive impact of the winter NAO on the Cold Pool temperature with a time lag of less than a year indicates the influence may through local atmospheric forcing and the so-called *reemergence mechanism*. The *reemergence mechanism* is first noted by Namias and Born [1970, 1974], suggesting that there is tendency for midlatitude winter SST anomalies to persist below the seasonal thermocline in avoidance of influence from surface processes and reappear in the next winter Alexander and Deser [1995]. Figure 4.8 shows a schematic diagram about the reemergence mechanism of SST anomalies. The first half of processes explains how local atmospheric forcing in the winter affects the Cold Pool temperature in the following spring and summer. This is also coherent with findings of Visbeck et al. [2003], which suggests a positive effect of winter NAO on the SSTs of the NES in the winter.

The lead-lag correlation analysis also shows the Cold Pool temperature, especially spring Cold Pool temperature has a 2.25-year lag with the winter NAO ($r = 0.46$; $p < 0.01$; Cold Pool lags NAO). This approximately 2-year time lag is consistent with the findings of the 2-year time lag between the LSW and winter NAO by Mountain [2012]. To make a comparison with results in Mountain [2012], quadratic fits of winter NAO and spring Cold Pool temperature are both computed to capture the long-term trends and the non-linearity of each time series. The quadratic fits exhibit the same trend with increasing values from the 1960s

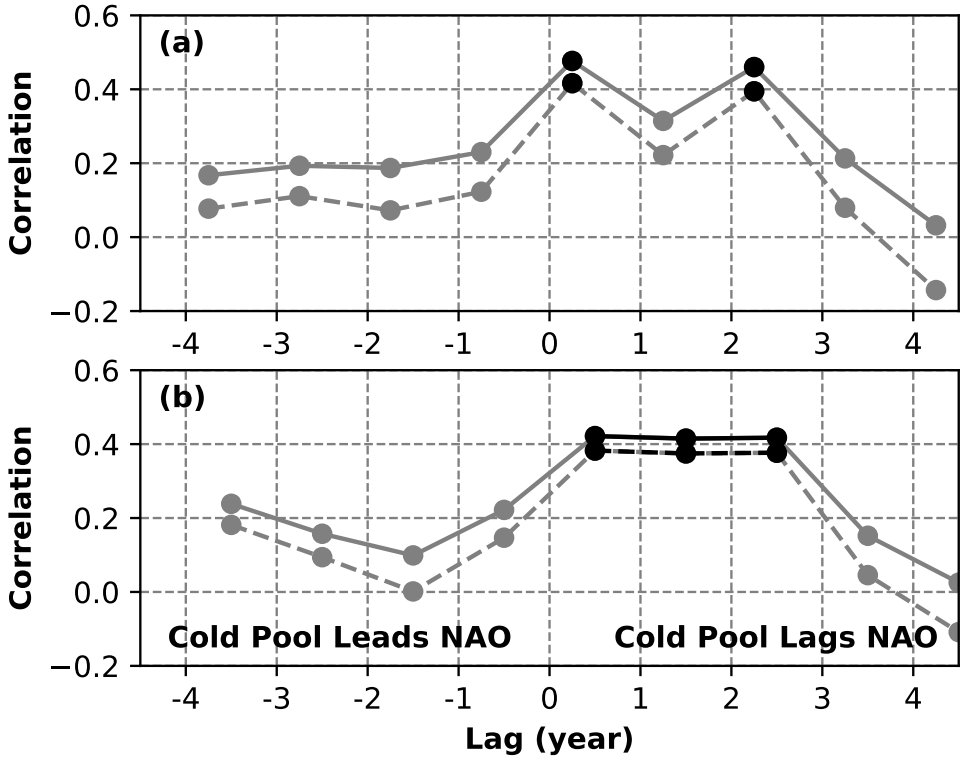

Figure 4.6: Lead-lag correlations between winter NAO and Cold Pool (CP) spring (a) and summer (b) temperatures with (solid lines) and without (dashed lines) linear trends. Correlations that are significant at the 99% confidence level is plotted in black dots.

to the 1990s, which recomfirms the significant relationship between the two time series (Figure 4.7). Similarly, the relationship between the Cold Pool spring temperature and the winter NAO (lead by 2 years) has a relatively higher correlation before the 1990s. The correlation between the two time series maximized from 1958 to 1992 ($r = 0.62$, $p < 10^{-4}$). The linear regression of the residuals for the two series also suggests a significant positive correlation. Whereas from 1992 to 2007, the relationship has changed similar to that between the Cold Pool spring temperature and the GS position (Figure 4.9 a). The long-term trend of the Cold Pool spring temperature has a slight decrease after the 1990s, whereas the NAO has a smaller decrease during the same period. The correlation coefficient between the two time series decreases to 0.15. After the 1990s, the difference in

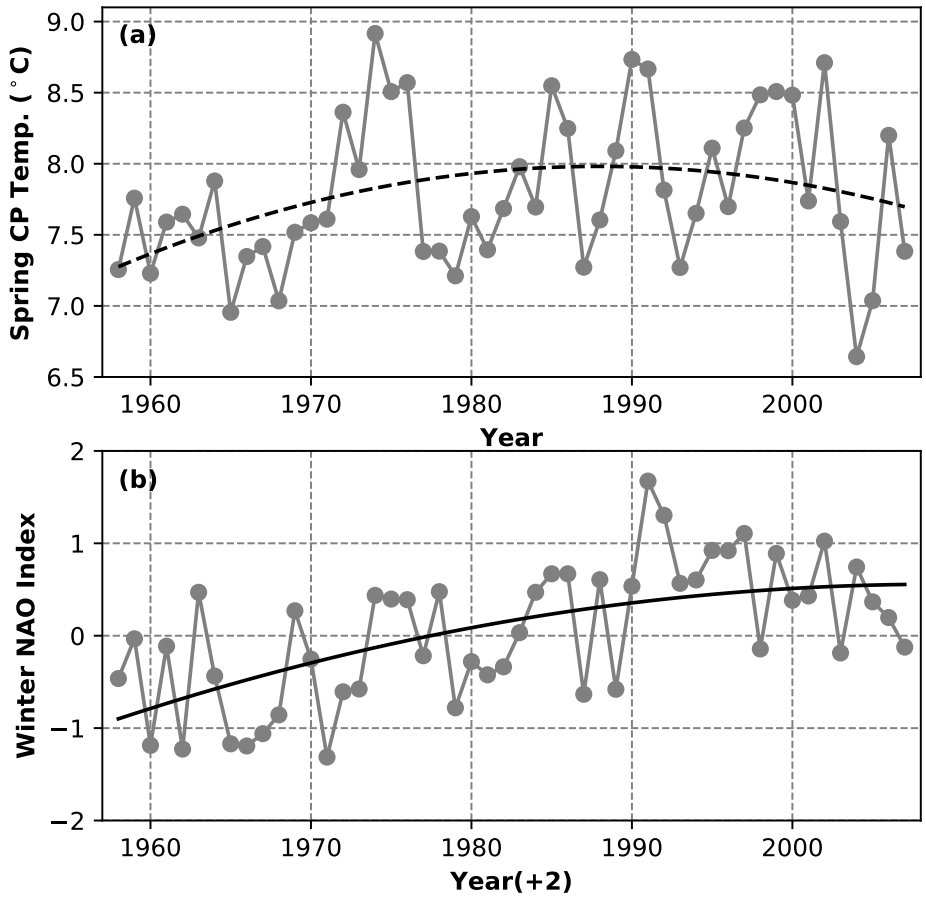

Figure 4.7: (a) Spring Cold Pool (CP) temperatures (gray circles) from 1958 to 2007 and its long-term trend computed by a quadratic fit. (b) The annual winter NAO index, shifted 2 years from 1956 to 2005 and its long-term trend computed by a quadratic fit.

the long-term trends of both time series is indicative of the reduced response of the spring Cold Pool temperature to variations in the winter NAO.

4.5 Discussion

In this study, we investigate the relationship between the MAB Cold Pool temperature and the north-south shift of the GS position. The Cold Pool interannual characteristics are quantified using a high-resolution hindcast simulation of the Northwest Atlantic Ocean. It is mainly located in the mid- and outer-shelf, extending from the 40- to 100-m isobaths. During weak Cold Pool years (warmer), its average location usually has a poleward shift along with the GS position. The annual GS index has a maximum correlation with the spring Cold Pool temperature of about 0.52 ($p < 0.001$). We also identify that the GS position could be a leading indicator of the Cold Pool temperature over the shelf. The fall GS position is significantly correlated with the Cold Pool temperature in the following spring, with a coefficient of 0.40. Commercially-important fish species like the silver hake over the outer-shelf (>100-m isobath), has been reported to have a similar relationship with the GS [Nye et al., 2011, Davis et al., 2017]. The fall GS index has a maximum correlation with the spatial distribution of silver hake in the following spring, with a much higher coefficient of 0.72 ($p < 0.001$). These relationships confirm the impact of the GS over the continental shelf and adjacent waters. It is also consistent with previous studies that changes in the slope waters can account for 50% of temperature variation over the shelf with a lag of 3-6 months [Loder et al., 2003].

Our findings also indicate that the Cold Pool, as well as the GS, has a positive response to remote oceanographic processes in the Labrador Sea, associated with the NAO. The Cold Pool temperature is significantly correlated with the NAO, which leads the Cold Pool by approximately 2 years. This time lag is consistent

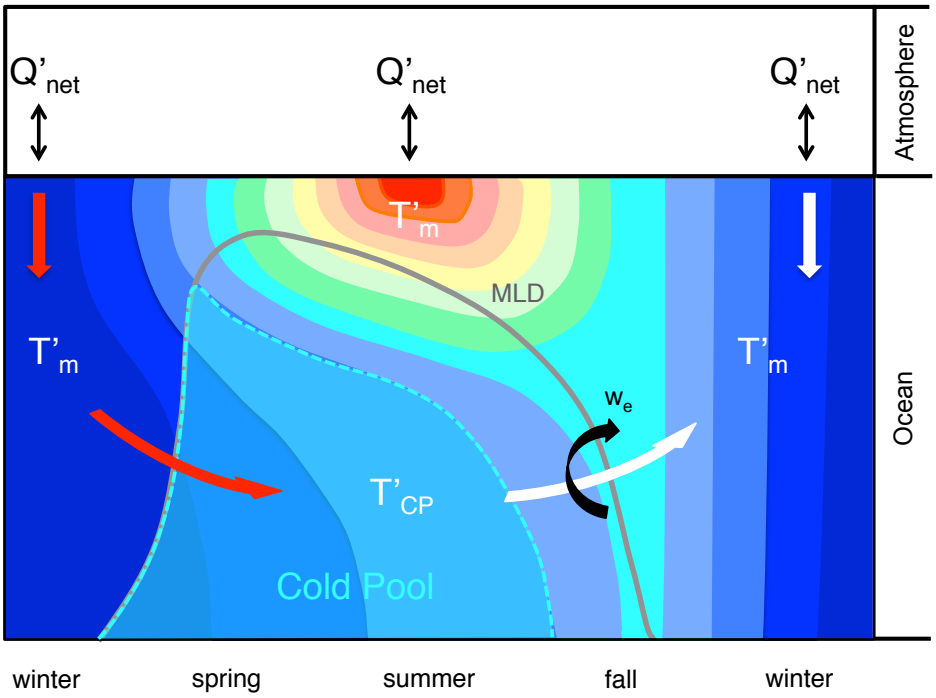

Figure 4.8: A schematic diagram of the *reemergence mechanism* replotted from Alexander and Deser [1995], focusing on illustrating how the winter SST anomalies affect the Cold Pool temperature below the seasonal thermocline during the same year (represented by the red arrows). Q'_{net} represents anomaly of the net air-sea heat flux. T'_m and T'_{CP} represent temperature anomaly within the mixed layer and the bottom layer. w_e represents entrainment of bottom temperature anomalies into the surface mixed layer in the fall. The gray solid line represents the mixed-layer depth (MLD). The translucent light blue patch represents the Cold Pool.

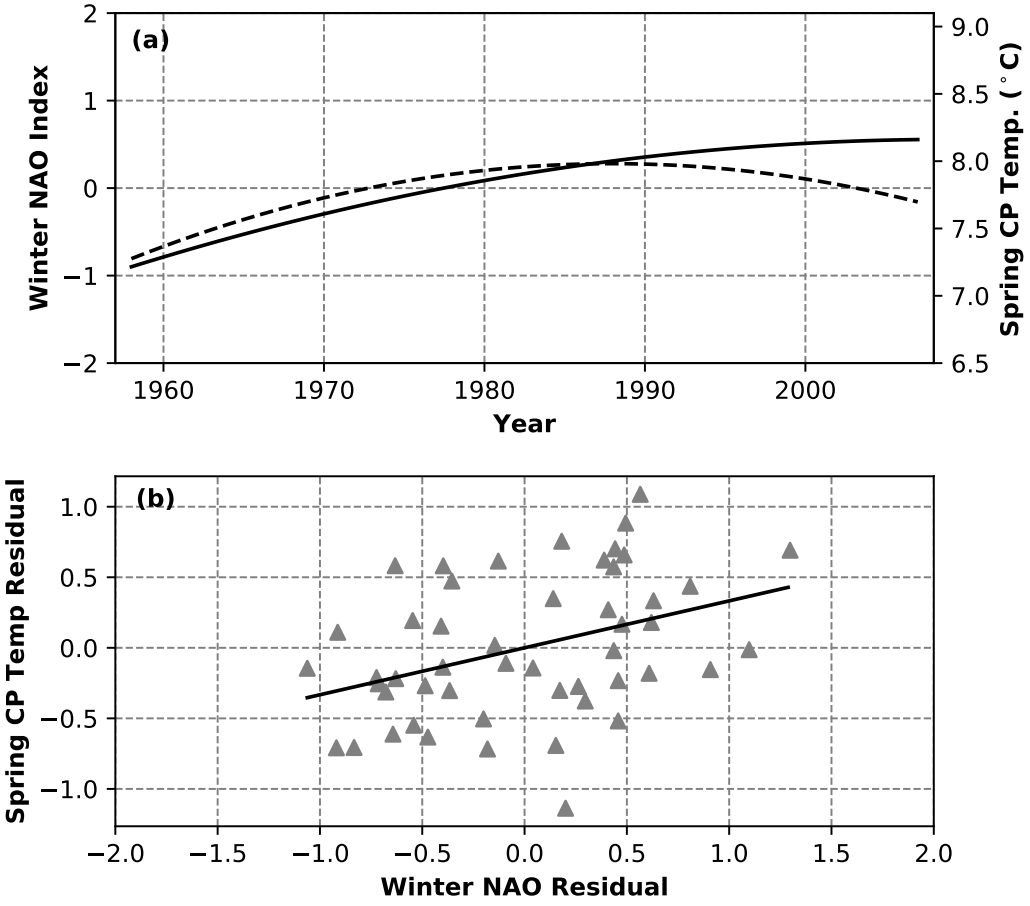

Figure 4.9: (a) Comparison of the long-term trends between spring CP temperature (dashed line) and winter NAO index (solid line). (b) Scatter plot of residuals of spring CP temperature and winter NAO index and the 1-d linear regression line between them. The regression ($CP = 0.3327 \times NAO$) has $r^2 = 0.15$ and $p < 0.01$.

with the lag between the NAO and the GS position, as well as that between the NAO and percent of LSW entering the GoM [Taylor and Stephens, 1998, Joyce et al., 2000, Mountain, 2012]. A long-term collection of observations along the US east coast suggests that along-shelf advection from the Labrador to Cape Hatteras of the coastal regions dominates the long-term changes of temperature of this region [Shearman and Lentz, 2010]. It is plausible to suggest that both the Cold Pool and the GS position are affected by 'upstream' processes that is related to the NAO. During positive NAO years, reduced southwestward transport of the LC leads to less percent of LSW entering the GoM, warmer Cold Pool temperature, and closer distance of the GS to the continental shelf. Conversely, increased flow of the LC leads to more LSW entering the GoM, cooler Cold Pool temperature on the shelf, and a southward shift of the GS.

We also have noted that the long-term trend of the Cold Pool temperature has a divergence from that of the NAO and the GS indexes after about 1990. However, the GS and the NAO do not have such a big difference. This implies that the Cold Pool's response to the NAO changes after about 1990. The reason still remains unclear. Coincidently, the long-term trend of the percent of LSW entering the GoM also has a similar divergence from that of the NAO after about 1990 [Mountain, 2012]. They attribute it to the westward and eastward movement of the nominal boundary between the LSW and WSW before and after about 1990. Through the shift of the boundary movement, the LSW entering the GoM is more diluted by mixing. However, this explanation does not suitable for the Cold Pool temperature. Besides, we use the reemergence mechanism over the MAB continental shelf to explain the 3-6 month time lag between the Cold Pool temperature and the NAO. However, a detailed investigation of the reappearance of upstream winter SSTs is beyond the scope of this work.

Chapter 5
Conclusions

The principal objective of this dissertation is to investigate spatio-temporal variability of the MAB Cold Pool using a long-term (1958-2007) high-resolution (about 7 km in horizontal and 40 terrain-following layers) numerical model (ROMS-NWA) and its response to large-scale processes of the Northwest Atlantic Ocean. The model is capable of capturing the overall structure and temporal variability of the Cold Pool over the continental shelf region. The Cold Pool is defined as a relatively cold and fresh water mass, develops below a seasonal thermocline, located over the mid- and outer-shelf. Following this definition, we employ three criteria to quantify the Cold Pool characteristics based on the 50-year high-resolution model hindcast. We reproduce the seasonal evolution of the Cold Pool on a 50-year average using the quantification method. Moreover, further analysis of the Cold Pool during strong and weak years, sheds light on interannual variability of the Cold Pool and the relationship with large-scale oceanic and atmospheric processes. The following is a summary of the principal conclusions of each research chapter.

Chapter 2 presents the seasonal climatology of the Cold Pool based on 50-year model output. This chapter also introduces the method for processing the model data to quantify the Cold Pool characteristics based on its definition. This quantified dataset has a significant advance in representing the spatio-temporal distribution of the Cold Pool during its seasonal evolution, which is imaged in three dimensions. Moreover, analysis of the temporal variations of the Cold Pool volume suggests that it is a continuous feature that experiences an *onset* - *peak* -

decline cycle. Typically it first emerges around early April, reaches maximum volume around mid-May and then gradually disappears around mid-September. The Cold Pool volume has a fast expansion in the south of Nantucket Shoals, which is considered as the winter remnant source water. Furthermore, cores of the Cold Pool move equatorward from the south of Nantucket Shoals to the Hudson Shelf Valley, along the 60-m isobath with a speed of about 2 cm/s. The warming rates of the Cold Pool cores is about 0.03 °C/day during the summer. The northern extent of the Cold Pool retreats 2.6 times faster than the southern one, which is due to horizontal advection of upstream warm water from the southern flank of Georges Bank. While in the southern edge of the Cold Pool, the down-stream advection of the Cold Pool water slows down the retreating speed. The importance of horizontal advection over the vertical mixing is confirmed in the detailed quantitative investigation of the near-bottom depth-averaged heat budget.

Chapter 3 presents an investigation of the interannual variability of the Cold Pool using the composite analysis. A Cold Pool Index is derived from the persistence time, volume and volume-averaged temperature, for evaluation of the Cold Pool strength. The Cold Pool characteristics and its summer progression during strong and weak years are compared. The Cold Pool during strong years persists 6.5 months from early-April to October; while during weak years it persists only for 4 months from early-April to August. The peak volumes during weak years are only about one-third of that during strong years. The minimum temperature of the Cold Pool is warmer by about 2 °C during weak years than that during strong years, although the warming rate is almost the same. Moreover, during strong years, the cores not only travels farther south to the Hudson Shelf Valley, but have a faster traveling speed (2.1 cm/s) than that of weak years (1.5 cm/s). The difference in retreating speeds of the northern and southern extents decreases to almost zero during weak years. In other words, horizontal advection of the Cold Pool water is too weak to overcome warming and mixing from the surface layer.

A volume-averaged heat budget of the Cold Pool region is investigated in detail between strong and weak years. Results suggest that initial temperature in the early spring and total advection during the summer are two main factors that dominate the temperature of the Cold Pool region. Abnormal warming/cooling from the initial temperature and total advection impact the interannual variability of the Cold Pool temperature. Furthermore, relative to total advection, initial temperature in the early spring is more closely related to the temperature anomaly in the Cold Pool, suggests that seasonal predictability may be possible, which warrants further investigation.

Chapter 4 presents an investigation of the relationship between the Cold Pool temperature and the north-south shift of the Gulf Stream, as well as the Cold Pool's response to the North Atlantic Oscillation. During weak Cold Pool years, its average location usually has a poleward shift along with a northward shift of the Gulf Stream position. The spring Cold Pool temperature is highly correlated with the Gulf Stream Index ($r = 0.52$, $p < 0.001$). A lead-correlation ($r = 0.40$, $p < 0.01$) between fall Gulf Stream Index and Cold Pool temperature in the following spring suggests predictability of the Cold Pool temperature using the Gulf Stream Index. The positive correlation coefficients confirm the impact of the Gulf Stream over the continental shelf and adjacent waters of previous studies. Furthermore, the Cold Pool has a positive response to remote oceanographic processes in the Labrador Sea, associated with the NAO. The Cold Pool temperature is significantly correlated with the NAO, which leads the Cold Pool by approximately 2 years. The 2-year time lag is consistent with that between the Gulf Stream Index and the NAO index, and with that between the percent of Labrador Slope Water entering the Gulf of Maine and the NAO index.

All these results provide an important insight into the spatial variability of the Cold Pool on time scales from seasonal to climate, using the long-term high-resolution hindcast model (ROMS-NWA). These investigations help us better

understand the formation and evolution of the Cold Pool during stratified seasons and explore its origins and relationship to variability in the large-scale ocean circulation, as well as in turn confirm the value of using high-resolution numerical models when studying the Cold Pool.

Global climate models, especially higher resolution models predict the Northwest Atlantic continental shelf will have a general warming trend (IPCC fifth assessment; Saba et al. [2016]). As the most important thermal feature over the MAB during stratified seasons, the Cold Pool has a first order impact on the marine ecosystem, for example, recruitment and settlement of commercially important fisheries (e.g., Sullivan et al. [2005], Miller et al. [2016]). This suggest that in the future there may be substantial changes in the dynamics and structure of the MAB ecosystem under these predictions. This work presents an investigation of dynamics and natural variability of the Cold Pool and a potential mechanism linking the Cold Pool and large-scale oceanic processes in the Northwest Atlantic Ocean, which is meaningful for prediction on living marine resources over the Northwest Atlantic continental shelf.

Bibliography

Charles F Adams, Timothy J Miller, John P Manderson, Dave E Richardson, and Brian Eugene Smith. *Butterfish 2014 stock assessment*. US Department of Commerce, National Oceanic and Atmospheric Administration, National Marine Fisheries Service, Northeast Fisheries Science Center, 2015.

Michael A Alexander and Clara Deser. A mechanism for the recurrence of wintertime midlatitude sst anomalies. *Journal of physical oceanography*, 25(1): 122–137, 1995.

Robert C Beardsley, David C Chapman, Kenneth H Brink, Steven R Ramp, and Ronald Schlitz. The Nantucket Shoals Flux Experiment (NSFE79). Part I: A basic description of the current and temperature variability. *Journal of Physical Oceanography*, 15(6):713–748, 1985.

Robert L Benway and Jack W Jossi. Departures of 1996 temperatures and salinities in the Middle Atlantic Bight and Gulf of Maine from historical means. *Journal of Northwest Atlantic Fishery Science*, 24:61–86, 1998.

Manfred Bersch, Igor Yashayaev, and Klaus Peter Koltermann. Recent changes of the thermohaline circulation in the subpolar north atlantic. *Ocean Dynamics*, 57(3):223–235, 2007.

Hongsheng Bi, Rubao Ji, Hui Liu, Young-Heon Jo, and Jonathan A Hare. Decadal changes in zooplankton of the northeast us continental shelf. *PloS one*, 9(1): e87720, 2014.

Henry Bryant Bigelow and Mary Sears. *Studies of the Waters of the Continental Shelf, Cape Cod to Chesapeake Bay: I. A Volumetric Study of the Zooplankton*. Massachusetts Institute of Technology, 1933.

W Brown, W Boicourt, C Flagg, A Gangopadhyay, O Schofield, S Glenn, and J Kohut. Mapping the Mid-Atlantic Cold Pool evolution and variability with ocean gliders and numerical models. In *2012 Oceans*, pages 1–6. IEEE, 2012.

W Brown, O Schofield, S Glenn, J Kohut, and W Boicourt. The Evolution of the Mid-Atlantic Bight Cold Pool Based on Ocean Glider Observations. Technical report, School for Marine Science and Technology, University of Massachusetts Dartmouth, 2015.

Martha W Buckley and John Marshall. Observations, inferences, and mechanisms of the atlantic meridional overturning circulation: A review. *Reviews of Geophysics*, 54(1):5–63, 2016.

Bradford Butman, RC Beardsley, Bruce Magnell, Daniel Frye, JA Vermersch, Ronald Schlitz, Richard Limeburner, WR Wright, and MA Noble. Recent observations of the mean circulation on georges bank. *Journal of Physical Oceanography*, 12(6):569–591, 1982.

James A Carton and Benjamin S Giese. A reanalysis of ocean climate using simple ocean data assimilation (soda). *Monthly Weather Review*, 136(8):2999–3017, 2008.

Renato Castelao, Scott Glenn, Oscar Schofield, Robert Chant, John Wilkin, and Josh Kohut. Seasonal evolution of hydrographic fields in the central Middle Atlantic Bight from glider observations. *Geophysical Research Letters*, 35(3), 2008.

David C Chapman and Robert C Beardsley. On the origin of shelf water in the Middle Atlantic Bight. *Journal of Physical Oceanography*, 19(3):384–391, 1989.

Zhuomin Chen and Enrique Curchitser. Inter-annual Variability of the Mid-Atlantic Bight Cold Pool. *Journal of Geophysical Research: Oceans. In Review*, 2018b.

Zhuomin Chen, Enrique Curchitser, Robert Chant, and Dujuan Kang. Seasonal Variability of the Cold Pool over the Mid-Atlantic Bight Continental Shelf. *Journal of Geophysical Research: Oceans. In Review*, 2018a.

James H Churchill and Glen G Gawarkiewicz. Pathways of shelf water export from the Hatteras shelf and slope. *Journal of Geophysical Research: Oceans*, 117(C8), 2012.

M Collins. Coauthors, 2013: Long-term climate change: Projections, commitments and irreversibility. Climate Change 2013: The Physical Science Basis, TF Stocker et al., Eds. *Cambridge University Press, Cambridge, United Kingdom and New York, NY, USA*, 10291136, 2013.

Aiguo Dai, Taotao Qian, Kevin E Trenberth, and John D Milliman. Changes in continental freshwater discharge from 1948 to 2004. *Journal of climate*, 22(10): 2773–2792, 2009.

P Soupy Dalyander, Bradford Butman, Christopher R Sherwood, Richard P Signell, and John L Wilkin. Characterizing wave-and current-induced bottom shear stress: US middle Atlantic continental shelf. *Continental Shelf Research*, 52:73–86, 2013.

Xujing Jia Davis, Terrence M Joyce, and Young-Oh Kwon. Prediction of silver hake distribution on the northeast us shelf based on the gulf stream path index. *Continental Shelf Research*, 138:51–64, 2017.

Clément de Boyer Montégut, Gurvan Madec, Albert S Fischer, Alban Lazar, and Daniele Iudicone. Mixed layer depth over the global ocean: An examination of

profile data and a profile-based climatology. *Journal of Geophysical Research: Oceans*, 109(C12), 2004.

KF Drinkwater, DB Mountain, and A Herman. Recent changes in the hydrography of the scotian shelf and gulf of maine– a return to conditions of the 1960s? *Sci. Counc. Res. Doc. NAFO*, (98):16, 1998.

Gary D Egbert and Svetlana Y Erofeeva. Efficient inverse modeling of barotropic ocean tides. *Journal of Atmospheric and Oceanic Technology*, 19(2):183–204, 2002.

Richard G Fairbanks. The origin of continental shelf and slope water in the New York Bight and Gulf of Maine: evidence from H2 18O/H2 16O ratio measurements. *Journal of Geophysical Research: Oceans*, 87(C8):5796–5808, 1982.

CN Flagg, CD Wirick, and Sharon L Smith. The interaction of phytoplankton, zooplankton and currents from 15 months of continuous data in the Mid-Atlantic Bight. *Deep Sea Research Part II: Topical Studies in Oceanography*, 41(2-3):411–435, 1994.

Jacob Samuel Tse Forsyth, Magdalena Andres, and Glen G Gawarkiewicz. Recent accelerated warming of the continental shelf off New Jersey: Observations from the CMV Oleander expendable bathythermograph line. *Journal of Geophysical Research: Oceans*, 120(3):2370–2384, 2015.

Alejandra Sanchez Franks. *Structure and Dynamics of the Gulf Stream's Interannual Migration East of Cape Hatteras*. State University of New York at Stony Brook, 2015.

Kevin D Friedland and Jonathan A Hare. Long-term trends and regime shifts in sea surface temperature on the continental shelf of the northeast united states. *Continental Shelf Research*, 27(18):2313–2328, 2007.

RW Fulweiler, AJ Oczkowski, KM Miller, CA Oviatt, and MEQ Pilson. Whole truths vs. half truths–and a search for clarity in long-term water temperature records. *Estuarine, Coastal and Shelf Science*, 157:A1–A6, 2015.

Glen Gawarkiewicz, Ke Chen, James F Lynch, Thomas M Grothues, Arthur Newhall, and Ying-Tsong Lin. Impacts of the warming of the continental shelf in spring 2012 on acoustic propagation conditions and fish distributions north of cape hatteras. *The Journal of the Acoustical Society of America*, 135(4): 2154–2154, 2014.

Glen Gawarkiewicz, Robert E Todd, Weifeng Zhang, Jacob Partida, Avijit Gangopadhyay, Mahmud-Ul-Hasan Monim, Paula Fratantoni, Anna Malek Mercer, and Margaret Dent. The changing nature of shelf-break exchange revealed by the ooi pioneer array. *Oceanography*, 31(1):60–70, 2018.

Glen G Gawarkiewicz, Robert E Todd, Albert J Plueddemann, Magdalena Andres, and James P Manning. Direct interaction between the Gulf Stream and the shelfbreak south of New England. *Scientific reports*, 2, 2012.

D Gong, JT Kohut, and SM Glenn. Seasonal climatology of wind-driven circulation on the New Jersey Shelf. *Journal of Geophysical Research: Oceans*, 115 (C4), 2010.

Arnold L Gordon and Frank Aikman. Salinity maximum in the pycnocline of the middle atlantic bight1, 2. *Limnology and Oceanography*, 26(1):123–130, 1981.

Charles H Greene, Erin Meyer-Gutbrod, Bruce C Monger, Louise P McGarry, Andrew J Pershing, Igor M Belkin, Paula S Fratantoni, David G Mountain, Robert S Pickart, Andrey Proshutinsky, et al. Remote climate forcing of decadal-scale regime shifts in northwest atlantic shelf ecosystems. *Limnology and Oceanography*, 58(3):803–816, 2013.

Gregory Han and Terren Niedrauer. Hydrographic observations and mixing processes in the New York Bight, 1975–1977. *Limnology and Oceanography*, 26(6): 1126–1141, 1981.

Guoqi Han, Kyoko Ohashi, Nancy Chen, Paul G Myers, Nuno Nunes, and Jürgen Fischer. Decline and partial rebound of the labrador current 1993–2004: Monitoring ocean currents from altimetric and conductivity-temperature-depth data. *Journal of Geophysical Research: Oceans*, 115(C12), 2010.

TS Hopkins and N Garfield III. Gulf of Maine intermediate water. *J. Mar. Res.;(United States)*, 37(1), 1979.

Robert W Houghton, Ronald Schlitz, Robert C Beardsley, Bradford Butman, and J Lockwood Chamberlin. The Middle Atlantic Bight cold pool: Evolution of the temperature structure during summer 1979. *Journal of Physical Oceanography*, 12(10):1019–1029, 1982.

Terrence M Joyce and Rong Zhang. On the path of the gulf stream and the atlantic meridional overturning circulation. *Journal of Climate*, 23(11):3146–3154, 2010.

Terrence M Joyce, Clara Deser, and Michael A Spall. The relation between decadal variability of subtropical mode water and the north atlantic oscillation. *Journal of Climate*, 13(14):2550–2569, 2000.

Dujuan Kang and Enrique N Curchitser. Gulf Stream eddy characteristics in a high-resolution ocean model. *Journal of Geophysical Research: Oceans*, 118(9): 4474–4487, 2013.

Dujuan Kang and Enrique N Curchitser. Energetics of eddy–mean flow interactions in the Gulf Stream region. *Journal of Physical Oceanography*, 45(4): 1103–1120, 2015.

Dujuan Kang and Enrique N Curchitser. On the evaluation of seasonal variability of the ocean kinetic energy. *Journal of Physical Oceanography*, 47(7):1675–1683, 2017.

Dujuan Kang, Enrique N Curchitser, and Anthony Rosati. Seasonal Variability of the Gulf Stream Kinetic Energy. *Journal of Physical Oceanography*, 46(4): 1189–1207, 2016.

Maria T Kavanaugh, Jennie E Rheuban, Kelly Luis, and Scott C Doney. Thirty-three years of ocean benthic warming along the us northeast continental shelf and slope: Patterns, drivers, and ecological consequences. *Journal of Geophysical Research: Oceans*, 2017.

Bostwick H Ketchum and Nathaniel Corwin. THE Persistance of Winter Water on the Continental Shelf South of Long Island, New York. *LIMNOLOGY*, 9, 1964.

Samar P Khatiwala, Richard G Fairbanks, and Robert W Houghton. Freshwater sources to the coastal ocean off northeastern North America- Evidence from H 2 O18/H2O16. *Journal of geophysical research*, 104(18):241–255, 1999.

William G Large, James C McWilliams, and Scott C Doney. Oceanic vertical mixing: A review and a model with a nonlocal boundary layer parameterization. *Reviews of Geophysics*, 32(4):363–403, 1994.

Steven J Lentz. Observations and a model of the mean circulation over the middle atlantic bight continental shelf. *Journal of Physical Oceanography*, 38(6):1203–1221, 2008a.

Steven J Lentz. Seasonal variations in the circulation over the middle atlantic bight continental shelf. *Journal of Physical Oceanography*, 38(7):1486–1500, 2008b.

Steven J Lentz. Seasonal warming of the middle atlantic bight cold pool. *Journal of Geophysical Research: Oceans*, 122(2):941–954, 2017.

Steven J Lentz, Robert C Beardsley, James D Irish, James Manning, Peter C Smith, and Robert A Weller. Temperature and salt balances on Georges Bank February–August 1995. *Journal of Geophysical Research: Oceans*, 108(C11), 2003.

Yun Li, Paula S Fratantoni, Changsheng Chen, Jonathan A Hare, Yunfang Sun, Robert C Beardsley, and Rubao Ji. Spatio-temporal patterns of stratification on the northwest atlantic shelf. *Progress in Oceanography*, 134:123–137, 2015.

John W Loder, Brian Petrie, and Glen Gawarkiewicz. The coastal ocean off northeastern North America: A large-scale view. *The sea*, 11:105–133, 1998.

John W Loder, Charles G Hannah, Brian D Petrie, and Elizabeth A Gonzalez. Hydrographic and transport variability on the halifax section. *Journal of Geophysical Research: Oceans*, 108(C11), 2003.

James Manning. Middle Atlantic Bight salinity: interannual variability. *Continental Shelf Research*, 11(2):123–137, 1991.

Timothy J Miller, Jonathan A Hare, and Larry A Alade. A state-space approach to incorporating environmental effects on recruitment in an age-structured assessment model with an application to southern New England yellowtail flounder. *Canadian Journal of Fisheries and Aquatic Sciences*, 73(999):1–10, 2016.

David G Mountain. Variability in the properties of Shelf Water in the Middle Atlantic Bight, 1977–1999. *Journal of Geophysical Research: Oceans*, 108(C1), 2003.

David G Mountain. Labrador slope water entering the gulf of maine - response to the north atlantic oscillation. *Continental Shelf Research*, 47:150–155, 2012.

Jerome Namias and Robert M Born. Temporal coherence in north pacific sea-surface temperature patterns. *Journal of Geophysical Research*, 75(30):5952–5955, 1970.

Jerome Namias and Robert M Born. Further studies of temporal coherence in north pacific sea surface temperatures. *Journal of Geophysical Research*, 79(6): 797–798, 1974.

Diego A Narváez, Daphne M Munroe, Eileen E Hofmann, John M Klinck, Eric N Powell, Roger Mann, and Enrique Curchitser. Long-term dynamics in Atlantic surfclam (Spisula solidissima) populations: The role of bottom water temperature. *Journal of Marine Systems*, 141:136–148, 2015.

Janet A Nye, Jason S Link, Jonathan A Hare, and William J Overholtz. Changing spatial distribution of fish stocks in relation to climate and population size on the northeast united states continental shelf. *Marine Ecology Progress Series*, 393:111–129, 2009.

Janet A Nye, Terrence M Joyce, Young-Oh Kwon, and Jason S Link. Silver hake tracks changes in northwest atlantic circulation. *Nature Communications*, 2: 412, 2011.

Hsien Wang Ou and Robert Houghton. A model of the summer progression of the cold-pool temperature in the Middle Atlantic Bight. *Journal of Physical Oceanography*, 12(10):1030–1036, 1982.

Brian Petrie and Kenneth Drinkwater. Temperature and salinity variability on the scotian shelf and in the gulf of maine 1945–1990. *Journal of Geophysical Research: Oceans*, 98(C11):20079–20089, 1993.

T Rossby and RL Benway. Slow variations in mean path of the gulf stream east of cape hatteras. *Geophysical Research Letters*, 27(1):117–120, 2000.

T Rossby and E Gottlieb. The oleander project: Monitoring the variability of the gulf stream and adjacent waters between new jersey and bermuda. *Bulletin of the American Meteorological Society*, 79(1):5–18, 1998.

Tom Rossby. On gyre interactions. *Deep Sea Research Part II: Topical Studies in Oceanography*, 46(1-2):139–164, 1999.

Vincent S Saba, Stephen M Griffies, Whit G Anderson, Michael Winton, Michael A Alexander, Thomas L Delworth, Jonathan A Hare, Matthew J Harrison, Anthony Rosati, Gabriel A Vecchi, et al. Enhanced warming of the Northwest Atlantic Ocean under climate change. *Journal of Geophysical Research: Oceans*, 121(1):118–132, 2016.

Jin Sha, Young-Heon Jo, Xiao-Hai Yan, and WT Liu. The modulation of the seasonal cross-shelf sea level variation by the cold pool in the Middle Atlantic Bight. *Journal of Geophysical Research: Oceans*, 120(11):7182–7194, 2015.

AF Shchepetkin and JC McWilliams. The regional ocean modeling system: A split-explicit, free-surface, topography-following-coordinate ocean model, 2003. *University of California at Los Angeles: Institute of Geophysics and Planetary Physics*, 2005.

R Kipp Shearman and Steven J Lentz. Long-term sea surface temperature variability along the us east coast. *Journal of Physical Oceanography*, 40(5):1004–1017, 2010.

Peter C Smith, Robert W Houghton, Richard G Fairbanks, and David G Mountain. Interannual variability of boundary fluxes and water mass properties in the Gulf of Maine and on Georges Bank: 1993–1997. *Deep Sea Research Part II: Topical Studies in Oceanography*, 48(1):37–70, 2001.

Yuhe Song and Dale Haidvogel. A semi-implicit ocean circulation model using a

generalized topography-following coordinate system. *Journal of Computational Physics*, 115(1):228–244, 1994.

David B Stephenson, Heinz Wanner, Stefan Brönnimann, and Jürg Luterbacher. The history of scientific research on the north atlantic oscillation. *The North Atlantic Oscillation: climatic significance and environmental impact*, pages 37–50, 2003.

Mark C Sullivan, Robert K Cowen, and Brian P Steves. Evidence for atmosphere–ocean forcing of yellowtail flounder (Limanda ferruginea) recruitment in the Middle Atlantic Bight. *Fisheries Oceanography*, 14(5):386–399, 2005.

Arnold H Taylor and John A Stephens. The north atlantic oscillation and the latitude of the gulf stream. *Tellus A: Dynamic Meteorology and Oceanography*, 50(1):134–142, 1998.

Martin Visbeck, Eric P Chassignet, Ruth G Curry, Thomas L Delworth, Robert R Dickson, and Gerd Krahmann. The ocean's response to north atlantic oscillation variability. *The North Atlantic Oscillation: climatic significance and environmental impact*, pages 113–145, 2003.

Martin H Visbeck, James W Hurrell, Lorenzo Polvani, and Heidi M Cullen. The north atlantic oscillation: past, present, and future. *Proceedings of the National Academy of Sciences*, 98(23):12876–12877, 2001.

James R Weinberg. Bathymetric shift in the distribution of Atlantic surfclams: response to warmer ocean temperature. *ICES Journal of Marine Science: Journal du Conseil*, 62(7):1444–1453, 2005.

John L Wilkin and Elias J Hunter. An assessment of the skill of real-time models of Mid-Atlantic Bight continental shelf circulation. *Journal of Geophysical Research: Oceans*, 118(6):2919–2933, 2013.

Haikun Xu, Timothy J Miller, Sultan Hameed, Larry A Alade, and Janet A Nye. Evaluating the utility of the gulf stream index for predicting recruitment of southern new england-mid atlantic yellowtail flounder. *Fisheries Oceanography*, 27(1):85–95, 2018.

Shuwen Zhang, Enrique N Curchitser, Dujuan Kang, Charles A Stock, and Raphael Dussin. Impacts of mesoscale eddies on the vertical nitrate flux in the gulf stream region. *Journal of Geophysical Research: Oceans*, 123(1):497–513, 2018a.

Weifeng G Zhang and Glen G Gawarkiewicz. Dynamics of the direct intrusion of Gulf Stream ring water onto the Mid-Atlantic Bight shelf. *Geophysical Research Letters*, 42(18):7687–7695, 2015.